Efficient and Low-Backaction Quantum Measurement Using a Chip-Scale Detector

by

Eric I. Rosenthal

B.A., University of Pennsylvania, 2015

M.S., University of Pennsylvania, 2015

A thesis submitted to the

Faculty of the Graduate School of the

University of Colorado in partial fulfillment

of the requirements for the degree of

Doctor of Philosophy

Department of Physics

2021

Committee Members:

Konrad W. Lehnert, Chair

Graeme Smith

John D. Teufel

Adam Kaufman

Joshua Combes

Rosenthal, Eric I. (Ph.D., Physics)

Efficient and Low-Backaction Quantum Measurement Using a Chip-Scale Detector

Thesis directed by Prof. Konrad W. Lehnert

Superconducting qubits are a leading platform for scalable quantum computing and quantum error correction. One feature of this platform is the ability to perform projective measurements orders of magnitude more quickly than qubit decoherence times. Such measurements are enabled by the use of quantum-limited parametric amplifiers in conjunction with ferrite circulators — magnetic devices which provide isolation from noise and decoherence due to amplifier backaction. Because these nonreciprocal elements have limited performance and are not easily integrated on chip, it has been a long-standing goal to replace them with a scalable alternative. Here, we demonstrate a solution to this problem by using a superconducting switch to control the coupling between a qubit and amplifier. Doing so, we measure a transmon qubit using a single, chip-scale device to provide both parametric amplification and isolation from the bulk of amplifier backaction. This measurement is also fast, high fidelity, and has 70% efficiency, comparable to the best that has been reported in any superconducting qubit measurement. As such, this work constitutes a high-quality platform for the scalable measurement of superconducting qubits.

Dedication

To my parents, brother, and Mia

Acknowledgements

I'm grateful to everyone who has supported and helped me over the course of my progression into a scientist. I can't express how lucky I am to be surrounded by so many thoughtful, encouraging and brilliant people. A thorough acknowledgement would be longer than this dissertation, but I want to specifically thank a few of you here.

First to my advisor Konrad: thank you for the dedication you took to advising me. Words can't express how grateful I am, both for the positive experience and for everything you taught me. Doing it over again I wouldn't hesitate to work for you.

To my undergraduate mentors including Matt LaHaye, Riichiro Saito and Alison Sweeney: thank you for the opportunity to get started, for your patience, and for believing in me.

To my colleagues in the Lehnert lab: thank you for creating such a supportive environment. I'm especially grateful to Ben Chapman, both for mentoring me and for being a positive role model, both as a scientist and an individual. To Christian Schneider, working with you was an absolute pleasure, thank you. To Ziyi Zhao, I look forward to seeing how you apply your creativity and brilliance to the project going forward.

To my friends, fellow graduate students, all of the JILA staff, and the Boulder physics community: I couldn't have done it without you. No matter what, I could always count on your help and camaraderie.

Finally to my family: thank you. To my parents and brother Greg, I appreciate that you have always being there for me near or far. To my partner, Mia Froehling Gallier, thank you for the love and support over the years.

Contents

Chapter

Tables

Table

Figures

Figure

List of Symbols

Fundamental constants

$h = 6.626 \times 10^{-34}\,\mathrm{m^2 kg/s}$	Planck's constant
$\hbar = h/2\pi = 1.055 \times 10^{-34}\,\mathrm{m^2 kg/s}$	reduced Planck's constant
$e = 1.602 \times 10^{-19}\,\mathrm{C}$	charge of an electron
$\Phi_0 = h/2e = 2.068 \times 10^{-15}\,\mathrm{Wb}$	magnetic flux quantum
$\phi_0 = \Phi_0/2\pi = 3.291 \times 10^{-16}\,\mathrm{Wb}$	reduced magnetic flux quantum

Chp. 2.1: Classical oscillators

Φ and q	branch flux across an inductor and charge on a capacitor, respectively
a	field in a resonator
A	field in a resonator, in the rotating wave approximation
c, l and r	capacitance, inductance and resistance, respectively
z_0	characteristic impedance of a resonator
ω_0	resonance frequency
H	Hamiltonian, classical mechanics
κ	loss-rate/linewidth
ϵ, Ω and θ	modulation amplitude, frequency and phase, respectively
δ	detuning of a modulation frequency
γ	parametric interaction rate
ξ	squeezing parameter
I_c	Josephson junction critical current
ζ	Kerr constant (parameterizes nonlinearity)
g and Δ	coupling rate and detuning between two resonators, respectively
ν	amplitude of the parametric interaction between two detuned resonators

Chp. 2.2: Quantum oscillators

$\hat{\Phi}$ and $\hat{q}$	branch flux and charge operators, respectively
$\hat{a}$	field operator
$\hat{x}$ and $\hat{y}$	quadrature operators
$\hat{n}$	number operator
$\hat{\sigma}_z$	Pauli z-matrix
$\hat{D}(\alpha)$	displacement operator
$\hat{H}$	Hamiltonian, quantum mechanics
$\hat{\rho}$	density matrix
$\|n\rangle$	number eigenstate
$\|0\rangle$ and $\|1\rangle$	qubit ground and excited state, respectively
$\|\alpha\rangle$	coherent state, such that $\alpha = \|\alpha\|e^{i\theta}$ and θ is an angle in phase space
ω_q	qubit frequency
χ	readout resonator dispersive shift
Δ	detuning between superconducting qubit and readout resonator
α	superconducting qubit anharmonicity
δ	detuning from resonator frequency

Chp. 3: Qubit measurement

A_x and Π_x	Krauss operator and POVM, respectively
$\|\varphi_0\rangle$ and $\|\varphi_1\rangle$	ancilla systems entangled with a qubit
$\|\alpha_0\rangle$ and $\|\alpha_0\rangle$	coherent states entangled with a qubit
T_1	qubit energy relaxation time
T_2^*	qubit dephasing (decoherence) time
T_ϕ	qubit pure dephasing time
$\|\hat{\rho}'_{01}\|$	off-diagonal density matrix element after measurement ('coherence')
η	measurement efficiency
ϵ	readout pulse amp (experimental units, e.g. voltage bias on a mixer)
$P(x\|y)$	probability of event x, given event y
F_r and F_0	readout fidelity and maximum readout fidelity, respectively
n_r and n_b	readout photon number and excess backaction photon number, respectively
ρ_b	dephasing due to excess backaction
SNR	signal-to-noise ratio
H	binary entropy
I_{acc}	accessible information of a qubit
I_{meas}	mutual information from a measurement

Chp. 4: Josephson parametric amplifiers

ω_p, ω_s and ω_i	frequency of a pump, signal and idler modes, respectively
N	number of SQUIDs in an array
I_{array}	current flowing through a SQUID array
l_{array}	linear inductance of a SQUID array
l_{res}	total linear inductance of a resonator
φ_s	amplitude of the static magnetic flux through a SQUID array
φ_m	amplitude of the time-dependent magnetic flux through a SQUID array

---

Chp. 5: Superconducting switches

Φ_u and Φ_g	TIB bias flux applied in a uniform or gradiometric manner, respectively

---

Chp. 6: The SIMBA

F_{QND}	quantum non-demolition fidelity

Appendix A: Introduction to Josephson junctions and SQUIDs

I	current flowing across a Josephson junction / SQUID / array
$I_{c,1(c,2)}$	critical current of the first (second) Josephson junction in a SQUID
L_J	Josephson inductance
$\psi_{1(2)}$	superconducting order parameter on either side of a Josephson junction
φ	phase drop across a Josephson junction / SQUID / array
$\varphi_{1(2)}$	phase drop across the first (second) Josephson junction in a SQUID
φ_{ext}	magnetic flux through a SQUID loop

Appendix C: Graph theory approach to circuit analysis

$\mathbf{S}$ and $\mathbf{Y}$	scattering and admittance matrix, respectively
$\mathbf{y}$	primitive admittance matrix
$\mathbf{A}$	adjacency matrix
n and m	number of nodes and chords in a network, respectively
v_ν	voltage on node ν
y_μ and i_μ	admittance across and current flowing across chord μ, respectively
n_p	number of ports in a network
z_0	port characteristic impedance

Chapter 1

Introduction

1.1 Motivation for quantum computing

This thesis is one small piece of the decades-long effort to advance information technology using the laws of quantum mechanics. While classical computers have revolutionized society over the past century, there are fundamental limits on the problems they can efficiently solve. This observation was epitomized by the legendary physicist Richard Feynman, who said: *"Nature isn't classical, dammit, and if you want to make a simulation of nature, you'd better make it quantum mechanical, and by golly it's a wonderful problem, because it doesn't look so easy."* In the 1980's [1, 2], Feynman was one of the first to realize that nature, which is described by quantum phenomenon such as entanglement, cannot always be reasonably modelled by a physical system which is purely classical. Since quantum computers are of course described by the laws of quantum mechanics, in a sense they represent the final frontier in computing technology. There are no known problems which *cannot* be efficiently solved on a quantum computer but *can* be efficiently solved on some other type of physically realizable computer [3, 4].

Interest in quantum computing expanded from an intellectual curiosity to an object of potential use in the 1990s, when Peter Shor made two important discoveries. First, he invented an algorithm to factor large numbers in polynomial time, a task strongly believed to be exponentially difficult (NP-complete) on a classical computer [5]. The ability to efficiently factor large numbers would allow for commonly used cryptography schemes to be easily broken. Secondly, Peter Shor and then others showed that error correction is possible on a quantum computer [6, 7, 8, 9]. The

implication of this is that it is possible, *in-principle*, to physically realize a universal, fault-tolerant quantum computer. Doing so in any way powerful enough to be generally relevant to society remains an outstanding challenge.

The current status of quantum computers, deemed the NISQ era for 'Noisy Intermediate-Scale Quantum' by John Preskill [10], is perhaps analogous to that of classical computers in the mid-20th century. There was a period when ideas from Alan Turing, John von Neumann and others had made it clear that a 'computer' was a new class of machine, and rudimentary demonstrations had even been built. If realizable at scale, such a 'computer' would be certainly be useful when applied to some specific problems, and perhaps would be useful to others in some unforeseen way. There were competing ideas for how a computer should be built: computers based on mechanical components, vacuum tubes, etc. It was not for several decades until a transistor-based computer emerged as the dominant architecture, and decades more until computers had spread to every corner of the globe and revolutionized society. Likewise, despite the impressive progress that has already been made in understanding and building quantum computers, nobody knows the best way to create a scalable one in the long-term, if doing so in a broadly useful way is even possible, and if so, the scope of what it would be used for. These open questions create uncertainty but also excitement.

1.2 The need for high quality measurement

In general, algorithms run on a quantum computers contain the following steps. First, the qubits — the basic units of quantum information —are prepared in a known state, for example the ground state $|0\rangle$. Next, a series of gates are applied, and finally, the qubits are measured. This measurement is generally projective, meaning that the qubit post-measurement state is collapsed to either the ground state $|0\rangle$ or excited state $|1\rangle$. Ideally, all of the operations in an algorithm: state preparation, single-qubit gates, multi-qubit gates and measurements, are performed with perfect fidelity. Moreover, the qubit states should not change in some unknown or unspecified way between steps.

In practice, errors occur. As the size and complexity of a quantum system increases, the fidelity of all operations in that algorithm must generally increase for it to yield a useful result. For example, suppose a measurement operation works with 90% probability, but returns an error the other 10% of the time. The chance of having no errors when measuring 10 qubits is $0.9^{10} = 0.35$ which is generally tolerable; runs of an algorithm which contain errors can simply be discarded. This strategy quickly becomes untenable in larger systems: for 100 qubits, the chance of having no errors is $0.9^{100} = 2.6 \times 10^{-5}$, and for 1000 qubits it is $0.9^{1000} = 1.7 \times 10^{-46}$. As the number of operations increases, fidelity must also increase so that an algorithm is not overwhelmed by errors.

Measurement performance is especially important for quantum error correction schemes, which generally involve the measurement of ancilla qubits [11]. Conditional on these measurement results, gates are applied to correct errors that have occurred in the data qubits. For such a procedure to succeed, measurements must generally have near-unit fidelity and be much faster than qubit decoherence times. Since ancilla qubits are repeatedly measured, measurements should be quantum non-demolition meaning that the qubit remains in its post-measurement eigenstate (rather than being kicked out of its two-level subspace, for instance). Measurement problems generally reduce the effectiveness of any quantum error correction algorithm, and can easily cause it to introduce *more* errors.

High quality qubit measurement is therefore essential to quantum computing and quantum error correction in any hardware platform. Improving the measurement of superconducting qubits motivates this thesis.

1.3 Quantum information with superconducting circuits

Superconducting systems falling within the scope of 'circuit quantum electrodynamics' (cQED) are currently one of the most promising ways to create a scalable quantum computer [12, 13]. This approach was pioneered at Yale in the mid-2000s [14, 15, 16]. In cQED, qubits are realized from superconducting, nonlinear microwave frequency resonators. Qubits are controlled and measured using microwave frequency pulses routed in and out of the base temperature of a dilution refriger-

ator, whose millikelvin temperature keeps these qubits in their quantum ground state.

This approach is a promising route towards quantum computation because qubits can have gate speeds orders of magnitude faster than their coherence times, fast and high-fidelity, qubit-specific measurement, and the promise of scalability due to their compact size and relative ease of fabrication. In other words, superconducting qubits arguably fulfill the DiVincenzo criteria [17], the features required to build a scalable quantum computer.

The transmon qubit [18], also developed at Yale in the mid-2000s, is an especially successful type of superconducting qubit. Companies including Google, IBM, Rigetti Computing, and others around the world, are all trying to build quantum computers using transmons as their data qubit [19, 20]. Other superconducting architectures built around linear cavities still make use of transmons for state preparation and measurement [21, 22].

Despite great promise, many challenges remain in implementing superconducting quantum computers. Today, the largest systems are becoming prohibitively difficult to simulate on classical computers (for example the recent demonstration of 'quantum supremacy' by Google [20]), but are not close to solving problems generally relevant to society. To do so, virtually every performance metric: e.g. coherence times, gate fidelities, measurement fidelities, must be improved by orders of magnitude. Moreover, there is the daunting technical challenge of fabricating and fitting increasingly many qubits and the hardware they require into a cryostat, and doing so in a way which doesn't degrade performance. Thousands of people around the world are working on all of these problems, and parallel challenges in other quantum computing architectures.

1.4 Introduction to superconducting qubit measurement

To place this thesis in context we review the standard approach to superconducting qubit measurement, an example of which is illustrated in Fig. 1.1. We discuss the advantages — and limitations — of this approach, and conclude with a summary of the current state-of-the-art.

Superconducting qubits are generally engineered in a dispersive architecture [15], meaning

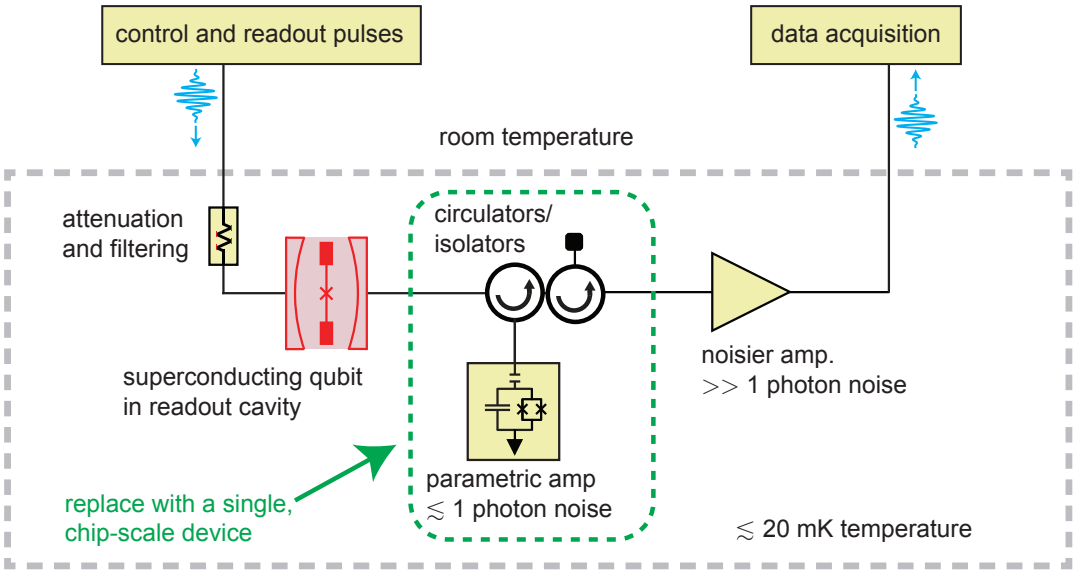

Figure 1.1: **Simplified schematic of superconducting qubit measurement**. A superconducting qubit is measured by scattering a microwave frequency pulse off of a readout cavity dispersively coupled to it. Here, this pulse is illustrated to enter the readout cavity through a weakly coupled port (left side of the red box) and exit through a strongly coupled port (right side). The pulse typically populates the cavity state with several photons. After leaving, the pulse is routed through circulators/isolators to a quantum limited parametric amplifier. Circulators/isolators are non-reciprocal devices which enforce unidirectional flow of information and prevent amplified signal and noise from the amplifier chain from entering the readout cavity. The pulse is then routed out of the cryostat, through further amplification, and to a digitizer at room temperature. The work in this thesis replaces the setup boxed in green with a single, chip-scale device called a SIMBA (a Superconducting, Isolating, Modular Bifurcation Amplifier) [23]. The SIMBA has state-of-the-art performance and the promise of further improvement.

that the qubit is weakly[1] coupled to a second, linear resonator. This resonator inherits some nonlinearity from the qubit, such that its resonance frequency shifts by $\pm\chi/2\pi$ depending on if the qubit is in the ground or excited state. A typical transmon has $\chi/2\pi$ order 1 MHz, with a resonator frequency of order 10 GHz and a detuning between the qubit and resonator of 1 GHz or more.

An advantage of the dispersive architecture is that the qubit is well isolated from its environment, which is a source of loss and noise. Its only explicit connection to any dissipative load is through the external coupling of the readout cavity, which is already coupled weakly to the qubit. The qubit can still be measured, however, by detecting microwave frequency photons scattered off

[1] Meaning $g/\Delta \ll 1$ with g the coupling between the resonator and qubit, and Δ their detuning. See Chp. 2.1.6.

of the cavity. An appropriate readout pulse will acquire a different phase and/or amplitude shift depending on if the qubit is in the ground state or excited state. This procedure is called 'dispersive readout' [15, 24] and is discussed quantitatively in Chp. 2.2.4.3. For now, we care that the problem of measuring the qubit state has been mapped to detecting this readout pulse.

High quality detection of the readout pulse is complicated by the fact that it typically contains less than 10 photons, an extremely weak signal by the standards of conventional microwave electronics. Yet high-fidelity readout relies on the precise discrimination of this signal. To do so, the readout pulse must first be routed to an amplifier which adds little noise compared to the amplitude of the readout pulse. Superconducting parametric amplifiers are suitable for this purpose.

1.4.1 Introduction to quantum limited amplification

Realized by Carlton Caves in the 1980s, quantum mechanics sets a fundamental limit on the noise that can be added by any linear amplification process [25, 26]. Analogous to the uncertainty principle, the product of the noise added along each quadrature[2] of the amplified field must be greater than or equal to a minimum non-zero value.

In general there are two classes of quantum limited parametric amplifiers. An ideal phase-*sensitive* amplifier can approach noiseless amplification of one quadrature of the electromagnetic field, while adding increased noise to the other quadrature. An ideal phase-*preserving* amplifier amplifies both quadratures equally, adding a quarter quanta of noise to each.

That quantum mechanics places a fundamental limit on amplification is of profound importance for the measurement of weak signals, for example the single photon level microwave pulses used in superconducting qubit measurement. On one hand, there is a limit to how well any amplifier can possibly perform. Advantageously however, this limit is *zero* when using a phase-sensitive amplifier to measure a single oriented along one quadrature, and only a half quanta of added noise when using a phase-preserving amplifier.

Quantum limited amplifiers are readily engineered in superconducting systems by making

[2] See Chp. 2.2.3 for a definition of 'quadrature'.

use of the nonlinearity of the Josephson junction [27, 28, 29, 30, 31]. The basic theory behind these amplifiers is discussed in Chp. 2.1.4, and the specific parametric amplifier used in this work is discussed in Chp. 4.

1.4.2 Isolating qubits from measurement backaction

In addition to low noise measurement, it is important to keep a qubit well isolated in order to maintain the delicate quantum information preserved in the qubit's phase coherence. Dephasing[3] will introduce errors into any quantum computing protocol. Photons coupled to the qubit will dephase it, regardless of if these photons come from a measurement pulse or a noise source. Exposure to too high a photon number can also kick a qubit out of its two-level subspace [32, 33]. Fortunately, it is possible to couple a qubit to a measurement chain without exposing it to extra noise.

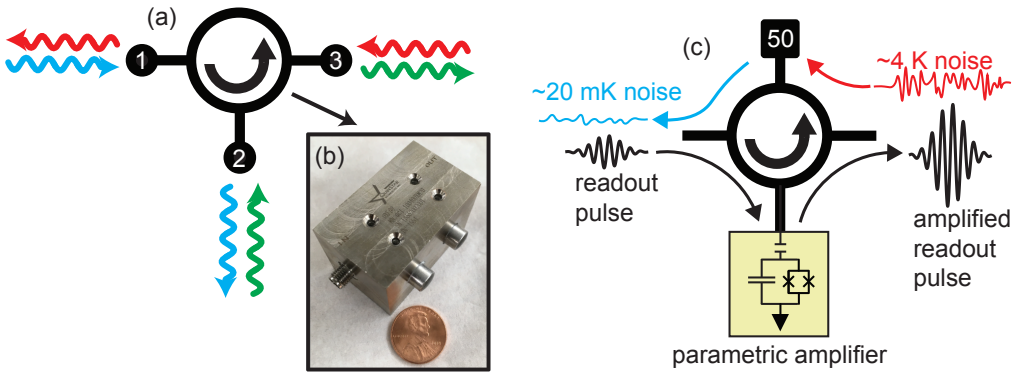

Figure 1.2: **The role of ferrite circulators/isolators**. (a) Schematic of a 3-port circulator: a signal incident on port 1, 2 or 3 is routed to port 2, 3 or 1, respectively. (b) Photograph of a commercial cryogenic isolator (a 4-port circulator, with matched terminations on two ports). (c) Illustration of a circulator used in conjunction with a parametric amplifier. A pulse incident on the left port is routed to a 1-port parametric reflection amplifier. This pulse is amplified and then routed by the circulator to a measurement chain connected to the right port. The measurement chain spits noise back to the circulator, which is dissipated in a matched load thermalized to the base temperature of a cryostat (black square, equivalent to a 50 Ohm resistor). Noise consistent with the base temperature of the cryostat is then routed back to the left port. The circulator therefore protects anything connected to the left port (e.g. a readout cavity containing a qubit), from amplifier backaction and the added noise of the measurement chain.

[3] See Chp. 3.1.3 and 3.1.4 for a definition of dephasing.

In a typical measurement, circulators and/or isolators[4] protect the qubit from the excess backaction caused by the measurement chain. Circulators/isolators are nonreciprocal devices, meaning that they enforce a unidirectional flow of information, Fig. 1.2a [34]. A circulator can route a signal output from a qubit readout cavity into a parametric amplifier, Fig. 1.2c, and then route the amplified signal to the rest of a measurement chain and ultimately out of the cryostat, rather than returning to the qubit. This keeps the qubit from being exposed to the order one-hundred photon amplified signal. Circulators and/or isolators also route the noise from the next amplifier in the measurement chain to a cold bath, rather than back into the qubit-cavity system. For a standard HEMT (high-electron-mobility-transistor) amplifier, the temperature of the noise it spits back to the base temperature of the cryostat is approximately 4 Kelvin or greater, corresponding to thermal state with a mean photon number of order ten or more at microwave frequencies.

The commercial circulators/isolators used in cryogenic microwave experiments break Lorentz reciprocity using ferromagnetic materials [34]. An example of one of these ferrite devices is shown in Fig. 1.2b. Magnetic shielding is included on the outside of this isolator to prevent the permanent magnetic field it produces from disrupting any superconducting electronics, which can be sensitive to magnetic fields on the order of a single flux quanta or less. Advantageously, commercial circulators/isolators are passive devices (requiring no external bias), have far more power handling than is needed in any cryogenic experiment, and have octave bandwidth.

Use of ferrite circulators/isolators combined with parametric amplifiers works reasonably well for superconducting qubit readout. For example, superconducting qubit readout faster than 100 ns with greater than 99% fidelity has been demonstrated using such hardware [35], with higher fidelities in longer measurements [36, 37]. However, there is a clear need for improvement as the scale and requirements of superconducting qubit systems increase.

[4] An isolator is an N-port circulator with $N-2$ ports connected to matched loads.

1.4.3 Measurement hardware areas for improvement

As superconducting qubits have developed, so has their measurement and the requisite hardware. Efforts toward fast, high-fidelity single-shot readout of superconducting qubits began shortly after their advent, for example Refs. [27, 38, 39]. Today, such efforts include the improvement of both amplifiers and circulators/isolators, with the broader goal of improving measurement performance and scalability.

For over a decade, superconducting, microwave parametric amplifiers have been shown to achieve both high gain and added noise near the quantum limit. These approaches are often based on resonant modes made nonlinear by the participation of a Josephson junction, for example Josephson parametric amplifiers (JPAs) [28, 40, 29] or the Josephson parametric converters (JPC) [30, 41]. More recent research efforts have included improving bandwidth [31, 42, 43, 44, 45], improving the power handling and ease of calibration [46, 47], and integrating these amplifiers more closely with superconducting qubits [48, 49, 50]. In particular, Josephson travelling wave parametric amplifiers (JTWPAs) [51, 31, 52, 53, 54] and related technology based on the nonlinearity from kinetic inductance [55, 56] offer added noise that can approach the quantum limit combined with $> 20\,\mathrm{dB}$ of gain over several GHz of bandwidth. Room for improvement remains and similar technology can be engineered for other applications such as astronomical detectors [57]. Arguably however, superconducting microwave amplifiers are an increasingly mature technology.

Improving the requisite circulators/isolators used in conjunction with parametric amplifiers is a separate challenge [58]. Despite desirable features, ferrite devices have limited isolation, unavoidable loss, and centimeter-scale size. Limited isolation (typically specified at 18 dB per circulator) requires that several circulators be used in front of each parametric amplifier, increasing loss between the amplifier and qubit. This lowers the *efficiency* of the measurement chain,[5] meaning greater loss before amplification or equivalently greater added noise during amplification. Ferrite circulators cannot be readily integrated on-chip with superconducting qubits due to their permanent magnetic fields, and the separate packaging they require is an additional source of loss. Finally,

[5] See Chp. 3.3 for a precise definition of efficiency.

fitting so many bulky circulators/isolators at the base temperature stage of a cryostat is an eventual bottleneck towards systems containing thousands or more individually measurable qubits.

In recognition of these problems, beginning in the mid-2010s the superconducting microwave circuit community has attempted to engineer *superconducting* circulators/isolators [59, 60, 61, 62] and/or directional amplifiers [63, 64, 65, 66]. Such devices must actively break Lorentz reciprocity using various bias tones, rather than using permanent magnetic fields [67]. These efforts have been paralleled by a (larger scale) telecom-focused effort to engineer active, chip-scale circulators using conventional transistor technology and operated at room-temperature [68].

Despite the added requirement of bias tones and/or nonlinearity, active superconducting circulators/isolators can in-principle outperform ferrites. Active circulators can have octave-scale bandwidth and high isolation [43], combined with minimal loss [45]. However, engineering a superconducting circulator with such performance is a difficult. In particular, the device in Ref. [45] is a design for a low-loss, broadband superconducting circulator that requires long, low-loss delay lines and fast, superconducting crossover switches with large on/off ratios. Long delay lines and other types of broadband switches have already been developed (see Table 5.1), but combining them together and demonstrating high-quality circulation in a superconducting system has not yet been achieved.

Alternatively, excellent performance has been demonstrated in narrow band superconducting circulators/directional-amplifiers [63, 64, 60, 65, 61, 62, 66]. Such devices contain three or more resonant modes with nonlinearity introduced by Josephson junctions. Non-reciprocity and/or gain can be realized by pumping the circuit at the difference and/or sum frequencies of these modes. State-of-the-art superconducting qubit readout has recently been demonstrated with such devices [69, 70, 71]. Despite impressive performance, these approaches suffer from narrow bandwidth limited by the high quality-factor of the modes, along with multiple requisite bias tones which must be carefully synchronized. These limitations manifest in the fact that to-date, no superconducting technology has been broadly adopted as an alternative to ferrites. All large-scale superconducting quantum experiments today still provide isolation exclusively using ferrites.

1.5 Comparison of this thesis to related work

The work forming the bulk of this thesis, Ref. [23], is also motivated by a desire to replace the ferrite circulators/isolators used in superconducting qubit measurements. Ref. [23] differs from other approaches in that it does not try to engineer a circulator or isolator, and that it is not designed to operate continuously. Instead, both isolation and pulsed directional amplification is achieved by the coordinated operation of superconducting switches. These switches, combined with a parametric amplifier, are integrated into a single-chip scale devices called a 'Superconducting Isolating Modular Bifurcation Amplifier' (SIMBA), discussed in detail in Chp. 6. Here, we will summarize the SIMBA's performance in comparison to other work.

In this comparison, we focus on the figures of merit reported in Table. 1.1: measurement efficiency η, excess backaction n_b, the maximum readout fidelity F_0, and the time it takes to complete the measurement.[6] Qualitatively, measurement efficiency η is the fraction of readout signal lost between the qubit and amplifier, assuming noiseless amplification (added noise also decreases efficiency). 'Excess backaction' in Table. 1.1 refers to the number of photons a qubit is exposed to due to measurement in excess of those in the readout. The presence of such photons indicates imperfect isolation between the qubit and amplifier. Both efficiency and backaction are discussed in detail in Chp. 3. Maximum readout fidelity is essentially the ability of the detector to discriminate the state of the qubit. This is defined as $F_0 = 1 - p_0 - q_0$, where p_0 and q_0 are the error probabilities of a projective measurement when the qubit is prepared in the excited or ground state, respectively.

The highest measurement efficiency which has thus-far been reported in a circuit quantum electrodynamics system is $\eta = 0.80$ in Ref. [49]. In Ref. [49], a qubit is dispersively coupled to a readout cavity which shares functionality as a phase-sensitive pumped parametric amplifier, with no non-reciprocal elements between the qubit and amplifier. The highest efficiencies that have

[6] Another important metric is how quantum-non-demolition (QND) a measurement is (how well a qubit remains in the measured eigenstate) [72]. Dispersive readout of superconducting qubits is understood to be QND [15, 24] and is not characterized in most of the references in Table. 1.1. Additionally, the amplifier bandwidth, ease of calibration, and requisite number of bias lines (along with the bandwidth of the bias signals), are also important considerations from the standpoint of scalability.

Table 1.1: **Comparison to related work.** Recent demonstrations of superconducting qubit readout in which the measurement efficiency η is characterized. Many recent experiments which make use of ferrite circulators/isolators have demonstrated maximum readout fidelities F_0 of 0.95 or greater, readout times of several hundred nanoseconds, and measurement efficiencies between $\eta = 0.1$ and $\eta = 0.6$. All works in this table use Josephson-junction based parametric amplifiers, which are operated either in a phase-*sensitive* (S) or phase-*preserving* (P) manner. Note that (excepting Ref. [36]) the works labelled (P) generally use a definition of measurement efficiency which goes to unity when using a phase-preserving amplifier, a different definition than that used by works which use a phase-sensitive amplifier (see Chp. 3.3.1).

Reference	Amplifier	Efficiency, η	Excess backaction n_b, (photons)	Readout fidelity, F_0	Readout duration
Rosenthal *et al.* (2021), [23]	SIMBA (S)	0.70	0.66	0.955	265 ns
Lecocq *et al.* (2021), [71]	FPJA (S)	0.72	0.07	0.97	350 ns
Andersen *et al.* (2020), [73]	TWPA (P)	$0.15 - 0.30$	N/A	$0.978 - 0.994$	$300 - 400$ ns
Abdo *et al.* (2020), [70]	JDA (P)	~ 0.2	0.002	0.92	1000 ns
Peronnin *et al.* (2020), [74]	TWPA (P)	0.11	N/A	0.95	220 ns
Andersen *et al.* (2019), [73]	TWPA (P)	0.24	N/A	$0.987 - 0.992$	200 ns
Abdo *et al.* (2019), [69]	JPC (P)	~ 0.3	0.01	0.9	200 ns
Touzard *et al.* (2019), [75]	SPA (S)	0.6	N/A	0.978	870 ns
Eddins *et al.* (2019), [49]	JPA (S)	0.80	$\gg 1$	N/A	N/A
Heinsoo *et al.* (2018), [76]	TWPA (P)	$0.43 - 0.52$	N/A	$0.936 - 0.988$	250 ns
Bultink *et al.* (2018), [77]	TWPA (P)	0.165	N/A	N/A	N/A
Eddins *et al.* (2018), [78]	JPA (S)	0.38	N/A	N/A	N/A
Walter *et al.* (2017), [35]	JPD (S)	0.75	N/A	0.992	88 ns
Macklin *et al.* (2015), [31]	TWPA (P)	0.49	N/A	0.967	100 ns
Jeffrey *et al.* (2014), [36]	JPA (P)	0.13	N/A	0.998	140 ns

yet been reported *with* considerable ferrite-based isolation between the qubit and amplifier are $\eta = 0.75$ in Ref. [35],[7] $\eta = 0.72$ in Ref. [71] and $\eta = 0.70$ in Ref. [23]. In other experiments using ferrite circulators/isolators before a parametric amplifier, the measurement efficiency falls between $\eta = 0.1$ and $\eta = 0.6$. Ref. [71] is a chip-scale 'FPJA'-style amplifier which synthesizes directional amplification with the use of several microwave frequency pumps and the sum and difference frequencies between several microwave modes. Ref. [23] introduces the SIMBA, the subject of this thesis.

The technologies in Refs. [70, 23, 71] are all promising alternatives to ferrite circulators/isolators.

[7] Note that the measurement in Ref. [35] (which uses ferrite circulators/isolators to provide isolation) calibrates η differently than the other works in Table. 1.1 which potentially complicates a direct comparison. In Ref. [35], η is estimated by determining the power spectral density of a readout pulse using the ac-Stark shift of the qubit [16], and comparing this to the power spectral density of a measured signal. Other references in Table 1.1 directly measure the decoherence of a qubit due to a weak measurement (see Chp. 3).

These devices result from years of preliminary work, but have only recently been developed to the point of demonstrating high-quality readout of a superconducting qubit without any ferrite/circulators between the qubit and amplifier. SIMBAs have the advantage, compared to the devices in Refs [69, 66, 70, 71], of requiring only one microwave bias tone and the promise of relative ease of calibration. The limitations of the SIMBA in Ref. [23] are well understood and not inherent to the concept itself (see Chp. 6.3). As such, SIMBA amplifiers based off of the device in Ref. [23] are a promising avenue towards the widespread replacement of ferrite circulators/isolators in superconducting quantum information experiments.

1.6 Thesis organization

The remainder of this thesis is organized as follows: Chp. 2 is a pedagogical introduction to simple-harmonic oscillators in the context of superconducting circuits. This includes damping, parametric gain, and coupled resonators treated classically. It also includes introductions to quantum optics, superconducting qubits, and the formalism of input-output theory. Chp. 3 discusses qubit measurement, beginning with a formal definition of measurement in quantum mechanics and developing this to show how measurement-induced dephasing can be used to calibrate the efficiency of a measurement. Chp. 4 overviews Josephson-parametric amplifiers (JPAs), the specific type of amplifier integrated within a SIMBA. Chp. 5 describes superconducting switches based on a 'tunable inductor bridge' (TIB) design [79], also integrated into a SIMBA. Chp. 6 describes the SIMBA itself and characterizes its use for superconducting qubit readout. Finally, Chp. 7 presents several avenues for future research.

Chapter 2

Oscillators

This chapter begins with the canonical example of a classical, simple harmonic oscillator. This simple model is extended to include loss, parametric gain, nonlinearity and coupling to another oscillator. A quantum description is then given, along with an introduction to superconducting qubits. Finally, coupling of an oscillator to its environment is reviewed using the framework of input-output theory. These examples are useful for understanding the work presented later in this thesis.

2.1 Classical oscillators

This section deals with classical oscillators. Here 'classical' refers to oscillators described by scalar-valued variables which commute, such as position and momentum.[1] The examples discussed in this section are useful for building intuition for their quantum counterparts. In many systems, classical dynamics alone are a sufficient description.

2.1.1 LC-oscillator

A simple harmonic oscillator is formed from an inductor-capacitor circuit, Fig. 2.1a. Following from Maxwell's equations its equations of motion are

$$\dot{\Phi} = \frac{1}{c} q, \qquad \dot{q} = -\frac{1}{l}\Phi. \tag{2.1}$$

[1] More formally, classical coordinates satisfy the Poisson bracket. See Refs. [80, 81] for more information.

where c is a lumped-element capacitance and l is a lumped-element inductance. We have written these equations using the time-dependent branch flux $\Phi(t) = I_l(t) \times l$ across the inductor such that $\Phi(t) = \int_{-\infty}^{t} dt' v(t')$, where $v(t)$ is the voltage drop across the inductor and $I_l(t)$ is the current flowing through it. We also use the time-dependent charge $q(t) = v(t) \times c$ across the capacitor such that $q(t) = \int_{-\infty}^{t} dt' I_c(t')$ where $I_c(t)$ is the current flowing through it. Kirchhoff's current law gives the relation $I_c + I_l = 0$.

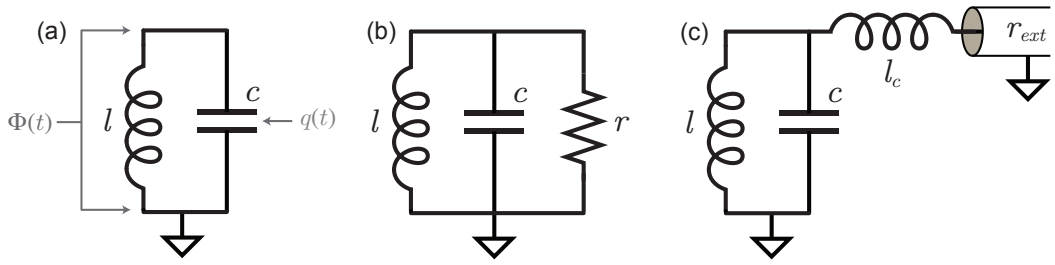

Figure 2.1: **A simple harmonic oscillator**. (a) An LC-oscillator ('LC' named for inductor 'L' and capacitor 'C') can be made from an inductance l to ground, in parallel with a capacitance c to ground. The branch flux $\Phi(t)$ across the inductor and charge $q(t)$ on the capacitor plates will oscillate in time at the circuit's resonance frequency. (b) A resistor r adds loss. (c) Coupling to a transmission line of characteristic impedance r_{ext} also adds loss (the transmission line symbol is assumed to be terminated in a matched load, and is then equivalent to a resistor of value r_{ext} to ground).

It is useful to transform these equations to normal mode form, such that the two first-order differential equations describing the oscillator's dynamics are complex conjugates of each other. To do so, we introduce the variable $a(t)$ and its complex conjugate $a^\dagger(t)$, defined by the transformation[2]

$$a = \frac{1}{\sqrt{2\hbar}} \left(\frac{\Phi}{\sqrt{z_0}} + i\sqrt{z_0} q \right), \tag{2.2}$$

where we have introduced the characteristic impedance of the resonator $z_0 = \sqrt{l/c}$.

After this transformation, the equation of motion for the circuit in Fig. 2.1 becomes

$$\dot{a} = -i\omega_0 a, \tag{2.3}$$

which has the solution $a(t) = Ae^{-i\omega_0 t}$, along with its complex conjugate. Here, A is a *phasor*, a

[2] Despite our introduction of $\hbar$, this analysis remains *classical* such that a and $a^\dagger$ (or Φ and q) commute.

complex number which specifies the amplitude and phase of oscillations in a frame rotating at the resonance frequency ω_0.

Notice that from the classical Hamiltonian $H = \Phi^2/2l + q^2/2c$, we find the energy stored in the oscillator to be

$$H = \hbar\omega_0 A^\dagger A, \tag{2.4}$$

where $\omega_0 = 1/\sqrt{lc}$ is the oscillator's resonance frequency.

2.1.2 LC-oscillator with damping

Eq. 2.1 is modified by the inclusion of loss. In Fig. 2.1b, this is modelled as a resistor r to ground in parallel with the inductor and capacitor. The equations of motion become

$$\dot{\Phi} = \frac{1}{c}q, \qquad \dot{q} = -\frac{1}{l}\Phi - \frac{1}{rc}q. \tag{2.5}$$

Again using Eq. 2.2 to transform to normal coordinates, Eq. 2.5 becomes

$$\dot{a} = -i\omega_0 a - \frac{\kappa}{2}\left(a - a^\dagger\right) \tag{2.6}$$

and its complex conjugate. Here, $\kappa = (rc)^{-1}$ is a loss rate.

It can be useful to rewrite Eq. 2.6 in the rotating frame, taking $a(t) = A(t)e^{-i\omega_0 t}$ such that $\dot{a} = \left(\dot{A} - i\omega_0 A\right)e^{-i\omega_0 t}$ by the product rule. Here, $A(t)$ is the now time-*dependent* phasor describing the oscillator field in the rotating frame. Substituting these relationships into Eq. 2.6 gives $\dot{A} = -\frac{\kappa}{2}A + \frac{\kappa}{2}e^{2i\omega_0 t}A^\dagger$. Neglecting the fast-rotating term $e^{2i\omega_0 t}$ simplifies the equations of motion to

$$\dot{A} = -\frac{\kappa}{2}A \tag{2.7}$$

and its complex conjugate.

Eq. 2.7 has the solution $A(t) = A_0 e^{-\kappa t/2}$, where A_0 is a phasor describing the system at $t = 0$. The energy stored in a circuit is proportional to the modulus-squared of its field, which exponentially decays at rate κ. It is typical to parameterize this decay by the *quality factor*,

$$Q = \frac{\omega_0}{\kappa}. \tag{2.8}$$

Physically, Q is the number of cycles it takes for energy in the oscillator to decay by e^{-1}.

2.1.3 LC-oscillator with damping by an external load

Loss may also be introduced by coupling to a dissipative load, for example the circuit in Fig. 2.1c. Here, this dissipative load is modelled by a transmission line of characteristic impedance r_{ext} which is terminated in a matched load, equivalent to a resistor to ground of the same value. In Fig. 2.1c this load is connected to the resonator through an inductance but equivalent physics arises for a capacitive coupling (or any high impedance).

In the limit of weak coupling $l/l_c \ll 1$ and in the rotating wave approximation, the equations of motion for the field in the resonator in Fig. 2.1c become

$$\dot{A} = -\frac{\kappa_{ext}}{2}A, \qquad \kappa_{ext} = \frac{r_{ext}}{l}\left(\frac{l}{l_c}\right)^2, \tag{2.9}$$

and its complex conjugate. Notice that Eq. 2.9 takes exactly the same form as Eq. 2.7, but with a loss rate dependent on the small parameter l_c/l describing how strongly coupled the resonator is to the dissipative load. Note that if the coupling inductor l_c is replaced by a coupling capacitor c_c then in the limit of $c_c/c \ll 1$, the external loss rate becomes $\kappa_{ext} = \frac{r_{ext}}{l}\left(\frac{c_c}{c}\right)^2$.

2.1.4 LC-oscillator with parametric gain

The field in a resonator can be amplified by modulating the circuit's resonance frequency ω_0 at twice its natural value. Consider a harmonic oscillator now with a time-*dependent* inductance $l(t)$ as in Fig. 2.2a

$$l(t) = \frac{l_0}{1 + \epsilon\cos(\Omega t + \theta)}. \tag{2.10}$$

Here, l_0 is a constant inductance, and Ω and θ are the frequency and phase of the modulation, respectively. The modulation amplitude ϵ is specified by the dimensionless parameter $0 \leq |\epsilon| < 1$.

The resulting equations of motion are identical to those in Eq. 2.5, but now with a time-dependent inductance $l(t)$:

$$\dot{\Phi} = \frac{1}{c}q, \qquad \dot{q} = -\frac{1}{l(t)}\Phi - \frac{1}{rc}q. \tag{2.11}$$

We again transform Eq. 2.11 to normal coordinates using Eq. 2.2, where now $z_0 = \sqrt{l_0/c}$. This gives

$$\dot{a} = -i\omega_0 a - \frac{\kappa}{2}\left(a - a^\dagger\right) - i\gamma\left(a + a^\dagger\right)\cos\left(\Omega t + \theta\right) \tag{2.12}$$

and its complex conjugate. Eq. 2.12 is identical to the damped harmonic oscillator in Eq. 2.6, but now with an extra term proportional to $\gamma = \epsilon\omega_0/2$.

We consider modulation near twice the oscillator's natural resonance frequency such that

$$\Omega = 2\omega_0 + 2\delta, \tag{2.13}$$

where δ is a detuning. Then, we transform Eq. 2.12 to a frame rotating at half the modulation frequency such that $a(t) = A(t)e^{-i\Omega t/2}$. Neglecting fast-rotating terms, the equations of motion simplify to

$$\dot{A} = -\frac{\kappa}{2}A + i\delta A - i\frac{\gamma}{2}e^{-i\theta}A^\dagger \tag{2.14}$$

and its complex conjugate. For a boundary condition $A(0) = 1$ and $\dot{A}(0) = 0$ at $t = 0$, maximum parametric amplification or de-amplification is achieved when $\theta = -\pi/2$ or $\theta = \pi/2$, respectively. This can be seen in Fig. 2.2b for the case when pump detuning and loss are both set to zero. This parametric process is phase-*sensitive*, as it depends on the modulation phase θ.

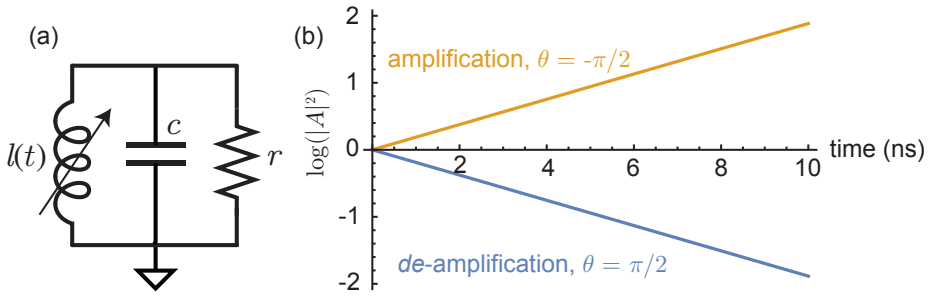

Figure 2.2: **A simple parametric oscillator**. (a) Modulating the frequency of a simple harmonic oscillator near twice its natural resonant frequency ω_0 can enable parametric gain. (b) Solutions to Eq. 2.14 are plotted for $\delta = 0$, loss $\kappa = 1/rc$ set to zero, and $\gamma/2\pi = 30$ MHz, with a boundary condition $A(0) = 1$ and $\dot{A}(0) = 0$ at $t = 0$. The energy in the oscillator, proportional to $|A(t)|^2$, is plotted on a logarithmic scale. This process is phase-*sensitive*: changing the phase of the initial field $A(t = 0)$ changes which angle θ causes amplification/de-amplification.

The Hamiltonian describing the parametrically modulated cavity in Fig. 2.2 is $H(t) = \Phi^2/2l(t) + q^2/2c$ where now the inductance is time-dependent given by Eq. 2.10, or equivalently $H = \hbar\omega_0 a^\dagger a + \Phi^2 \epsilon \cos(\Omega t + \theta)/2l_0$, where the second term describes parametric gain. Taking $\Omega = 2\omega_0$ and going to a rotating frame, this simplifies to:

$$H = \hbar\omega_0 A^\dagger A + \frac{\hbar}{2}\left(\xi A^2 + \xi^* A^{\dagger 2}\right), \tag{2.15}$$

where $\xi = \epsilon\omega_0 e^{i\theta}/4 = \gamma e^{i\theta}/2$ and fast-rotating terms are neglected. The second term on the right-hand side of Eq. 2.15 is called the *squeezing* Hamiltonian [82].

2.1.5 LC-oscillator with nonlinearity

In the model for parametric gain shown in Fig. 2.2b, energy in the pumped oscillator increases to infinity. In any physical process, nonlinear effects will eventually prevent this from happening. In superconducting systems this nonlinearity can be *engineered* using a Josephson junction, Fig. 2.3.

The relationship between current and branch flux across a Josephson junction is: $I = I_c \sin(2\pi\Phi/\Phi_0)$, where I_c is the junction's critical current (see Appx. A.1 for details) and $\Phi_0 = h/2e$ is the magnetic flux quantum. The equations of motion for the circuit in Fig. 2.3 are identical to those of Eq. 2.5, but with an extra term describing current flowing across the Josephson junction:

$$\dot{\Phi} = \frac{1}{c}q, \qquad \dot{q} = -\frac{1}{l}\Phi - \frac{1}{rc}q - I_c \sin\left(\frac{2\pi\Phi}{\Phi_0}\right). \tag{2.16}$$

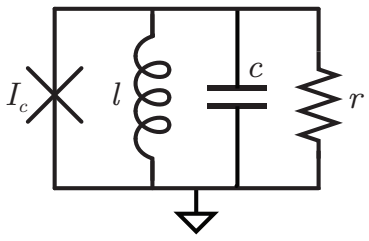

Figure 2.3: **A nonlinear oscillator**. In this nonlinear RLC-oscillator, part of the inductance comes from a Josephson junction ($\times$ symbol) parameterized by its critical current I_c. The Josephson junction behaves as a nonlinear inductor (see Appx. A).

We transform Eq. 2.16 to normal mode form and expand in the limit where $|\Phi/\Phi_0| \ll 1$ to get,

$$\dot{a} = -i\omega_0 a - \frac{\kappa}{2}\left(a - a^\dagger\right) + i\frac{\zeta}{3}\left(a + a^\dagger\right)^3, \tag{2.17}$$

where

$$\zeta = \frac{(2e)^2}{\hbar}\frac{z_0^2}{8l_J}, \qquad l_\mathrm{J} = \frac{\Phi_0}{2\pi I_c}. \tag{2.18}$$

In Eq. 2.18, ζ parameterizes the nonlinearity of the oscillator and l_J is the Josephson inductance (the linear inductance associated with the Josephson junction). Note that in Eq. 2.18 and Eq. 2.19 the resonance frequency and characteristic impedance are modified from their values in previous sections to now be $\omega_0 = 1/\sqrt{l_\mathrm{res}c}$ and $z_0 = \sqrt{l_\mathrm{res}/c}$, respectively, where $l_\mathrm{res} = (1/l + 1/l_\mathrm{J})^{-1}$ is the combination of both the Josephson inductance l_J and the other linear inductance l. Next, we transform Eq. 2.18 to a frame rotating at the resonance frequency ω_0, giving

$$\dot{A} = -\frac{\kappa}{2}A + i\zeta\left|A\right|^2 A \tag{2.19}$$

along with its complex conjugate.

Finally, the oscillator's Hamiltonian is $H = \Phi^2/2l + q^2/2c + E_J\left[1 - \cos\left(\frac{2\pi\Phi}{\Phi_0}\right)\right]$, where $E_J = I_c\Phi_0/2\pi$ is the Josephson energy [81, 83]. Going to normal mode form and again expanding in the limit where $|\Phi/\Phi_0| \ll 1$ gives the Hamiltonian,

$$H = \hbar\omega_0 A^\dagger A - \frac{\hbar\zeta}{2}\left(A^\dagger A\right)^2, \tag{2.20}$$

where fast-rotating terms are neglected, and the resonance frequency ω_0 has been renormalized to account for the linear inductance of the Josephson energy.

Eq. 2.20 is identical to the Hamiltonian of a simple harmonic oscillator, Eq. 2.4, but with an extra term added to account for the resonator's nonlinearity.[3] The meaning of the nonlinearity ζ, also known as the Kerr-constant, becomes clear: the oscillator's resonance frequency $\omega_0 - \zeta a^\dagger a/2$ is shifted by the modulus-squared of the field inside of it, times the Kerr constant.[4]

[3] The Duffing oscillator is a system described by Eq. 2.20. See Refs. [84, 85] for a thorough theoretical treatment in the context of superconducting circuits.

[4] Note that here, the Kerr-shift is defined such that a positive value of ζ denotes a negative shift in the resonance frequency.

2.1.6 Coupled oscillators

Many physical systems are described by two or more resonators coupled together. In this section, we consider two RLC-oscillators coupled by an inductance l_g as in Fig. 2.4a.[5]

Four coordinates are required to describe these two oscillators: $\Phi_A(t)$, $\Phi_B(t)$ the branch fluxes across inductors l_A and l_B, respectively, and $q_A(t)$ and $q_B(t)$, the charges on the plates of capacitors c_A and c_B, respectively. Four coupled first-order differential equations describe the relationship between these parameters:

$$\dot{\Phi}_A = \frac{1}{c_A} q_A, \tag{2.21}$$

$$\dot{q}_A = -\left(\frac{1}{l_A} + \frac{1}{l_g}\right)\Phi_A - \frac{1}{r_A c_A} q_A + \frac{1}{l_g}\Phi_B, \tag{2.22}$$

along with two analogous equations specifying $\dot{\Phi}_B$ and $\dot{q}_B$.

We allow the bare resonant frequencies of the two oscillators $\omega_A = 1/\sqrt{l_A c_A}$ and $\omega_B = 1/\sqrt{l_B c_B}$ to be different, but for simplicity enforce their characteristic impedances to be equal such that $z_0 = \sqrt{l_A/c_A} = \sqrt{l_B/c_B}$. Doing so and specifying the loss rates of each resonator $\kappa_A = (r_A c_A)^{-1}$ and $\kappa_A = (r_B c_B)^{-1}$, the circuit equations of motion become

$$\dot{\Phi}_A = \omega_A z_0 q_A, \tag{2.23}$$

$$\dot{q}_A = -\left(\frac{\omega_A}{z_0} + \frac{1}{l_g}\right)\Phi_A - \kappa_A q_A + \frac{1}{l_g}\Phi_B, \tag{2.24}$$

along with two analogous equations for $\dot{\Phi}_B$ and $\dot{q}_B$. We then transform to the normal coordinates $a = \frac{1}{\sqrt{2\hbar}}\left(\Phi_A/\sqrt{z_0} + i\sqrt{z_0} q_A\right)$ and $b = \frac{1}{\sqrt{2\hbar}}\left(\Phi_B/\sqrt{z_0} + i\sqrt{z_0} q_B\right)$, giving

$$\dot{a} = -i\omega_A a - ig\left(a + a^\dagger - b - b^\dagger\right) - \frac{\kappa_A}{2}\left(a - a^\dagger\right), \tag{2.25}$$

$$\dot{b} = -i\omega_B b - ig\left(b + b^\dagger - a - a^\dagger\right) - \frac{\kappa_B}{2}\left(b - b^\dagger\right), \tag{2.26}$$

and their complex conjugates. Here, we have defined the coupling rate $g = z_0/2l_g$.

[5] Similar dynamics emerge if this coupling inductor is replaced by a coupling capacitor. Recall that at a given frequency ω, there exists some capacitor c_g whose impedance has the same magnitude as that of l_g such that $j\omega l_g = -1/j\omega c_g$.

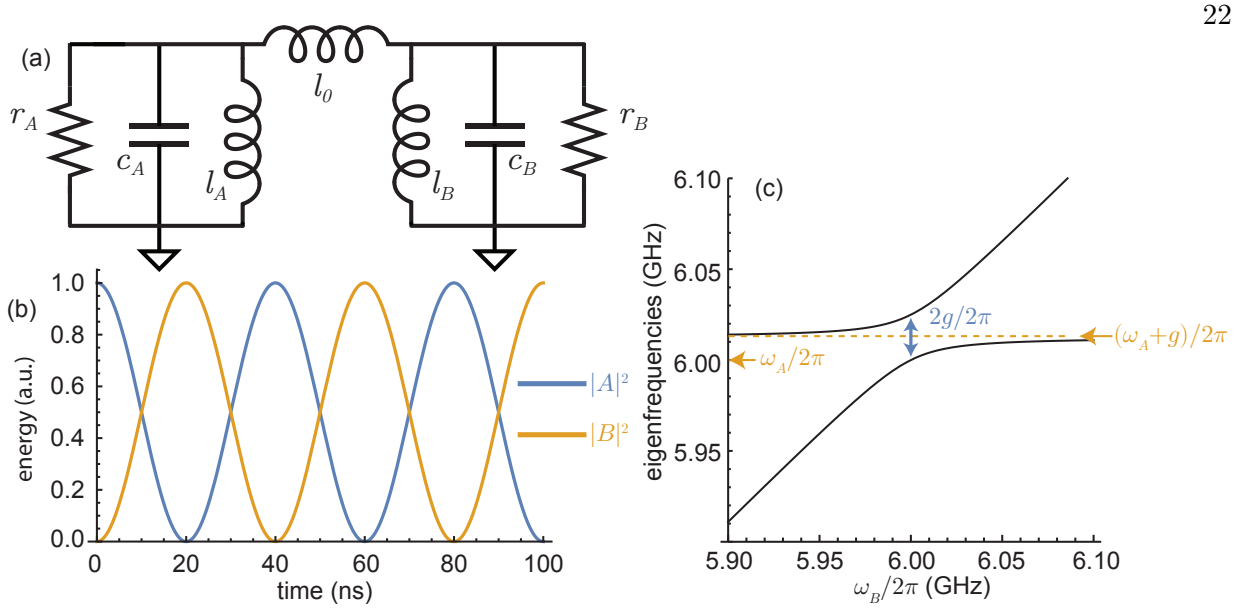

Figure 2.4: **Two coupled oscillators**. (a) Two resonators labelled 'A' and 'B' are coupled by an inductance l_g. For simplicity, we work in a limit where each oscillator has the same characteristic impedance $z_0 = \sqrt{l_A/c_A} = \sqrt{l_B/c_B}$. (b) Solutions to the equations of motion for this circuit taking $\Delta = 0$ and $g = z_0/2l_g = 2\pi \times 12.5$ MHz, with loss set to zero such that $\kappa_A = \kappa_B = 0$ and a boundary condition at $t = 0$ of $A(0) = 1$, $B(0) = 0$, and $\dot{A}(0) = \dot{B}(0) = 0$. Here, $A(t)$ and $B(t)$ are the fields in respective resonators in the rotating frame. (c) Eigenfrequencies (black lines) with $\omega_A/2\pi = 6$ GHz while sweeping $\omega_B/2\pi$. When $\omega_B = \omega_A$ the 'dressed' eigenfrequencies are split by $2g/2\pi$.

Next, we express the field in each oscillator in a frame rotating near their resonance frequencies $\omega'_A = \omega_A + g$ and $\omega'_B = \omega_B + g$ by making the transformations $a(t) = A(t)e^{-i\omega'_A t}$ and $b(t) = B(t)e^{-i\omega'_B t}$. We also define the detuning $\Delta = \omega_A - \omega_B$. Doing so and removing the fast-rotating terms (i.e. assuming $\omega'_A \gg \Delta$ and $\omega'_B \gg \Delta$), gives $\dot{A} = -\frac{\kappa_A}{2}A + ige^{i\Delta t}B$ and $\dot{B} = -\frac{\kappa_B}{2}B + ige^{-i\Delta t}A$, along with their complex conjugates. Here, $A(t)$ and $B(t)$ are phasors corresponding to the fields in the 'A' and 'B' oscillators in their respective rotating frames. We are often interested in the 'degenerate' case where $\Delta = 0$ in which these equations simplify to

$$\dot{A} = -\frac{\kappa_A}{2}A + igB, \tag{2.27}$$

$$\dot{B} = -\frac{\kappa_B}{2}B + igA, \tag{2.28}$$

and their complex conjugates. Solutions to Eqs. 2.27 and 2.28 are plotted in Fig. 2.4b. In this case,

energy swaps back and forth between the oscillators with a swap time of $\pi/2g$.

The Hamiltonian describing the circuit in Fig. 2.4a is the sum of the energy in either oscillator, plus the energy stored in the coupling inductor:

$$H = \hbar\omega'_A A^\dagger A + \hbar\omega'_B B^\dagger B + \hbar g\left(A^\dagger B + AB^\dagger\right), \tag{2.29}$$

where fast-rotating terms e.g. AB and $A^\dagger B^\dagger$ are neglected. The final term on the right-hand side of Eq. 2.29 is called the *beamsplitter* Hamiltonian.

It can be useful to consider the eigenfrequencies of Eqs. 2.25 and 2.26, plotted in Fig. 2.4c. For the degenerate case of $\omega_0 = \omega_A = \omega_B$, these eigenfrequencies are $\omega_0 + g \pm g$. Physically, these two eigenfrequencies correspond to symmetric and anti-symmetric modes. In the symmetric mode, no current flows across the coupling inductor and the fields in both resonators oscillate in phase at the 'decoupled' resonance frequency ω_0. In the antisymmetric mode, the fields in both resonators oscillate out of phase at the higher frequency $\omega_0 + 2g$.

2.1.6.1 Dispersive limit

We often consider the case where the oscillators are far detuned such that $g/\Delta \ll 1$. First, consider the lossless case such that $\kappa_A = \kappa_B = 0$. The eigenfrequencies λ_A and λ_B are then

$$\lambda_A = \omega'_A - \frac{g^2}{\Delta}, \tag{2.30}$$

$$\lambda_B = \omega'_B + \frac{g^2}{\Delta}, \tag{2.31}$$

plus higher order corrections. The 'bare' eigenfrequencies ω'_A and ω'_B of either resonator are changed by the *dispersive shift* equal to $\pm g^2/\Delta$.

In many systems, one resonator is much lossier than the other. We now take $\kappa_A = 0$ and $\kappa_B = \kappa$ to be nonzero, but in the limit where $\kappa/\Delta \ll 1$. The now complex eigenvalues of the system are:

$$\lambda_A = \omega'_A - \frac{g^2}{\Delta} - \frac{i\kappa g^2}{2\Delta^2}, \tag{2.32}$$

$$\lambda_B = \omega'_B + \frac{g^2}{\Delta} - \frac{i\kappa}{2}\left(1 - \frac{g^2}{\Delta^2}\right), \tag{2.33}$$

plus higher order corrections. Resonator 'A' therefore inherits an energy decay rate of $\kappa g^2/\Delta^2$ due to its dispersive coupling to the lossy resonator 'B'.

2.1.7 Parametrically coupled oscillators

We now consider a time-dependent modulation of the coupling inductor such that: $l_g(t) = l_0/\left(1+\epsilon\cos\left(\Omega t+\theta\right)\right)$ as in Eq. 2.10. This results in the time-dependent parametric coupling $g_p(t) = z_0/2l_g(t)$, or

$$g_p(t) = g + 2\nu\cos\left(\Omega t+\theta\right), \tag{2.34}$$

where $g = z_0/2l_0$ is the time-*independent* coupling of the previous section and $\nu = z_0\epsilon/4l_0$ is a new time-*dependent* coupling. For the remainder of this section we set $\theta = 0$.

Eqs. 2.25 and 2.26 are now modified such that the static coupling g of the previous section is replaced by the dynamic coupling $g_p(t)$ is given by Eq. 2.34. We make this substitution and transform to frames rotating at the respective resonant frequencies of the cavities such that $a(t) = A(t)e^{-i(\omega_A+2g)t}$ and $b(t) = B(t)e^{-i(\omega_B+2g)t}$. Neglecting the fast-oscillating terms yields the following equations of motion when modulating at the difference frequency between the resonators:

$$\left.\begin{aligned}\dot{A} &= -\frac{\kappa_A}{2}A + i\nu B\\ \dot{B} &= -\frac{\kappa_B}{2}B + i\nu A\end{aligned}\right\}\ \Omega = \Delta \tag{2.35}$$

and their complex conjugates. Related equations of motion are obtained when modulating at the sum frequency:

$$\left.\begin{aligned}\dot{A} &= -\frac{\kappa_A}{2}A + i\nu B^\dagger\\ \dot{B} &= -\frac{\kappa_B}{2}B + i\nu A^\dagger\end{aligned}\right\}\ \Omega = 2\omega_0 \tag{2.36}$$

and their complex conjugates. Modulating the coupling between two resonators at their difference frequency, as in Eq. 2.35, turns on a coupling between the two resonators, just like the system described by Eqs. 2.27 and 2.28. Now, however, the cavity bare resonant frequencies can be detuned by an arbitrary amount much greater than their bare coupling rate g. Modulation at the sum frequency, as in Eq. 2.36, turns on parametric gain.

Notice that the strength of the parametric interaction $\nu = g\epsilon/2$ is a function of the bare coupling g and the parametric modulation amplitude ϵ. Many physical systems are described by the limit where $|\epsilon| \ll 1$, so that the strength of parametric interaction is weak compared to the degenerate case (Eq. 2.27 and Eq. 2.28).

2.2 Quantum oscillators

2.2.1 Quantization of the electromagnetic field

In Sec. 2.1 the flux Φ and charge q, or likewise the fields a and $a^\dagger$, are scalar values which commute and can simultaneously be zero [82, 86, 87]. In a quantum picture this is not true. Instead, these variables are replaced by analogous *operators* $\hat{\Phi}$, $\hat{q}$ and $\hat{a}$, $\hat{a}^\dagger$ which obey the commutation relations [81],

$$\left[\hat{\Phi}, \hat{q}\right] = i\hbar, \qquad \left[\hat{a}, \hat{a}^\dagger\right] = 1, \tag{2.37}$$

where $\hat{a}$ and $\hat{a}^\dagger$ are the creation and annihilation operators. Note that Eq. 2.2 still describes the normal mode transformation between these variables, such that $\hat{a} = \frac{1}{\sqrt{2\hbar}}\left(\hat{\Phi}/\sqrt{z_0} + i\sqrt{z_0}\hat{q}\right)$, where z_0 is the characteristic impedance of the resonator.

2.2.2 A quantum simple harmonic oscillator

The quantum mechanical Hamiltonian for a simple harmonic oscillator, e.g. Fig. 2.1a, is

$$\hat{H} = \hbar\omega_0\left(\hat{a}^\dagger\hat{a} + \frac{1}{2}\right). \tag{2.38}$$

Note the similarity between Eq. 2.38 and Eq. 2.4. In the quantum description, the fields are replaced by operators and there is an extra 'zero-point energy' $\hbar\omega_0/2$.

A quantum simple harmonic oscillator has the eigenstates $|n\rangle$ such that $\hat{H}|n\rangle = E_n|n\rangle$, where $n = 0, 1, 2$, etc.. Here, the energy eigenvalues $E_n = \hbar\omega_0(n + 1/2)$ of the harmonic oscillator form a ladder of levels equally spaced by $\hbar\omega_0$. The creation and annihilation operators and the number operator $\hat{n} = \hat{a}^\dagger\hat{a}$ act on the eigenstates $|n\rangle$ by

$$\hat{a}|n\rangle = \sqrt{n}\,|n-1\rangle, \qquad \hat{a}^\dagger|n\rangle = \sqrt{n+1}\,|n+1\rangle, \qquad \hat{n}|n\rangle = n|n\rangle, \tag{2.39}$$

with $\hat{a}\,|0\rangle = 0$.

The quantum state of the harmonic oscillator can in general be in a superposition of number eigenstates, such that $|\psi\rangle = \sum_{n=0}^{\infty} c_n\,|n\rangle$, where $|c_n|^2$ gives the probability of the oscillator being in number state $|n\rangle$ when measured. States are normalized such that $\sum_{n=0}^{\infty} |c_n|^2 = 1$.

2.2.3 Coherent states

2.2.3.1 Representation in the number basis

Of special importance are coherent states, denoted $|\alpha\rangle$ [82, 86, 87]. Coherent states are eigenstates of the annihilation operator such that $\hat{a}\,|\alpha\rangle = \alpha\,|\alpha\rangle$. From this property,

$$|\alpha\rangle = \sum_{n=0}^{\infty} \frac{\alpha^n}{\sqrt{n!}} e^{-|\alpha|^2/2}\,|n\rangle\,, \tag{2.40}$$

where α is a complex number specifying the amplitude and phase of the coherent state. The probability that a coherent state will be measured in a particular eigenstate $|n\rangle$ follows a Poisson distribution with a mean of $|\alpha|^2$ (the mean photon number). This probability distribution $|\langle n|\alpha\rangle|^2 = |\alpha|^{2n}\,e^{-2|\alpha|^2}/n!$ is plotted in Fig. 2.5a for three different photon numbers. Notice that $\alpha = 0$ corresponds to the oscillator being in state $|n = 0\rangle$ with unit probability. This special coherent state is called the *vacuum* state.

2.2.3.2 Representation in the quadrature basis

It is often useful to describe the state of a simple harmonic oscillator in the quadrature basis, rather than the number basis. Unlike the *discrete* number basis which is defined by eigenstates of the number operator $\hat{n} = \hat{a}^\dagger\hat{a}$, the quadrature basis is a *continuous* basis defined by two orthogonal quadrature operators,[6]

$$\hat{x} = \frac{1}{2}\left(\hat{a} + \hat{a}^\dagger\right), \qquad \hat{y} = \frac{1}{2i}\left(\hat{a} - \hat{a}^\dagger\right). \tag{2.41}$$

[6] Note there are different conventions for how to define the quadrature operators. We follow the conventions of Loudon [86] and Gerry & Knight [87], but Walls & Milburn [82] take $\hat{x} = \hat{a} + \hat{a}^\dagger$ and $\hat{y} = \left(\hat{a} - \hat{a}^\dagger\right)/i$, yielding a different uncertainty relation in Eq. 2.42, etc.

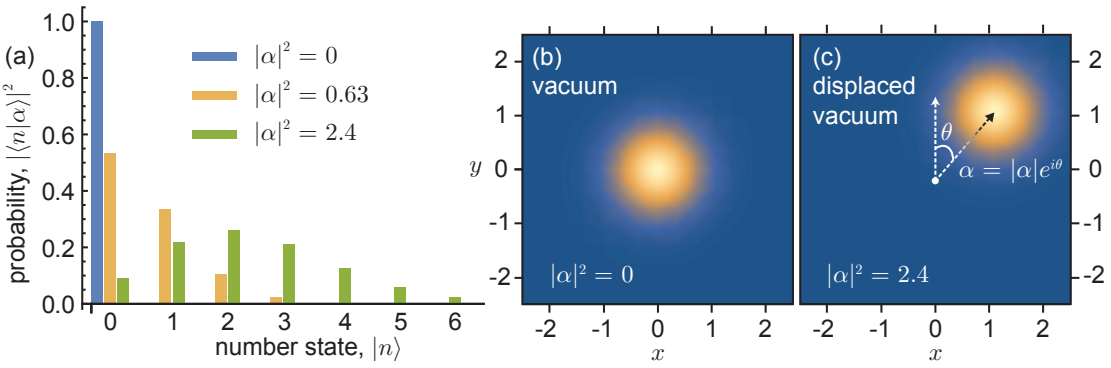

Figure 2.5: **Coherent states**. (a) Number state probability distribution for three different coherent states of mean photon number $|\alpha|^2$. The state with $|\alpha|^2 = 0$ is the *vacuum* state. (b,c) Quasiprobability distribution (the Wigner function, Eq. 2.44) of a coherent state with $|\alpha|^2 = 0$, and $|\alpha|^2 = 2.4$ at angle $\theta = \pi/4$, respectively. The complex number $\alpha = |\alpha|e^{i\theta}$, illustrated by the arrow in (c), displaces the vacuum state from the origin to create the coherent state $|\alpha\rangle$. Note that here, θ is defined so that $\theta = 0$ corresponds to a state pointing along the y-quadrature, and $\theta = \pi/2$ corresponds to a state pointing along the x-quadrature.

These operators are analogous to the charge and flux operators in dimensionless units, and have eigenstates $|x\rangle$ and $|y\rangle$ respectively such that $\hat{x}\,|x\rangle = x\,|x\rangle$ and $\hat{y}\,|y\rangle = y\,|y\rangle$. They have the non-zero commutation relation $[\hat{x}, \hat{y}] = i/2$, yielding the uncertainty relation,

$$(\Delta x)^2\,(\Delta y)^2 \geq \left(\frac{1}{4}\right)^2. \tag{2.42}$$

Here, $(\Delta x)^2$ is a variance (i.e. the square of a standard deviation Δx) associated with an uncertainty along the x-quadrature such that $(\Delta x)^2 = \langle x^2\rangle - \langle x\rangle^2$. Eq. 2.42 implies that even in its lowest energy eigenstate, the 'vacuum fluctuations' of the field in an oscillator are not zero, seen already by the zero-point energy $\hbar\omega_0/2$ in Eq. 2.38. For a coherent state, the fluctuations along each quadrature are equal such that $\Delta x = \Delta y = 1/2$.

To express a coherent state in the quadrature basis, we make use of the displacement operator $\hat{D}(\alpha)$. Coherent states can also be defined as the displacement operator acting on the vacuum state such that

$$\hat{D}\,(\alpha) = e^{\alpha\hat{a}^\dagger - \alpha^*\hat{a}}, \qquad |\alpha\rangle = \hat{D}(\alpha)\,|0\rangle\,. \tag{2.43}$$

Notice that when $|\alpha| = 0$ the displacement operator is the identity matrix, and so the oscillator

remains in the vacuum state.

A quantum state may be graphically represented in phase space by one of several quasiprobability distributions. Commonly used is the Wigner function, defined as [82, 86, 87]:

$$W(x,y) = \frac{1}{\pi\hbar}\int_{-\infty}^{\infty} dx' \left\langle x + \frac{x'}{2}\right| \hat{\rho} \left| x - \frac{x'}{2}\right\rangle e^{ix'y/\hbar}, \tag{2.44}$$

where $\hat{\rho} = |\alpha\rangle\langle\alpha|$ for a coherent state, which in Eq. 2.44 is represented in the quadrature basis, with x, y and x' real variables. The Wigner function of a vacuum state $|0\rangle$ with photon number $|\alpha|^2 = 0$ is a Gaussian centered at the origin, Fig. 2.5b, and a non-zero α translates this Gaussian, Fig. 2.5c. The meaning of the displacement operator thus becomes clear: coherent states are vacuum states translated from the origin to a mean position in phase space specified by the complex number α.

To determine the 'wavefunction' of a coherent state along the x-quadrature, we take the inner product $\langle x|\alpha\rangle = \langle x|\,\hat{D}(\alpha)\,|0\rangle$ with $\alpha = |\alpha|e^{i\theta}$, defining the angle θ such that $\theta = 0$ corresponds to a state pointing along the y-quadrature, Fig. 2.5c.[7] Doing this computation and an analogous one for the y-quadrature yields

$$\langle x|\alpha\rangle = (2/\pi)^{1/4}\, e^{-i|\alpha|^2\sin(2\theta)/2} e^{-\left[(x-|\alpha|\sin\theta)^2 - 2ix|\alpha|\cos\theta\right]}, \tag{2.45}$$

$$\langle y|\alpha\rangle = (2/\pi)^{1/4}\, e^{-i|\alpha|^2\cos(2\theta)/2} e^{-\left[(y-|\alpha|\cos\theta)^2 - 2iy|\alpha|\sin\theta\right]}. \tag{2.46}$$

Given an ideal homodyne detector, the probability of measuring a coherent state to have quadrature value x or y, respectively, is given by

$$|\langle x|\alpha\rangle|^2 = \sqrt{2/\pi} e^{-2(x-|\alpha|\sin\theta)^2}, \tag{2.47}$$

$$|\langle y|\alpha\rangle|^2 = \sqrt{2/\pi} e^{-2(y-|\alpha|\cos\theta)^2}. \tag{2.48}$$

Here, Eq. 2.47 and Eq. 2.48 are normalized such that $\int_{-\infty}^{\infty} dx\,|\langle x|\alpha\rangle|^2 = \int_{-\infty}^{\infty} dy\,|\langle y|\alpha\rangle|^2 = 1$, and are related to the Wigner function by $\int_{-\infty}^{\infty} dy\, W(x,y) = |\langle x|\alpha\rangle|^2$ and $\int_{-\infty}^{\infty} dx\, W(x,y) = |\langle y|\alpha\rangle|^2$.

Notice that both Eq. 2.45 and Eq. 2.46 are Gaussians with the single-quadrature standard deviation of $1/\sqrt{2}$ and the single-quadrature variance of $1/2$. Eq. 2.47 and Eq. 2.48 are *also*

[7] This unconventional choice of angle is so that in Chp. 3, we measure along the *conventional* choice of the x-quadrature.

Gaussians with the single-quadrature standard deviation of $1/2$ and the single-quadrature variance of $1/4$ as previously stated in Eq. 2.42. The classical limit emerges when $|\alpha|^2 \gg 0$, so that the photon number is much greater than the variance of $1/4$. Neglecting these quantum fluctuations, the coherent state is analogous to the phasor 'A' in Sec. 2.1, which is a point in phase space.

2.2.3.3 Two coherent states

Two coherent states $|\alpha_0\rangle$ and $|\alpha_1\rangle$ are not in general orthogonal: their inner product $\langle\alpha_0|\alpha_1\rangle \neq 0$ for finite values of α_0 and α_1. However, two coherent states can be 'more' or 'less' orthogonal dependent on the difference in phase space between α_0 and α_1. The inner product between two coherent states is straightforwardly computed by using the displacement operator in Eq. 2.43: $\langle\alpha_0|\alpha_1\rangle = \langle 0|\,\hat{D}^\dagger(\alpha_0)\,\hat{D}(\alpha_1)\,|0\rangle = e^{-\frac{1}{2}\left(|\alpha_0|^2 - 2\alpha_0^*\alpha_1 + |\alpha_1|^2\right)}$. Let us consider the specific case of two coherent states with the same amplitude but different phase, so that $\alpha_0 = |\alpha|e^{i\theta}$ and $\alpha_1 = \alpha_0^* = |\alpha|e^{-i\theta}$. We compute

$$|\langle\alpha_0|\alpha_1\rangle| = e^{-2|\alpha|^2\sin^2\theta}, \tag{2.49}$$

where $|\alpha|\sin\theta = \mathrm{Re}[\alpha]$ is the projection of the phasor α along the x-quadrature, equal to the angle θ as defined in Figs. 2.5b,c. From Eq. 2.49, we can see that the inner product of these two coherent states goes to zero in the limit of $|\alpha| \to \infty$ as long as they are at different angles in phase space such that $\sin\theta \neq 0$. The inner product between any two *identical* coherent states, including the inner product between the vacuum state and itself, is equal to 1.

2.2.4 Qubits

2.2.4.1 Introduction to qubits

Unlike the infinite dimensional Hilbert space of a harmonic oscillator, a qubit is described by a two dimensional Hilbert space with eigenstates $|0\rangle$ and $|1\rangle$ only. Unlike a classical bit which can have value 0 or 1 only, a qubit can be in a *superposition* state, for example $|\psi\rangle = (|0\rangle + |1\rangle)/\sqrt{2}$

with the density matrix $\hat{\rho} = |\psi\rangle\langle\psi|$. More explicitly,

$$|\psi\rangle = c_0|0\rangle + c_1|1\rangle, \qquad \hat{\rho} = \begin{pmatrix} c_0^* c_0 & c_0 c_1^* \\ c_0^* c_1 & c_1^* c_1 \end{pmatrix}, \tag{2.50}$$

where c_0 and c_1 are complex valued coefficients with the property $\mathrm{Tr}(\hat{\rho}) = |c_0|^2 + |c_1|^2 = 1$.

The state of a qubit can be visualized using the Bloch sphere, Fig. 2.6a. A qubit's density matrix corresponds to a vector pointing from the origin to any position on the surface or interior of the sphere. Points on the surface of the sphere are called *pure* states which have the property $\hat{\rho} = \hat{\rho}^2$. Any state with a nonzero component along the x or y-axes of the Bloch sphere describes a qubit in a superposition — a situation not allowed classically. States on the interior of the sphere are *mixed* states corresponding to a probabilistic distribution of different pure states. State's falling along the z-axis of the Bloch sphere are 'classical' in that they correspond to the qubit being either in the $|0\rangle$ or $|1\rangle$ state with some probability, equivalent to describing a weighted coin. For example, the point at the center of the sphere is the maximally mixed state meaning that the qubit is *either* in state $|0\rangle$ or $|1\rangle$ with equal probability — but not in any superposition between them. Some important qubit states are summarized in Table. 2.2.4.1.

Table 2.1: **Important qubit states.** Manipulations of a qubit's state can be deconstructed in terms of the Pauli operators: $\hat{\sigma}_x$, $\hat{\sigma}_y$ and $\hat{\sigma}_z$. Also useful are the qubit lowering operator $\hat{\sigma}_- = |0\rangle\langle 1|$ and raising operator $\hat{\sigma}_+ = |1\rangle\langle 0|$.

Name	Bra-ket notation	Density matrix, $\hat{\rho}$	Pure/mixed?
Ground	$\|0\rangle$	$\begin{pmatrix} 1 & 0 \\ 0 & 0 \end{pmatrix}$	pure
Excited	$\|1\rangle$	$\begin{pmatrix} 0 & 0 \\ 0 & 1 \end{pmatrix}$	pure
Maximally mixed	$\frac{1}{2}\|0\rangle\langle 0\| + \frac{1}{2}\|1\rangle\langle 1\|$	$\frac{1}{2}\begin{pmatrix} 1 & 0 \\ 0 & 1 \end{pmatrix}$	mixed
Superposition	$\frac{1}{\sqrt{2}}(\|0\rangle + \|1\rangle)$	$\frac{1}{2}\begin{pmatrix} 1 & 1 \\ 1 & 1 \end{pmatrix}$	pure

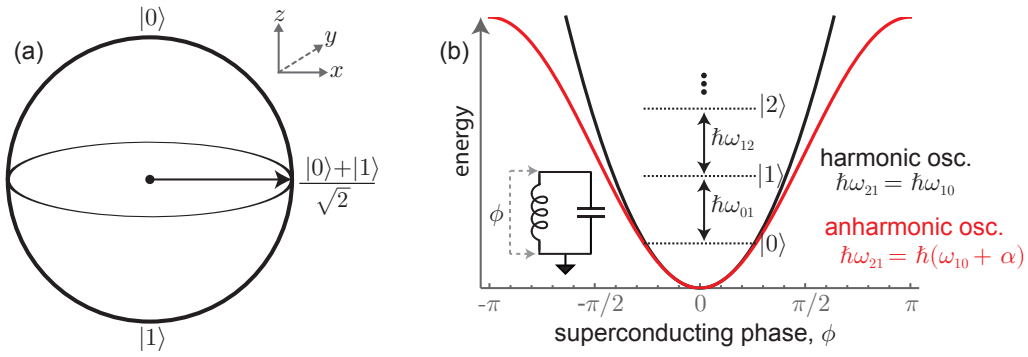

Figure 2.6: **A qubit from an anharmonic resonator**. (a) The quantum state of a qubit can be represented on the Bloch sphere, for example the ground state $|0\rangle$, the excited state $|1\rangle$, or the particular superposition state $(|0\rangle + |1\rangle)/\sqrt{2}$. The density matrix $\hat{\rho}$ can be represented as a vector pointing from the origin to any point on or within the sphere. (b) The eigenstates of a *harmonic* oscillator are an evenly spaced ladder of energy levels, here plotted overlaid onto a quadratic energy potential vs. the superconducting phase ϕ across an inductor. Adding nonlinearity to the resonator can modify this potential, changing the spacing between energy levels such that $\omega_{21} = \omega_{10} + \alpha$, where here α is the anharmonicity, which is typically negative with $0.01 \lesssim |\alpha/\omega_0| \lesssim 0.1$ for superconducting qubits. (Note the variable α, here referring to anharmonicity, is distinct from the same notation used in the discussion of coherent states in Sec. 2.2.3.) The lowest two levels are taken as a qubit with frequency $\omega_q = \omega_{10}$. (Subplot (b) is inspired by diagrams in Refs. [81, 88].)

2.2.4.2 Superconducting qubits from anharmonic resonators

In superconducting systems, qubits are commonly created by using an *anharmonic* LC-oscillator [88, 13].[8] Recall that the eigenstates of the simple harmonic oscillator (Eq. 2.38) are a 'ladder' of equally spaced energy levels. 'Anharmonic' means that the spacings between these energy levels are made to be unequal such that $\omega_{21} - \omega_{10} = \alpha$,[9] where the anharmonicity $\alpha \neq 0$ is typically negative for superconducting qubits [18]. The lowest two of these energy levels are taken as the ground and excited state of the qubit. Because the spacing between these levels is now unique, the qubit can be controlled by driving at this specific frequency difference $\omega_q = \omega_{10}$. The

[8] The single-photon-level nonlinearity required to achieve this anharmonicity is provided by a *Josephson junction*. A Josephson junction is a non-superconducting link between two superconducting leads and functions as a nonlinear inductor. Its energy is a cosinusoidal function of branch flux across it, rather than quadratic as for a linear inductor. More information about Josephson junctions is provided in Appx. A.

[9] Note the symbol α is used *separately* for both the anharmonicity and coherent state amplitude.

qubit's Hamiltonian is $\hat{H} = \hbar\omega_q\hat{\sigma}_+\hat{\sigma}_-$ which is often shifted to

$$\hat{H} = \frac{1}{2}\hbar\omega_q\hat{\sigma}_z. \tag{2.51}$$

Note that a qubit prepared in a superposition state will precess around the equator of the Bloch sphere at frequency ω_q. It is typical to work in a frame rotating at this frequency.

There are many different types of superconducting qubits. The 'transmon' qubit typically has $-\alpha$ of several hundred MHz compared to a resonator frequency of $\omega_q/2\pi$ typically between 5 and 10 GHz. Note that the 'transmon' regime is defined by the ratio of Josephson energy E_J (energy stored in the Josephson junction) to charging energy E_C (energy stored in the capacitor) such that $E_J/E_C \approx 20-80$. This ends up being a favorable tradeoff between reducing charge noise on the capacitor while preserving anharmonicity [18, 89].

2.2.4.3 Qubit-cavity systems

Superconducting qubits are often coupled to linear cavities [15]. These cavities help keep the qubit well isolated from the environment and are also used for qubit measurement (see Chp. 3). This qubit-cavity system is described by the Jaynes-Cummings Hamiltonian [90]:

$$\hat{H} = \hbar\omega_0\hat{a}^\dagger\hat{a} + \frac{1}{2}\hbar\omega_q\hat{\sigma}_z + \hbar g\left(\hat{a}^\dagger\hat{\sigma}_- + \hat{a}\hat{\sigma}_+\right). \tag{2.52}$$

The first term of Eq. 2.52 desribes a linear cavity with the zero-point energy neglected and the second term describes the qubit. The third term describes excitations being exchanged between the cavity and the qubit, parameterized by a coupling rate g. Note that the Jaynes-Cummings model is within the rotating-wave approximation and ignores any dissipative processes.

Superconducting systems are often engineered in the *dispersive* limit of the Jaynes-Cummings model [15, 13], meaning $|g/\Delta| \ll 1$ where $\Delta = \omega_0 - \omega_q$ is the detuning between the cavity and qubit. In this limit Eq. 2.52 simplifies to

$$\hat{H} = \hbar\omega_0'\hat{a}^\dagger\hat{a} + \frac{1}{2}\hbar\omega_q'\hat{\sigma}_z + \hbar\chi\hat{a}^\dagger\hat{a}\hat{\sigma}_z. \tag{2.53}$$

Here, $\omega_0' = \omega_0 + g^2/(\Delta + \alpha)$ and $\omega_q' = \omega_q - g^2/\Delta$ are the shifted frequencies of the resonator and qubit, respectively [18, 13], like the shifts of the eigenfrequencies of two dispersively coupled linear cavities derived in Eqs. 2.30 and 2.31. The dispersive-shift χ is the change in the readout cavity frequency dependent on if the qubit is in the ground or excited state. In the transmon regime this is [88]:

$$\chi = \left(\frac{g^2}{\Delta}\right)\frac{\alpha}{\Delta + \alpha}. \tag{2.54}$$

2.3 Input-output theory

This section reviews input-output theory which describes the coupling between an oscillator and an external environment. This treatment can be either classical or quantum [91, 92, 82, 93], but the classical description is given here.

2.3.1 A one-port cavity

We first consider the case of a cavity with a single port, e.g. Fig. 2.1c. The port is parameterized by a coupling rate κ_1, along with some internal loss κ_{int} such that the cavity has a total energy decay rate of $\kappa = \kappa_1 + \kappa_{\text{int}}$. Input-output theory [91] solves the Heisenberg equation of motion for this system including the incoming and outgoing fields $a_{\text{in},1}(t)$ and $a_{\text{out},1}(t)$, respectively, in addition to the field $a(t)$ inside the resonator. The equation of motion for this cavity is:

$$\dot{a} = -i\omega_0 a - \frac{\kappa}{2}a + \sqrt{\kappa_1}a_{\text{in},1}(t), \tag{2.55}$$

with the input-output relation:[10]

$$a_{\text{out},1} + a_{\text{in},1} = \sqrt{\kappa_1}a. \tag{2.56}$$

After taking the Fourier-transform of the input-output relations, the frequency-dependent reflection coefficient (the scattering parameter) $S_{11}(\omega) = a_{\text{out},1}/a_{\text{in},1}$ is given by

$$S_{11} = \frac{i\delta + \kappa_1/2 - \kappa_{\text{int}}/2}{-i\delta + \kappa/2}, \tag{2.57}$$

[10] It is a potential source of confusion that per convention, the field in the cavity a has different units from the incoming and outgoing fields a_{in} and a_{out}. This can be roughly understood as the incoming and outgoing fields are *propagating* so $|a_{\text{in}}|^2$ and $|a_{\text{out}}|^2$ describe a flux in units of photons/s. The field in the cavity is *not* propagating and so $|a|^2$ is expressed in units of photons.

where $\kappa = \kappa_1 + \kappa_{\text{int}}$ is the total loss rate (linewidth) of the cavity, and $\delta = \omega - \omega_0$ is the detuning from its resonance frequency ω_0.

Table 2.2: **Cavity coupling regimes.**

Name	Criteria	Reflection at $\delta = 0$	Phase wrap
Undercoupled	$\kappa_1 < \kappa - \kappa_1$	< 0	0
Critically coupled	$\kappa_1 = \kappa - \kappa_1$	0	π
Overcoupled	$\kappa_1 > \kappa - \kappa_1$	> 0	2π

Solutions to Eq. 2.57 fall into three categories dependent on the relationship between an external coupling rate κ_1 and the additional loss rate $\kappa - \kappa_1$. In the *under*coupled case, a port's coupling rate is smaller than other contributions to the cavity's loss, and the majority of incoming radiation is reflected without interacting with the cavity. In the *critically* coupled case, $\kappa_1 = \kappa - \kappa_1$ and on-resonance incoming radiation is entirely absorbed. Finally, in the *over*coupled case $\kappa_1 > \kappa - \kappa_1$, most on-resonance incoming radiation is also reflected but after interacting with the cavity, giving a different phase shift from the undercoupled case. These cases are summarized in Table 2.3.1.

2.3.2 A two-port cavity

Often we are interested in a cavity with *two* ports of coupling rates κ_1 and κ_2, Fig. 2.7a. This results in the term $\sqrt{\kappa_2}a_{\text{in},2}(t)$ being added to the right-hand sides of Eq. 2.55, and a second input-output relation analogous to Eq. 2.56 describing the field continuity at the second port.

After taking the Fourier-transform of these modified relations, the scattering parameters are $S_{11} = a_{\text{out},1}/a_{\text{in},1}$ and $S_{21} = a_{\text{out},2}/a_{\text{in},1}$ are given by

$$S_{11} = \frac{i\delta + \kappa_1/2 - \kappa_2/2 - \kappa_{\text{int}}/2}{-i\delta + \kappa/2}, \qquad S_{21} = \frac{\sqrt{\kappa_1\kappa_2}}{-i\delta + \kappa/2}, \tag{2.58}$$

where $\kappa = \kappa_1 + \kappa_2 + \kappa_{\text{int}}$. Solutions to S_{11} for the three cases in Table 2.3.1 are plotted in Fig. 2.7.

Such analysis can be extended to N-port cavities. In a cavity with N ports, $\kappa = \kappa_{\text{int}} + \Sigma_{i=1}^{N}\kappa_i$ and the subscripts 1 and 2 in Eq. 2.58 can be replaced by any desired choice of ports (e.g. S_{ij}

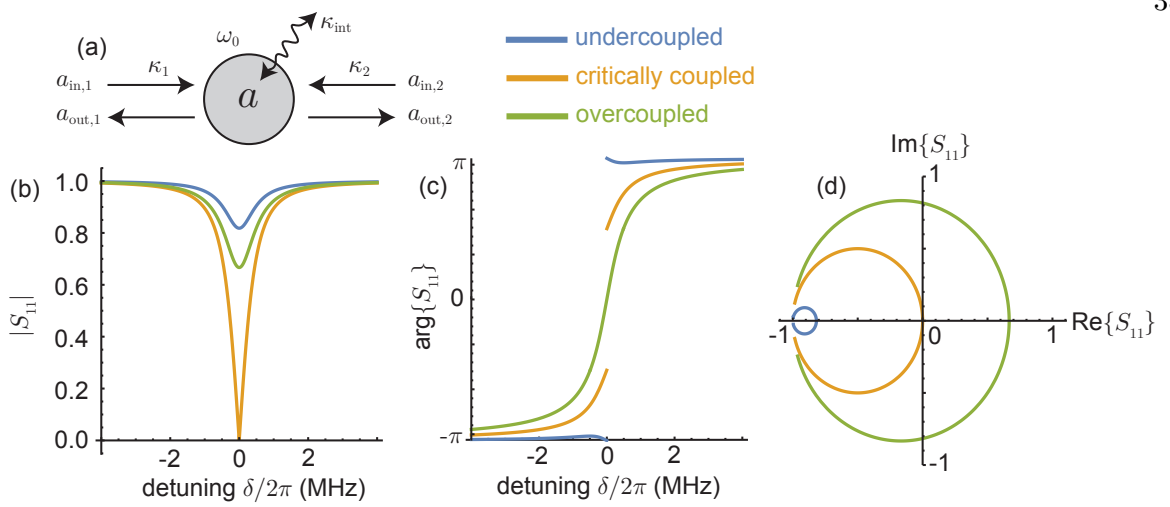

Figure 2.7: **Scattering parameters of a cavity**. (a) Input-output theory model for a 2-port cavity. The field a inside the cavity interacts with incoming and outgoing fields a_{in} and a_{out}, respectively, from either port. The cavity has a bare resonance frequency of ω_0, external coupling rates of κ_1 and κ_2, an internal loss rate κ_{int}, and a total loss rate $\kappa = \kappa_1 + \kappa_2 + \kappa_{\text{int}}$. Internal loss is equivalent to a 'fictitious' third port with coupling rate κ_{int}, whose outgoing field cannot be measured. (b-d) Reflection from port 1, Eq. 2.57, for three different parameter regimes. The frequency response is a Lorentzian function. Here the 'undercoupled' case takes $\kappa_1/2\pi = 0.1\,\text{MHz}$ and $\kappa_2/2\pi = 1\,\text{MHz}$, the 'critically coupled' case takes $\kappa_1/2\pi = 0.5\,\text{MHz}$ and $\kappa_2/2\pi = 0.5\,\text{MHz}$, and the 'overcoupled' case takes $\kappa_1/2\pi = 1.0\,\text{MHz}$ and $\kappa_2/2\pi = 0.2\,\text{MHz}$. All cases take $\kappa_{\text{int}} = 0$. (b) Absolute value of reflection. (c) Phase of reflection. (d) Representation in the complex plane.

where $i \in \{1, 2, ...N\}$ and $j \in \{1, 2, ...N\}$), but the form of Eq. 2.58 otherwise remains the same.

2.4 Summary

This chapter introduces some important examples which are generally relevant to the field of superconducting circuits and the work presented later in this thesis. In a 'classical' description, the state of an oscillator is specified by the scalar fields a and $a^\dagger$ which commute, and specify a single point in phase space. In a 'quantum' description, the oscillator is instead described by operators $\hat{a}$ and $\hat{a}^\dagger$ which do not commute, leading to an uncertainty relation and the state of the oscillator being a 'blob' in phase space.

In the number basis, the energy eigenstates of simple harmonic oscillator form a ladder of equally-spaced eigenstates ('rungs' on the ladder). Nonlinearity added to the resonator can

Table 2.3: **Summary of different oscillators**. Hamiltonians are listed in a quantum description where $\hat{a}$ and $\hat{a}^\dagger$, etc. are operators with the commutation relation $\left[\hat{a}, \hat{a}^\dagger\right] = 1$, and zero-point energy is neglected. In a classical description, operators are replaced by scalar fields. Resonance frequencies are re-parameterized such that $\omega_A' \to \omega_A$, $\omega_B' \to \omega_B$, $\omega_0' \to \omega_0$ and $\omega_q' \to \omega_q$ in the Hamiltonians listed here, which are written in the rotating-wave-approximation when appropriate.

Name	Section	Hamiltonian	Physical example
harmonic oscillator	2.1.1, 2.1.2, 2.2.2	$\hbar\omega_0\hat{a}^\dagger\hat{a}$	superconducting microwave cavity [94]
parametric oscillator	2.1.4	$\hbar\omega_0\hat{a}^\dagger\hat{a} + \frac{1}{2}\hbar\left(\xi\hat{a}^2 + \xi^*\hat{a}^{\dagger 2}\right)$	'flux-pumped' JPA [29, 95]
nonlinear oscillator	2.1.5	$\hbar\omega_0\hat{a}^\dagger\hat{a} - \frac{1}{2}\hbar\zeta\left(\hat{a}^\dagger\hat{a}\right)^2$	JPA ($\zeta \ll \kappa$) [28],[a] qubit ($\zeta \gg \kappa$) [15]
coupled oscillators	2.1.6	$\hbar\omega_A\hat{a}^\dagger\hat{a} + \hbar\omega_B\hat{b}^\dagger\hat{b} + \left(g\hat{a}^\dagger\hat{b} + g^*\hat{a}\hat{b}^\dagger\right)$	SIMBA + readout cavity [23]
qubit	2.2.4.1	$\frac{1}{2}\hbar\omega_q\hat{\sigma}_z$	transmon [18, 89]
Jaynes-Cummings model, dispersive limit	2.2.4.3	$\hbar\omega_0\hat{a}^\dagger\hat{a} + \frac{1}{2}\hbar\omega_q\hat{\sigma}_z + \hbar\chi\hat{a}^\dagger\hat{a}\hat{\sigma}_z$	qubit + readout cavity [14, 97]

[a] A Josephson parametric amplifier (JPA) is a nonlinear cavity where the Kerr-constant ζ (frequency-shift per photon) is typically much smaller than the linewidth κ, see Chp. 4. The JPA can generally be treated in the classical limit; note that its amplified state can contain hundreds of photons, far larger than vacuum fluctuations. A superconducting qubit (e.g. a transmon) is also an example of a nonlinear oscillator, but where ζ is generally much larger, so that the oscillator has a nonlinear response for even a single excitation and must be treated with a quantum description. See Ref. [96] for analysis of the transition between these limits.

shift the spacing of these eigenstates so that a qubit can be formed from the lowest two of these eigenstates. In superconducting qubits, this nonlinearity is provided by the Josephson junction, which is nonlinear even at the single-photon level. In practice, superconducting qubits are often dispersively coupled to a readout resonator, realizing the Jaynes-Cummings Hamiltonian in the dispersive limit.

To measure a resonator, a 'port' is introduced to couple the field in the cavity to an external environment. This coupling is described using the formalism of input-output theory. The frequency

dependent response of a signal scattered from this port can then be used to measure parameters of the cavity.

Not discussed in this chapter are systems of *many* oscillators, the effects of non-zero temperature, the fluctuation-dissipation theorem, squeezed light, and many other important examples from quantum optics. Further information and more detailed discussion can be found in textbooks [82, 86, 87, 93] or review articles [24, 81, 88, 98].

Chapter 3

Qubit measurement

3.1 Formalism of quantum measurement

Qubits are the basic unit of quantum information, analogous to bits in classical computing. Measuring the state of a qubit in a 'high-quality' way is essential to any quantum computing protocol on any hardware platform. In this chapter, we precisely define qubit measurement and several important metrics describing its performance. We then show how these metrics can be quantified.

3.1.1 Difference from classical measurement

First, we briefly acknowledge the fundamental difference between classical and quantum measurement. A classical bit is in *either* the 0 or 1 state, both before and after any measurement. A qubit prepared in the state $(|0\rangle + |1\rangle)/\sqrt{2}$ is in a superposition state of 'both' $|0\rangle$ and $|1\rangle$ at the same time (the 'superposition state' in Table. 2.2.4.1). This is Schrödinger's cat being alive *and* dead, if you like, and is fundamentally different than the qubit being in either $|0\rangle$ *or* $|1\rangle$ (e.g. the 'maximally mixed' in Table. 2.2.4.1). When a qubit prepared in a superposition state is projectively measured, its state is collapsed onto either the $|0\rangle$ or $|1\rangle$ eigenstate — equivalent to 'looking' at Schrödinger's cat and finding it either alive *or* dead.

What exactly this 'quantum superposition' means has been, and will continue to be, the subject of a great deal of debate within the context of the philosophy of physics. Quantum superposition troubled Einstein [99], who famously objected to it saying *"God does not play dice*

with the universe." Going forward, we will ignore such debates and take measurement to be an axiom of quantum theory, per the modern viewpoint described in John Preskill's notes on quantum information [100].

3.1.2 POVMs and Kraus operators

Recall that a quantum state is fully described its density matrix $\hat{\rho} = |\psi\rangle\langle\psi|$.[1] A quantum measurement on this state is characterized by a positive operator-valued measure (POVM) $\Pi = \{\Pi_x \colon x \in \mathcal{X}\}$, which consists of a set of positive semidefinite operators $\Pi_x \geq 0$ labeled by the measurement outcome x in some set $\mathcal{X}$, and satisfying $\sum_{x\in\mathcal{X}} \Pi_x = \mathbb{I}$. For each x one may choose Kraus operators A_x such that $\Pi_x = A_x^\dagger A_x$. Note that the choice of Kraus operators is not unique. Given a measurement outcome x, the POVM maps a quantum state $\hat{\rho}$ to a new quantum state $\hat{\rho}'_x$ via the formula [101]

$$\hat{\rho}'_x = \frac{A_x \hat{\rho} A_x^\dagger}{\mathrm{Tr}\,(\Pi_x \hat{\rho})}. \tag{3.1}$$

Since the POVM is complete, $\sum_{x\in\mathcal{X}} \Pi_x = \mathbb{I}$, the post-measurement state is then

$$\hat{\rho}' = \sum_x \lambda_x \hat{\rho}'_x, \tag{3.2}$$

with probabilities $\lambda_x = \mathrm{Tr}\,(\Pi_x \hat{\rho})$.

In other words, measurement of a quantum state $\hat{\rho}$ returns a set of possible outcomes indexed by the measurement outcome x. Each measurement outcome (each different x) maps the initial density matrix $\hat{\rho}$ to a new density matrix $\hat{\rho}'_x$, Eq. 3.1. This mapping is specified by the Kraus operators $A_x^\dagger$ and A_x (or the related POVM $\Pi_x = A_x^\dagger A_x$), where each possible measurement value x corresponds to a separate Kraus operator and POVM. The quantum state's post-measurement density matrix $\hat{\rho}'$, Eq. 3.2, is the mixed state which is the ensemble of density matrices corresponding to all possible measurement outcomes $\hat{\rho}'_x$, weighted by the probabilities λ_x of obtaining each measurement.

[1] See Sec. 2.2.2 for more information.

For example, consider a pre-measurement pure state $c_0 |0\rangle + c_1 |1\rangle$. After a projective measurement, this state will 'collapse' to either $|0\rangle$ with probability $|c_0|^2$ or $|1\rangle$ with probability $|c_1|^2 = 1 - |c_0|^2$. Since this measurement has two possible outcomes labelled by 0 or 1 there are two Kraus operators $A_0 = |0\rangle\langle 0|$ and $A_1 = |1\rangle\langle 1|$, or equivalently:

$$A_0 = \begin{pmatrix} 1 & 0 \\ 0 & 0 \end{pmatrix}, \qquad A_1 = \begin{pmatrix} 0 & 0 \\ 0 & 1 \end{pmatrix}. \tag{3.3}$$

Applying Eq. 3.1 and Eq. 3.2 to compute the post-measurement density matrix $\hat{\rho}'$ gives

$$\hat{\rho} = \begin{pmatrix} |c_0|^2 & c_0 c_1^* \\ c_0^* c_1 & |c_1|^2 \end{pmatrix} \longrightarrow \hat{\rho}' = \begin{pmatrix} |c_0|^2 & 0 \\ 0 & |c_1|^2 \end{pmatrix}, \tag{3.4}$$

with measurement outcome probabilities of $\lambda_0 = |c_0|^2$ and $\lambda_1 = |c_1|^2$.

If instead a quantum state is described in a *continuous* basis, its measurement can be described by a continuum of infinitely many Kraus operators. For example, measurement along the x-quadrature of a coherent state $|\alpha\rangle$, using an ideal homodyne detector, is described by the Kraus operators $A_x^\dagger = A_x = |x\rangle\langle x|$ corresponding to the POVM,

$$\Pi_x = |x\rangle\langle x|. \tag{3.5}$$

For these Kraus operators and the pre-measurement density matrix $\hat{\rho} = |\alpha\rangle\langle\alpha|$, Eq. 3.1 and Eq. 3.2 give the post-measurement density matrix $\hat{\rho}' = \Sigma_x \lambda_x |x\rangle\langle x|$, where magnitude $\lambda_x = |\langle x|\alpha\rangle|^2 = \sqrt{2/\pi} e^{-2(x-|\alpha|\sin\theta)^2}$ follows a Gaussian distribution, Eq. 2.47.

As we discuss later in Sec. 3.3.3, measurement of a quantum state may be done with added noise and/or loss before detection, with imperfection quantified by the 'measurement efficiency' $0 \leq \eta \leq 1$. While Eq. 3.5 gives the Kraus operators for an ideal homodyne detector, defined here to mean $\eta = 1$, the Kraus operators for a general homodyne detector are $A_x^\dagger = A_x = \frac{1}{\sqrt{\Delta_\eta \sqrt{2\pi}}} \int_{-\infty}^{\infty} dx'\, e^{-(x-x')^2/4\Delta_\eta^2} |x'\rangle\langle x'|$ with POVM [102]:

$$\Pi_x = \frac{1}{\sqrt{2\pi\Delta_\eta^2}} \int_{-\infty}^{\infty} dx'\, e^{-(x-x')^2/2\Delta_\eta^2} |x'\rangle\langle x'|. \tag{3.6}$$

Physically, $\Delta_\eta = \sqrt{(1-\eta)/4\eta}$ is a standard deviation parameterizing the noise added by the detector,[2] equivalent to loss caused by a beamsplitter of transmissivity η between state preparation and an ideal homodyne detector. In the limit of $\eta \to 1$ corresponding to $\Delta_\eta \to 0$, Eq. 3.6 reduces to Eq. 3.5. Applying Eq. 3.1 and Eq. 3.2, using Eq. 3.6, gives the post-measurement density matrix $\hat{\rho}' = \Sigma_x \lambda_x |x\rangle\langle x|$, where magnitude $\lambda_x = \sqrt{2\eta/\pi} e^{-2\eta(x-|\alpha|\sin\theta)^2}$ follows a Gaussian distribution whose standard deviation is $1/\left(2\sqrt{\eta}\right)$, taking a minimum value of $1/2$ at $\eta = 1$. Such a measurement gives the same signal-to-noise ratio as using an ideal homodyne detector to measure a coherent state whose displacement $|\alpha|\sin\theta$ along the measured quadrature is first reduced by the factor $\sqrt{\eta}$.

3.1.3 Measurement induced dephasing

Notice from Eq. 3.4 that a qubit prepared in a superposition state, for instance taking $c_0 = c_1 = 1/\sqrt{2}$ for a qubit prepared along the equator of the Bloch sphere, is taken to a mixed state after measurement. In other words the qubit is *dephased* by measurement. For the Kraus operators in Eq. 3.3 this measurement is *projective*, such that the post-measurement state $\hat{\rho}'$ falls entirely along the z-axis of the Bloch sphere.

For a different type of measurement, the post-measurement qubit state need not be entirely dephased, or equivalently the post-measurement density matrix might still have some non-zero off-diagonal value. For example, consider the common scenario of a qubit prepared in a superposition state and then entangled with a measurement system in the state $|\varphi_0\rangle$ or $|\varphi_1\rangle$ to create the bipartite state

$$|\psi\rangle = \frac{1}{\sqrt{2}}\left(|0\rangle|\varphi_0\rangle + |1\rangle|\varphi_1\rangle\right), \tag{3.7}$$

with density matrix $\hat{\sigma} = |\psi\rangle\langle\psi|$ describing the joint state of the qubit and the measurement system. For the POVM element $\Pi_x = \mathbb{I} \otimes |x\rangle\langle x|$, Eq. 3.1 gives the following state after obtaining the measurement outcome x:

$$\hat{\sigma}'_x = \frac{1}{2\lambda_x} \begin{pmatrix} |\langle x|\varphi_0\rangle|^2 & \langle x|\varphi_0\rangle\langle\varphi_1|x\rangle \\ \langle x|\varphi_1\rangle\langle\varphi_0|x\rangle & |\langle x|\varphi_1\rangle|^2 \end{pmatrix} \otimes |x\rangle\langle x|, \tag{3.8}$$

[2] Note that the noise added by the detector is assumed here to follow a Gaussian distribution.

where $\lambda_x = \mathrm{Tr}\left(\Pi_x \hat{\sigma}\right)$. Summing Eq. 3.8 over all measurement outcomes as in Eq. 3.2 and taking the partial trace over the second system gives the average density matrix $\hat{\rho}' = \mathrm{Tr}_2\left(\sum_x \lambda_x \hat{\sigma}'_x\right)$ of the qubit after measurement:[3]

$$\hat{\rho}' = \frac{1}{2}\begin{pmatrix} 1 & \langle\varphi_1|\varphi_0\rangle \\ \langle\varphi_0|\varphi_1\rangle & 1 \end{pmatrix}. \tag{3.9}$$

In other words, the projective measurement on the ancilla via POVM element Π_x transforms the pure qubit state into the mixed state given by Eq. 3.9.[4] Qubit coherence (the off-diagonal density matrix element of the qubit) will be reduced by the inner product $\langle\varphi_1|\varphi_0\rangle$, i.e. the extent to which $|\varphi_0\rangle$ and $|\varphi_1\rangle$ are orthogonal.

3.1.4 Environment induced dephasing

The concepts of measurement and dephasing can now be connected more generally. 'Dephasing' describes any process where a qubit prepared in a superposition state reduces to a mixed state, corresponding to its off-diagonal matrix elements $\hat{\rho}'_{01}$ diminishing in magnitude.

In a *projective* measurement, as in Eq. 3.4, it is simple to think of this dephasing as happening at a specific moment. Any physical qubit, however, will also naturally dephase over time as it interacts with its environment. A qubit's energy relaxation rate $\Gamma_1 = 1/T_1$ and dephasing rate $\Gamma_2 = 1/T_2^*$ evolve its density matrix over time according to [81]

$$\hat{\rho}'(t) = \begin{pmatrix} 1 + \left(|c_0|^2 - 1\right) e^{-\Gamma_1 t} & c_0 c_1^* e^{-\Gamma_2 t} \\ c_0^* c_1 e^{-\Gamma_2 t} & |c_1|^2 e^{-\Gamma_1 t} \end{pmatrix}, \tag{3.10}$$

for a qubit starting in state $c_0\,|0\rangle + c_1\,|1\rangle$ at time $t = 0$. The dephasing rate is the sum of half the energy relaxation rate $\Gamma_1 = 1/T_1$ and the 'pure' dephasing rate $\Gamma_\phi = 1/T_\phi$ such that $1/T_2^* = 1/2T_1 + 1/T_\phi$. In the limit where the qubit's energy relaxation rate T_1 goes to infinity, then $\Gamma_2 \to \Gamma_\phi$.

[3] The partial trace $\mathrm{Tr}_2(\cdot)$ is defined as the unique linear operator satisfying $\mathrm{Tr}_2(X \otimes Y) = X\mathrm{Tr}(Y)$ for any two operators X and Y. When applied to a bipartite state, the partial trace Tr_2 yields the marginal of the first constituent system.

[4] Note that Eq. 3.9 holds regardless of the value of measurement efficiency η, or equivalently when using the POVM given in Eq. 3.6 rather than Eq. 3.5.

As $\Gamma_\phi t \to \infty$, the qubit has been 'dephased' into a mixed state falling along the z-axis of the Bloch sphere. Assuming $\Gamma_1 = 0$, the qubit's post-measurement density matrix is not distinguishable from that after a projective measurement, Eq. 3.4. Therefore measurement and dephasing are in a sense the same operation. Dephasing can be understood as the qubit being 'measured' due to interaction with degrees of freedom in the environment, with the measurement results hidden insofar as the environment cannot be probed to gain information about the qubit state.

In superconducting qubits dispersively coupled to readout cavities, pure dephasing is often dominated by the presence of a thermal state in the readout cavity (as opposed to vacuum) [103, 104]. When the mean thermal photon number in the readout cavity $\bar{n}_{\text{th}}$ is much less than one, the pure dephasing rate due to thermal photons is [105, 106],

$$\Gamma_\phi = \frac{4\kappa_r \chi^2}{\kappa_r^2 + 4\chi^2} \bar{n}_{\text{th}}. \tag{3.11}$$

Here, χ is the dispersive shift defined such that the readout cavity shifts by $\pm\chi/2\pi$ dependent on the qubit state (as in Eq. 2.53), and κ_r is the energy decay rate of the readout cavity.

3.2 Dispersive readout

In dispersive readout of superconducting qubits [15], it is typical to scatter a coherent state[5] off of a readout cavity and then measure the amplitude and/or phase of the scattered pulse. A coherent state in the readout cavity becomes entangled with the qubit to make the bipartite state

$$|\psi\rangle = \frac{1}{\sqrt{2}} \left(|0\rangle |\alpha_0\rangle + |1\rangle |\alpha_1\rangle \right). \tag{3.12}$$

Note the similarity to Eq. 3.7, where $|\varphi_0\rangle = |\alpha_0\rangle$ and $|\varphi_1\rangle = |\alpha_1\rangle$, illustrated in Fig. 3.1a. These states have equal amplitudes $|\alpha|$ but are separated by a maximum angle $2\theta = 2\arctan(2\chi/\kappa_r)$ in quadrature space, Fig. 3.1a.[6]

From Eq. 2.45, a normalized coherent state in the quadrature basis has the property: $\langle x|\alpha\rangle = \left(\frac{2}{\pi}\right)^{1/4} e^{-i|\alpha|^2 \sin(2\theta)/2} e^{-\left[(x - \text{Re}[\alpha])^2 - 2ix\text{Im}[\alpha]\right]}$, where $\text{Re}[\alpha] = |\alpha| \sin\theta$ and $\text{Im}[\alpha] = |\alpha| \cos\theta$. Note that

[5] See Sec. 2.2.3 for a review of coherent states

[6] The angle 2θ is found by computing $\arg[S_{21}(\omega)]$ using Eq. 2.58 for $\delta = \pm\chi$ and $\kappa = \kappa_r$.

in this definition, $\langle x|\alpha\rangle$ is a Gaussian function with a standard deviation of $1/\sqrt{2}$, variance of $1/2$, and that $|\langle x|\alpha\rangle|^2 = \sqrt{2/\pi}e^{-2(x-|\alpha|\sin\theta)^2}$. Therefore $|\langle x|\alpha\rangle|^2$, the modulus-squared of the coherent state, has a standard deviation of $1/2$ and a variance of $1/4$, as per the convention in Refs. [86, 87]. From Eq. 3.9, the qubit after measurement is in a mixed state with coherence $\hat{\rho}'_{01} = \frac{1}{2}\langle\alpha_0|\alpha_1\rangle$. Evaluating this gives

$$\hat{\rho}' = \frac{1}{2}\begin{pmatrix} 1 & e^{-2|\alpha|^2\sin^2\theta} \\ e^{-2|\alpha|^2\sin^2\theta} & 1 \end{pmatrix}, \tag{3.13}$$

as in Eq. 2.49. As $|\alpha| \to \infty$, qubit coherence vanishes and Eq. 3.13 reduces to the density matrix of a qubit prepared in a superposition state and then projectively measured. Eq. 3.13 also concludes that dephasing goes to zero in the limit where $\theta \to 0$ such that $\chi \ll \kappa_r$. This makes sense — a readout signal much more strongly coupled to the environment than to the qubit will dissipate before becoming entangled with the qubit.

With no readout signal, $|\alpha| = 0$, a qubit may still be dephased by the excess backaction of a detector (for example, due to finite isolation between the qubit and amplifier). This backaction is parameterized as another coherent state $|\alpha_b\rangle$ interacting with the qubit, where $\alpha_b = |\alpha_b|e^{i\theta_b}$. Post-measurement qubit coherence is then modified to

$$|\hat{\rho}'_{01}| = \rho_b e^{-2|\alpha|^2\sin^2\theta}, \tag{3.14}$$

where $0 \leq \rho_b = \frac{1}{2}e^{-2|\alpha_b|^2\sin^2\theta_b} = \frac{1}{2}e^{-2n_b} \leq 1/2$ is the dephasing in excess of that caused by the readout pulse, or equivalently

$$n_b = -\frac{1}{2}\log\left(2\rho_b\right), \tag{3.15}$$

where $n_b = |\alpha_b|^2\sin^2\theta$ is the mean photon number of this backaction. Here, we have assumed that the state $|\alpha_b\rangle$ caused by detector backaction entangles with the qubit and is measured either before or after the readout pulse $|\alpha\rangle$, so that $|\alpha_b\rangle$ and $|\alpha\rangle$ do not interfere with each other.

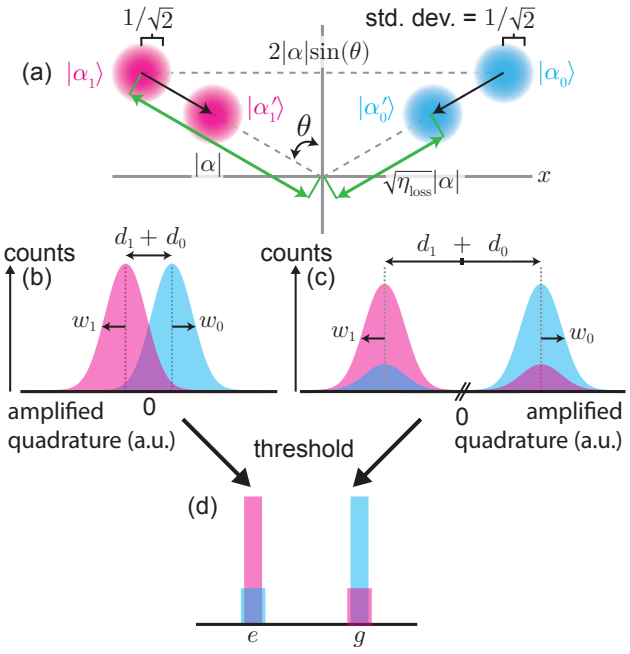

Figure 3.1: **Dispersive readout model.** (a) A coherent state of amplitude $|\alpha|$, whose state $|\langle x|\alpha\rangle\langle\alpha|y\rangle|$ is illustrated by a blob in phase space, is a Gaussian function with a single quadrature standard deviation $1/\sqrt{2}$ (see Eq. 2.45 and Eq. 2.46). Loss before a detector scales the amplitude of this coherent state by $\sqrt{\eta_{\text{loss}}}$ to create $|\alpha_0'\rangle$ and $|\alpha_1'\rangle$, here assuming that $\eta = \eta_{\text{loss}}$. (b) Linear measurement along the x-quadrature yields the cyan (pink) distribution if the qubit was prepared in the ground (excited) state. The height of these distributions are proportional to $|\langle x|\alpha_0'\rangle|^2$ and $|\langle x|\alpha_1'\rangle|^2$, such that their standard deviations w_0 and w_1 represent the coherent state variance. After noiseless parametric amplification, the experimentally measured signal-to-noise ratio (SNR) is defined according to Eq. 3.17. Errors due to finite SNR (b) and preparation infidelity (c), are not distinguishable when a linear measurement result is thresholded as shown in (d). This is true regardless of whether the thresholding is due to use of a bifurcation amplifier, or due to post-processing of a linear measurement. However, thresholding due to the non-unitary dynamics of a bifurcation amplifier is fundamentally irreversible.

3.3 Measurement efficiency

3.3.1 Definition

As a qubit is dephased by measurement, classical information about the qubit state may also be gained. As given by Eq. 3.14, the amount of dephasing — and therefore possible information gain — is a function of the separation in phase space between coherent states $|\alpha_0\rangle$ and $|\alpha_1\rangle$. In practice, loss present between the qubit and detector will diminish this separation before $|\alpha_0\rangle$

and $|\alpha_1\rangle$ can be measured. Loss scales the measured coherent state amplitudes by $|\alpha| \to \sqrt{\eta_{\text{loss}}}|\alpha|$, where $0 \leq 1-\eta_{\text{loss}} \leq 1$ is the fraction of readout energy remaining immediately before amplification, Fig. 3.1a. The total efficiency of a measurement chain, i.e. its *measurement efficiency*,[7] is equal to $\eta = \eta_{\text{loss}}\eta_{\text{amp}}$, where $0 \leq \eta_{\text{amp}} \leq 1$ is the efficiency of the amplifier chain (quantifying its added noise). In Ref. [23], we measure η but can assume $\eta_{\text{amp}} = 1$ and therefore $\eta = \eta_{\text{loss}}$, because we use a phase-sensitive parametric amplifier which in principle adds no noise along the amplified quadrature.

3.3.2 Linear measurement

Loss before measurement transforms $|\alpha_0\rangle$ and $|\alpha_1\rangle$ to the states $|\alpha_0'\rangle$ and $|\alpha_1'\rangle$, respectively, Fig. 3.1a. The ability of a detector to discriminate $|\alpha_0'\rangle$ and $|\alpha_1'\rangle$ may be quantified by a signal-to-noise ratio (SNR) [24]. We define SNR [75, 13] as the separation in phase space between these states divided by their single quadrature standard deviation of $1/\sqrt{2}$. The expected SNR of a measurement along the x-quadrature is therefore

$$\text{SNR} = \sqrt{8\eta}|\alpha|\sin\theta. \tag{3.16}$$

Referring to Fig. 3.1b,c, this is equal to the experimentally measured value of

$$\text{SNR} = \frac{|d_1 + d_0|}{\sqrt{w_1^2 + w_0^2}}, \tag{3.17}$$

where $|d_1 + d_0|$ is the separation between the two measured histograms (corresponding to the qubit in the ground/excited state), and $w_1 = w_0$ are the standard deviations of these histograms (corresponding to the coherent state variance).

Eq. 3.14 and Eq. 3.16 can be used together to quantify the efficiency of a linear measurement

$$\eta = \frac{\text{SNR}^2}{-4\log\left(|\hat{\rho}_{01}'|/\rho_b\right)}, \tag{3.18}$$

which is a function of the experimentally measurable quantities of $|\hat{\rho}_{01}'|$, ρ_b and SNR. For any readout amplitude $|\alpha|$, measurement of SNR and dephasing $|\hat{\rho}_{01}'|/\rho_b$ thus determines η. It is expedient

[7] Note that measurement efficiency has also been referred to as 'quantum efficiency' or simply 'efficiency' in the superconducting qubit literature [24, 36, 107, 76, 78, 77, 49, 75].

to simplify this determination by measuring $|\hat{\rho}'_{01}|$ and SNR at different values of readout amplitude. Consider a readout amplitude in the experimental units ϵ proportional to $|\alpha|$ (e.g. voltage bias on a mixer). From Eq. 3.16, SNR will increase linearly with ϵ. From Eq. 3.14, qubit coherence is reduced as a Gaussian function of the readout amplitude ϵ. Therefore,

$$\text{SNR} = a\epsilon, \qquad |\hat{\rho}'_{01}(\epsilon)| = \rho_b e^{-\epsilon^2/2\sigma^2}, \tag{3.19}$$

where a is a constant of proportionality and σ is a Gaussian standard deviation. Substituting these expressions into Eq. 3.18 and solving for η gives

$$\eta = \frac{a^2\sigma^2}{2}. \tag{3.20}$$

Eq. 3.20 gives the measurement efficiency in terms of σ and a, experimental quantities which are determined from fits to measurements of $|\hat{\rho}'_{01}|$ and SNR as functions of the readout amplitude ϵ. We reiterate that in Eq. 3.20 and Ref. [23], we define measurement efficiency such that $\eta = 1$ when using an ideal, phase-*sensitive* amplifier, with no other loss or added noise introduced by the detector.[8]

3.3.3 Bifurcated measurement

The measurement discussed in Ref. [23], however, does not use a linear amplifier. Pumping a parametric amplifier into bifurcation is a non-unitary process which destroys information: all possible input states are irreversibly mapped to two output states, illustrated by the distribution in Fig. 3.1d. Finite SNR and preparation infidelity are indistinguishable after thresholding which prevents a direct measurement of SNR for use in Eq. 3.18 and thus Eq. 3.20.

To understand the efficiency of a bifurcated measurement, we instead consider the qubit

[8] Note that Ref. [77] derives an expression which is written identically to Eq. 3.20, but whose derivation contains two differences from ours. First, Ref. [77] defines unit measurement efficiency to correspond to an ideal phase-*preseving* amplifier, such that $0 \leq \eta \leq 1/2$ accordingly to our definition. Second, SNR is defined in Ref. [77] to equal $(d_1 + d_0)/w$ (taking $w_1 = w_0 = w$, referring to our Fig. 3.1), which differs from our definition in Eq. 3.17. Our definition of SNR is chosen to keep with the convention in Refs. [75, 13], and references therein. In practice, such conflicting definitions can be a source of confusion, and it is important to make sure that the definitions for η and SNR are consistent with the formula being used.

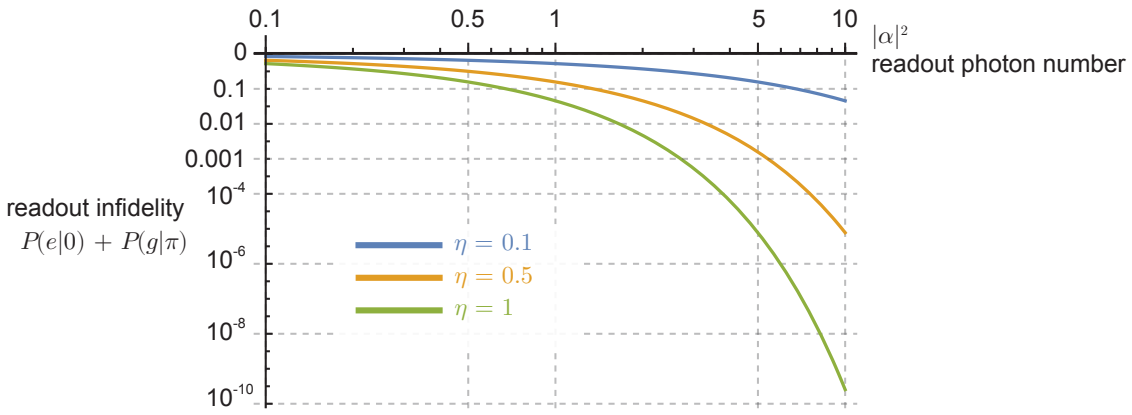

Figure 3.2: **Readout infidelity vs. photon number.** Readout infidelity $1-F_r = P(e|0)+P(g|\pi)$ represents the inability to distinguish the coherent states $|\alpha_0\rangle$ and $|\alpha_1\rangle$, which are associated with the qubit states $|0\rangle$ and $|1\rangle$, respectively. A model for readout infidelity (see Eq. 3.24) is plotted vs. readout photon number $n_r = |\alpha|^2$ (assuming $\sin\theta = 1$ and $F_0 = 1$). At $|\alpha|^2 = 10$ photons, the states $|\alpha_0\rangle$ and $|\alpha_1\rangle$ can in principle be discriminated with error probability of less than 10^{-9}, far exceeding the performance threshold necessary for error correction. For $\eta = 0.1$, however, an error rate of several percent is expected. Given that the readout photon number cannot be arbitrarily increased due to unwanted nonlinearities [32, 33], high measurement efficiency is therefore important for high performing readout.

readout fidelity [108]

$$F_r = 1 - P(e|0) - P(g|\pi), \tag{3.21}$$

where $P(e|0)$ and $P(g|\pi)$ are the error probabilities of measuring the qubit to be in the excited (ground) state, when the qubit is prepared in the ground (excited) state, respectively, such that $0 \leq F_r \leq 1$. Intuitively, readout fidelity is the probability of the detector to correctly discriminate the state that the qubit has been prepared in: $F_r = \frac{1}{2}\left(P(e|\pi) - P(e|0)\right) + \frac{1}{2}\left(P(g|0) - P(g|\pi)\right)$.

Readout fidelity is limited by both finite readout amplitude and preparation infidelity. Preparation infidelities, p_0 and q_0, are defined as the probability of having prepared the qubit in the excited (ground) state when trying to prepare it in the ground (excited) state, respectively. These infidelities p_0 and q_0 define a maximum readout fidelity $F_0 = 1 - p_0 - q_0$.

To model the readout fidelity, we model our bifurcated measurement as a linear amplification whose result (a measured value along the x-quadrature, Fig. 3.1) is thresholded by its sign, assigning the qubit state to one of two distinct outcomes. Measurement error is the sum of correct state

preparation but incorrect assignment, and incorrect state preparation with correct assignment [108]:

$$P(e|0) = \int_{-\infty}^{0} dx \left[(1-p_0) \left| \langle x|\alpha_0' \rangle \right|^2 + p_0 \left| \langle x|\alpha_1' \rangle \right|^2 \right], \tag{3.22}$$

$$P(g|\pi) = \int_{0}^{\infty} dx \left[q_0 \left| \langle x|\alpha_0' \rangle \right|^2 + (1-q_0) \left| \langle x|\alpha_1' \rangle \right|^2 \right]. \tag{3.23}$$

Evaluating these integrals and plugging the results into Eq. 3.21 yields,

$$F_r = F_0 \mathrm{erf}\left[\sqrt{2\eta} |\alpha| \sin\theta \right]. \tag{3.24}$$

Note that the argument of Eq. 3.24 is always positive, since $0 \leq \theta \leq \pi/2$ as defined in Fig. 3.1a. Using Eq. 3.14, readout fidelity can be expressed in terms of the measurement induced dephasing

$$F_r = F_0 \mathrm{erf}\left[\sqrt{-\eta \log\left(|\hat{\rho}_{01}'| / \rho_b \right)} \right]. \tag{3.25}$$

In order to finally determine η, we use Eq. 3.25 to solve for η in a similar manner to how we obtained Eq. 3.20. Again, we consider readout amplitude in the experimental units of $\epsilon \propto |\alpha|$. From Eq. 3.24, readout fidelity will increase as an error function with respect to ϵ, and qubit coherence will still decrease as a Gaussian:

$$F_r(\epsilon) = F_0 \mathrm{erf}\left[\nu \epsilon \right], \tag{3.26}$$

$$\left| \hat{\rho}_{01}'(\epsilon) \right| = \rho_b e^{-\epsilon^2/2\sigma^2}. \tag{3.27}$$

Where ν and σ are obtained from fits of experimental data, e.g. Fig 3c. Using Eq. 3.24 and Eqs. 3.26 and 3.27 to solve for η gives

$$\eta = 2\nu^2\sigma^2. \tag{3.28}$$

Eq. 3.28 gives the measurement efficiency η in terms of σ and ν, quantities which can be experimentally determined from fits to measurements of $|\hat{\rho}_{01}'|$ and F_r as functions of ϵ.

3.4 Information Efficiency

The methods described in the previous section are specific to either a linear or bifurcated measurement. Alternatively, measurement of a qubit using *any* type of detector can be understood

in terms of information theory [109, 110]. In this section, qubit measurement is framed as the following questions: given a qubit prepared in a given state, how much information *could* be learned about the state given a specific type of detector? How much information was *actually* learned? Where here "information" follows a precise definition developed from information theory [111].

This analysis can be useful if the specific mechanism for qubit readout measurement is unclear or does not cleanly follow the models of Eq. 3.20 or Eq. 3.28. This analysis will also allow us to quantitatively compare the information gained by linear vs. bifurcated measurements.

3.4.1 Accessible information

When a qubit prepared in a superposition state $(|0\rangle + |1\rangle)/\sqrt{2}$ is measured, it is collapsed toward the eigenstate $|0\rangle$ or $|1\rangle$. How projective, or how strong, the measurement is quantifies this collapse. For two quantum states $|\varphi_0\rangle$ and $|\varphi_1\rangle$ of a measurement system which are entangled with the qubit as given by Eq. 3.7, this collapse is characterized by the 'error probability' r associated with discriminating $|\varphi_0\rangle$ and $|\varphi_1\rangle$. Error here, given by the Helstrom bound [112], is a function of the non-orthogonality of these states. For pure states $|\varphi_0\rangle$ and $|\varphi_1\rangle$ this minimum error probability is $r = \frac{1}{2}\left(1 - \sqrt{1 - |\langle\varphi_0|\varphi_1\rangle|^2}\right)$, which from Eq. 3.9 equals

$$r = \frac{1}{2} - \frac{1}{2}\sqrt{1 - 4|\hat{\rho}'_{01}|^2}, \tag{3.29}$$

with $0 \leq r \leq \frac{1}{2}$. The Helstrom bound has a simple geometric interpretation: Fig. 3.3 illustrates a qubit density matrix before and after measurement in the z-basis, such that a superposition state is partially projected onto $|0\rangle$, with some remaining phase coherence $|\hat{\rho}'_{01}|$. The error probability r is the remaining uncertainty of the post-measurement qubit state, equal to the length of the green vector.

Explicitly, consider the states $|\varphi_0\rangle$ and $|\varphi_1\rangle$ to be prepared with equal probability. We take that a measurement of $|\varphi_0\rangle$ occurs with error probability r_0, and a measurement of $|\varphi_1\rangle$ with error probability r_1. The probability of obtaining the measurement outcomes corresponding to $|\varphi_0\rangle$ or $|\varphi_1\rangle$ are therefore $s_0 = (1 - r_0)/2 + r_1/2$ and $s_1 = 1 - s_0$, respectively. The quantities $r_1/2s_0$ and

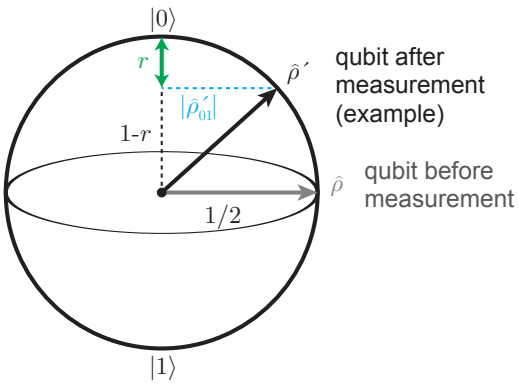

Figure 3.3: **The Helstrom bound.** A qubit is prepared in a superposition state $\hat{\rho}$ and non-projectively measured in the z-basis. For a given measurement outcome, the post-measurement qubit state is $|\phi\rangle = \sqrt{1-r}\,|0\rangle + \sqrt{r}\,|1\rangle$, with density matrix $\hat{\rho}' = |\phi\rangle\langle\phi|$. The projection of this state along the z-axis, $1-r$, quantifies the remaining uncertainty r about the qubit state. In this example a projection toward $|0\rangle$ is illustrated, but a projection toward $|1\rangle$ occurs with equal probability.

$r_0/2s_1$ are the fractional likelihoods of error, given by Bayes' theorem. This is generalizable to the case where $|\varphi_0\rangle$ and $|\varphi_1\rangle$ are prepared with different probabilities, but here we consider only the case of Eq. 3.7 for simplicity.

Measurement therefore gains *information* about the qubit state, quantified by the probabilities $r_1/2s_0$ and $r_0/2s_1$. As in Ref. [110], this information is quantified by the mutual information,

$$I = 1 - \left[s_0 H\left(\frac{r_1}{2s_0}\right) + s_1 H\left(\frac{r_0}{2s_1}\right) \right], \tag{3.30}$$

where $H(x) = -x\log_2(x) - (1-x)\log_2(1-x)$ denotes the binary entropy.

The accessible information I_{acc} is defined as the maximum possible mutual information I which may be obtained by a measurement. This occurs when the measurement error probabilities saturate the Helstrom bound, i.e., $r_0 = r_1 = r$ and $s_0 = s_1 = 1/2$. Eq. 3.30 then simplifies to

$$I_{\text{acc}} = 1 - H(r). \tag{3.31}$$

Note that I_{acc} is a function of *only* the post-measurement qubit density matrix $|\hat{\rho}'_{01}|$, on which r depends via Eq. 3.29.

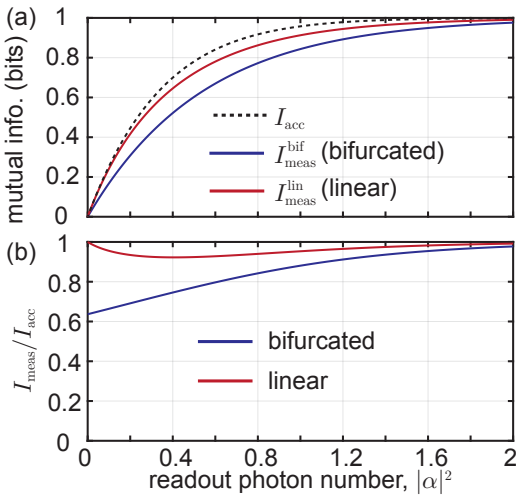

Figure 3.4: **Information gained by a qubit measurement.** (a) Accessible information, $I_{\rm acc}$ from Eq. 3.32, after the qubit is measured by a coherent state with amplitude $|\alpha|$ (dashed line, and assuming $\theta = \pi/2$). $I_{\rm acc}$ grows with $|\alpha|$, and (b) is always greater than or equal to the information gain from either a bifurcated (blue) or linear (red) measurement. Notice that for even a linear measurement (here meaning a homodyne detector with unit efficiency), $I_{\rm meas}$ remains less than $I_{\rm acc}$ when $0 < |\alpha|^2 < \infty$. For a description of other types of measurements which can saturate to $I_{\rm meas} = I_{\rm acc}$ within this range, e.g. a Dolinar receiver, see Refs. [113, 114, 115, 110].

3.4.2 Information gain

We can similarly determine the information attained by measurement. The information $I^{\rm bif}_{\rm meas}$ gained from a bifurcated measurement (here meaning two possible outcomes) is:

$$I^{\rm bif}_{\rm meas} = 1 - \frac{1}{2}H\left[P\left(e|0\right)\right] - \frac{1}{2}H\left[P\left(g|\pi\right)\right]. \tag{3.32}$$

Here, we take that $|\varphi_0\rangle = |\alpha\rangle$ and $|\varphi_1\rangle = |-\alpha\rangle$ (assuming $2\chi \gg \kappa_r$ such that $\theta = \pi/2$, for simplicity). Also for simplicity, we assume that preparation infidelity is zero, $p_0 = q_0 = 0$.

The probability of a measurement error for a bifurcated measurement, Eq. 3.23, therefore reduces to $P\left(e|0\right) = P\left(g|\pi\right) = \int_{-\infty}^{0} |\langle\alpha|x\rangle|^2\, dx = \frac{1}{2}\left(1 - \mathrm{erf}\left[\sqrt{2}|\alpha|\right]\right)$. This is plugged into Eq. 3.32 to model $I^{\rm bif}_{\rm meas}$.

Of course, a detector need not only give two measurements but instead can yield a continuum of outcomes. An example of this is a *linear* measurement such as homodyne detection of a coherent state which has been linearly amplified. To quantify information gain from a linear mea-

surement, consider discrimination between the pink and blue Gaussian distributions in Fig. 3.1b, which are prepared with equal likelihood of 1/2. If the qubit was prepared in the ground state (cyan distribution, Fig. 3.1), the probability of error for a measurement returning the value x is $r_x^0 = P(x|\pi) = \sqrt{2/\pi}e^{-2(x-|\alpha|)^2}$. And if the pink distribution corresponding to the qubit in the excited state was prepared, the probability of error is $r_x^\pi = P(x|0) = \sqrt{2/\pi}e^{-2(x+|\alpha|)^2}$. The probability of measuring the value x at all is the sum $s_x = \frac{1}{2}\left[P(x|0) + P(x|\pi)\right] = \frac{1}{2}\left(r_x^0 + r_x^\pi\right)$. At each x, the information acquired from measurement is the entropy of the normalized measurement probability, $H\left(r_x^0/s_x\right)$ or $H\left(r_x^\pi/s_x\right)$. The mutual information from measurement is the integral of these conditional entropies over all values x, weighted by the likelihood s_x of that measurement outcome occurring [109, 110],

$$I_{\text{meas}}^{\text{lin}} = 1 - \frac{1}{2}\int_{-\infty}^{\infty} dx \left[H\left(\frac{r_x^0}{s_x}\right) + H\left(\frac{r_x^\pi}{s_x}\right)\right] s_x, \tag{3.33}$$

where $I_{\text{meas}}^{\text{bif}} < I_{\text{meas}}^{\text{lin}}$ for $|\alpha| < \infty$, seen in Fig. 3.4a. As $|\alpha| \to \infty|$, however, both $I_{\text{meas}}^{\text{bif}}$ and $I_{\text{meas}}^{\text{lin}}$ saturate to unity. This means that thresholding a linear measurement destroys information, but only for the case of a weak or non-projective measurement.

Chapter 4

Josephson parametric amplifiers

4.1 Introduction to Josephson parametric amplifiers

Josephson parametric amplifiers (JPAs) are a type of superconducting parametric amplifier consisting of a resonant cavity with added nonlinearity due to the participation of one or more Josephson junctions [28, 29]. Such amplifiers have been developed over the past two decades in conjunction with other superconducting microwave technologies, and are routinely used for superconducting qubit readout. This chapter gives a brief introduction to JPAs and then analyzes the specific device used in Ref. [23].

In any parametric amplifier, a *pump* excitation at frequency ω_p is converted into *signal* and *idler* excitations at frequencies ω_s and ω_i, respectively. Such a process can be described by either 4-wave or 3-wave mixing. In 4-wave mixing, *two* pump photons[1] are converted to one signal and one idler photon (four photons total) such that $2\omega_p = \omega_s + \omega_i$ by energy conservation. In 3-wave mixing, *one* pump photon is converted to one signal and one idler photon (three photons total) such that $\omega_p = \omega_s + \omega_i$.

JPAs can also be colloquially categorized as either 'current-pumped' or 'flux-pumped', based on the manner in which the pump tone is operated. The nomenclature 'current-pumped' comes from the pump acting like a current source applied across the resonator's nonlinear element, typically achieved by applying a pump field incident on the JPA port as illustrated in Fig. 4.1a. The pump is

[1] 'Photon' assuming that the electromagnetic field is being amplified, but the theory is identical for any bosonic system (e.g. phonons).

Table 4.1: **Review of Josephson parametric amplifiers (JPAs).**

'current-pumped' JPA	'flux-pumped' JPA
4-wave mixing	3-wave mixing
pump near ω_0	pump near $2\omega_0$
linear amp example: Ref. [28]	linear amp example: Ref. [29]
bifurcation amp example: Ref. [27]	bifurcation amp example: Ref. [116]

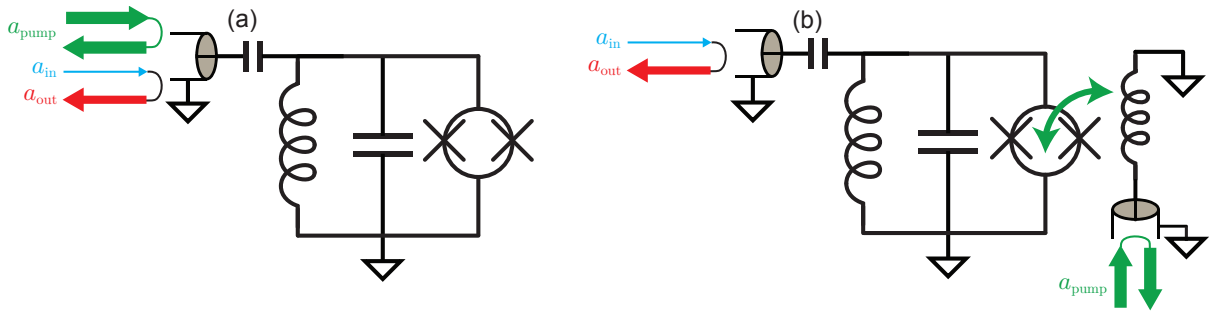

Figure 4.1: **Review of Josephson parametric amplifier (JPA) operation.** (a) Example schematic of a 'current-pumped' JPA. Signal, idler and pump photons enter and exit through a single port on the resonator. Typically, a pump near the resonance frequency $\omega_p \approx \omega_0$ provides two photons which are converted to signal and idler photons at frequencies $\omega_p \pm \delta$ where $\delta \lesssim \kappa$, the linewidth of the resonator. (b) Example schematic of a 'flux-pumped' JPA. Flux through a SQUID (or array of SQUIDs) participating in the resonator is modulated at twice the resonance frequency $\omega_p \approx 2\omega_0$, creating signal and idler photons at $(\omega_p \pm \delta)/2$ and amplifying an incident field. In both (a) and (b), the resonator frequency ω_0 can be tuned using an external dc flux often provided with an off-chip superconducting coil (not shown). In both styles of amplifier and when operated in the high gain limit, the input field (a_{in}, blue) is much weaker than the output field (a_{out}, red), and both are generally much weaker than the pump field (a_{pump}, green).

typically near the JPA resonance frequency in order to realize 4-wave mixing. Care must be taken to route the reflected pump signal away from any sensitive devices (e.g. a qubit/cavity system). The nomenclature 'flux-pumped' comes from modulating the flux through one or more SQUID loops in order to modulate a resonator's frequency at twice its natural frequency (3-wave mixing), realizing phase-sensitive parametric gain as described in Sec. 2.1.4.

These concepts are summarized in Table 4.1 and Fig. 4.1. The JPA in Ref. [23] is a 'flux-pumped' device which we operate in bifurcation mode. We focus on the theory of operation of this device for the remainder of this chapter. Further information on current-pumped JPAs is found in

Refs. [28, 84, 40, 85, 117, 118] and many references therein.

Finally, note that the bifurcation mode of operation qualitatively differs between current-pumped and flux-pumped devices. Bifurcation in current-pumped (4-wave mixing) devices is characterized by two stable states of different amplitude, as described by the physics of the driven Duffing oscillator [84]. Bifurcation in flux-pumped devices is characterized by two stable states of the same amplitude, but opposite phase [85]. Both styles are referred to as 'bifurcation amplifiers' in the literature — a potential source of confusion.

4.2 Flux-pumped Josephson parametric amplifier design

The JPA ('parametric cavity') in Ref. [23] is a two-port device whose lumped element schematic is given in Fig. 4.2a. A resonator is formed by an inductor (realized with a SQUID array similar to that in the TIBs), with 0.43 pF capacitors to ground on either side. When the SQUID array inductance is biased to be minimum, the array has an inductance of 0.66 nH. The geometric inductance of the resonator is 0.52 nH.

To turn on parametric gain, flux through these SQUIDs is modulated at twice the JPA resonance frequency using a microwave bias line (red, Fig. 4.2b), which contains an on-chip capacitor to block dc-current. Current through a second flux bias line (containing low pass filters) can be used to change the uniform dc-flux through the SQUID array, tuning the JPA frequency. A fingered capacitor (0.08 pF) is placed between the JPA and each TIB. This limits the coupling rate into/out of the JPA to $\kappa_p^s/2\pi = 52$ MHz when a TIB is in its maximal transmit mode, and when the JPA is tuned to 6.3 GHz.

4.3 Theory of operation

In this section we develop a theory of operation for the flux-pumped JPA used in Ref. [23]. We find that upon parametric amplification, the initial state is mapped to one of two specific locations in phase space, which are characterized by high amplitude ($\gg 1$ photon) but opposite phase. This classical analysis includes loss, parametric gain and nonlinearity, and expands upon

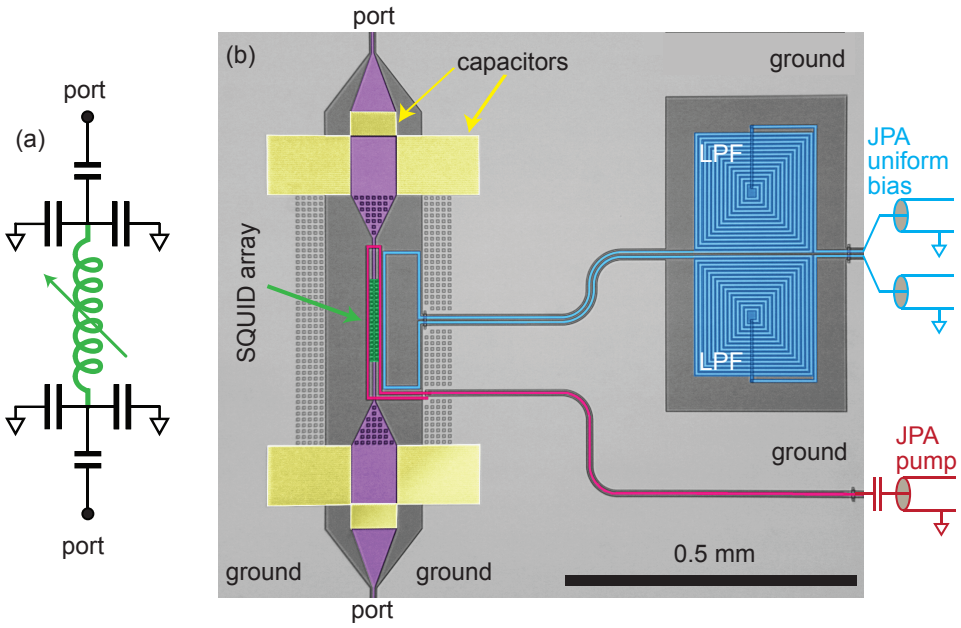

Figure 4.2: **JPA optical micrograph.** (a) Lumped element schematic of the JPA ('parametric cavity') integrated within the SIMBA described in Ref. [23]. The JPA consists of a 2-port LC-oscillator, whose tunable inductor is realized with an array of SQUIDs. The external coupling out of either port is tunable using TIBs (not shown). (b) False-color optical micrograph of this JPA. The SQUID array (green) is at the center of the image, and is surrounded by interdigitated finger capacitors (yellow), both to ground and connected to each port. Flux through the SQUID array can be controlled by two on-chip bias lines. One bias lines (red) is designed for the microwave frequency parametric cavity pump signal, and the other (blue) is designed to apply a dc flux to tune the parametric cavity frequency. Both bias lines contain low-pass filters (LPFs) realized with $\sim 20\,\mathrm{nH}$ spiral inductors (see Sec. 5.2.2 for more information).

simpler examples found in Chp. 2.1. Note that we neglect coupling of the JPA to its external environment (assuming the TIBs connected to both ports to be in reflect mode), and therefore build our analysis upon the circuit in Fig. 4.3. As elsewhere in this thesis, zero temperature is assumed.

4.3.1 Full equations of motion

The equations of motion for the circuit in Fig. 4.3 are two coupled first order differential equations governing the evolution of flux $\Phi(t)$ across the inductor l, and charge $q(t)$ across the

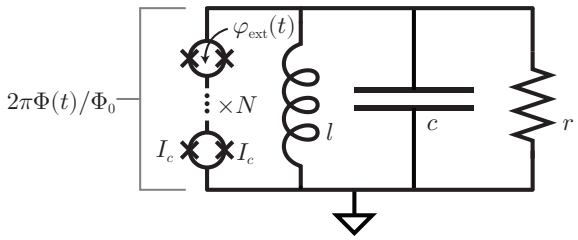

Figure 4.3: **Parametric cavity model.** A parametric amplifier is modelled as a parallel combination of a resistor r, capacitor c, linear inductor l, and array of N dc-SQUIDs. These SQUIDs are assumed to be comprised of identical Josephson junctions with critical current I_c. The phase difference across the SQUID array is $2\pi\Phi(t)/\Phi_0$, where $\Phi(t)$ is the branch flux accross the array and $\Phi_0 = h/2e$ is the magnetic flux quantum. The charge on the capacitor plates is $q(t)$. Note that this circuit has a slightly different topology from the circuit in Fig. 4.3, but results in equivalent dynamics but with simpler equations of motion to initially write down.

capacitor c. From Kirchoff's circuit laws, they are:

$$\dot{\Phi} = \frac{q}{c}, \tag{4.1}$$

$$\dot{q} = -\frac{\Phi}{l} - \frac{q}{rc} - I_{\text{array}}, \tag{4.2}$$

where $I_{\text{array}} = 2I_c \left|\cos\left(\varphi_{\text{ext}}/2\right)\right| \sin\left(2\pi\Phi/N\Phi_0\right)$ is the current flowing through the SQUID array as a function of flux across it (see Appx. A.3 for details).

It is useful to rewrite these equations in normal mode form (as in Sec. 2.1.1) given by,

$$a = \frac{1}{\sqrt{2\hbar}}\left(\frac{\Phi}{\sqrt{z_0}} + i\sqrt{z_0}q\right), \tag{4.3}$$

and its complex conjugate $a^\dagger$. Here, z_0 is the characteristic impedance of the resonator. The circuit equation of motion becomes,

$$\dot{a} = i\left[-\frac{a-a^\dagger}{2cz_0} - \frac{z_0}{2l}\left(a+a^\dagger\right) - \sqrt{\frac{z_0}{2\hbar}}I_{\text{array}}\right] - \frac{\kappa}{2}\left(a-a^\dagger\right), \tag{4.4}$$

where $\kappa = 1/rc$.

Note that the linear inductance in Eq. 4.4 is comprised both of the inductor l and the linear inductance of the SQUID array l_{array}. We first consider a static external flux bias $\varphi_{\text{ext}}(t) = \varphi_s$. Combining Eq. 4.4 together with Eq. A.8, it follows that the SQUID array adds a φ_s-dependent

linear inductance l_{array} in parallel to the inductor l. The resulting total linear inductance l_{res} of the device becomes,

$$\frac{1}{l_{\text{array}}} = \frac{2\pi}{\Phi_0}\frac{2I_c\cos\left(\varphi_s/2\right)}{N}, \qquad \frac{1}{l_{\text{res}}} = \frac{1}{l} + \frac{1}{l_{\text{array}}}. \tag{4.5}$$

The corresponding values for the resonator impedance and resonance frequency are,

$$z_0 = \sqrt{\frac{l_{\text{res}}}{c}}, \qquad \omega_0 = \frac{1}{\sqrt{l_{\text{res}}c}}. \tag{4.6}$$

The resonance frequency ω_0 is a 2π-periodic function of the static external flux bias φ_s. It assumes a maximum at $\varphi_s = 0$ and a minimum at $\varphi_s = \pm\pi$.

Next, we consider the parametric modulation of the SQUID critical current. This is achieved by a modulation of the external flux φ_{ext} through each SQUID around its static bias value,

$$\varphi_{\text{ext}}(t) = \varphi_s + \varphi_m\cos\left(\Omega t\right), \tag{4.7}$$

$$\Omega = 2\omega_0 + 2\delta. \tag{4.8}$$

where φ_m is the modulation amplitude and the pump detuning δ is assumed to be small, such that $\delta \ll \omega_0$.

4.3.2 Simplified equations of motion

Eq. 4.4, along with Eqs. 4.7 and 4.8 substituted into Eq. A.8, represent the full time-dependent equations of motion for the circuit in Fig. 4.3. These equations greatly simplify in certain realistic limits.

First, we consider only weak excitations $|2\pi\Phi/\Phi_0| \ll 1$, and in this limit we can expand the current-phase relation of the SQUID arrays in Eq. A.8. We also assume that for the entire modulation period, the resonator remains detuned from its maximum frequency such that $0 < \varphi_{\text{ext}}(t) < \pi$, so that we may ignore the absolute value in Eq. A.8. Finally, we assume weak parametric modulation amplitude $\varphi_m \ll 1$ so that $\cos(\varphi_{\text{ext}}/2) = \cos(\varphi_s/2) - (\varphi_m/2)\sin(\varphi_s/2)\cos(\Omega t) + \mathcal{O}\left(\varphi_m^2\right)$. In these limits, the circuit equation of motion then becomes,

$$\dot{a} = i\left[-\omega_0 a + \gamma\cos\left(\Omega t\right)\left(a + a^\dagger\right) + \frac{\zeta}{3}\left(a + a^\dagger\right)^3\right] - \frac{\kappa}{2}\left(a - a^\dagger\right). \tag{4.9}$$

Where we have defined an effective parametric drive amplitude γ and an effective nonlinearity ζ,

$$\gamma = \frac{\varphi_m \tan(\varphi_s/2)\, z_0}{4 l_{\text{array}}}, \tag{4.10}$$

$$\zeta = \frac{(2e)^2}{\hbar} \frac{z_0^2}{8 N^2 l_{\text{array}}}, \tag{4.11}$$

where e is the charge of an electron.

Finally, we transform Eq. 4.9 to the rotating frame such that $a = Ae^{-i\Omega t/2}$ and $\dot{a} = \left(\dot{A} - i\Omega A/2\right) e^{-i\Omega t/2}$, where A is the cavity field amplitude in the rotating frame. Averaging over fast oscillations removes explicit time-dependence, and the equation of motion simplifies to,

$$\dot{A} = i\delta A + i\frac{\gamma}{2} A^\dagger + i\zeta |A|^2 A - \frac{\kappa}{2} A. \tag{4.12}$$

Solutions to Eq. 4.12 are plotted in Fig. 4.4a,b for the parameters used in Ref. [23].

4.3.3 Phase diagram

We now examine stable solutions to Eq. 4.12. For absent or small parametric pumping, $\gamma \leq \kappa$, Eq. 4.12 has only the trivial solution $A = 0$. However, for $\gamma > \kappa$, Eq. 4.12 admits non-trivial steady-state solutions, a phenomenon known as parametric oscillation. One finds two stable, nontrivial steady states $A = |A| e^{i\theta_{\text{po}}}$ to Eq. 4.12, both with the same amplitude,

$$|A|^2 = \frac{1}{\zeta} \left(-\delta + \frac{1}{2} \sqrt{\gamma^2 - \kappa^2} \right), \tag{4.13}$$

but with π-shifted phases which are determined by $\sin(2\theta_{\text{po}}) = \kappa/\gamma$. Here $|A|^2$ is the steady-state photon number in the resonator. From Eq. 4.13, we can see that these states appear only for $\gamma > \kappa$ and $\delta < \delta_{\text{th}} = \frac{1}{2}\sqrt{\gamma^2 - \kappa^2}$. In the parameter regime $\gamma > \kappa$ and $|\delta| < \delta_{\text{th}}$ the trivial state $A = 0$ is instable, while for $\gamma > \kappa$ and $\delta < -\delta_{\text{th}}$ it coexists as a stable state with the parametric oscillation states [85, 116, 119]. The bistable region in parameter space is graphically illustrated in Fig. 4.4c for the parameters used in Ref. [23].

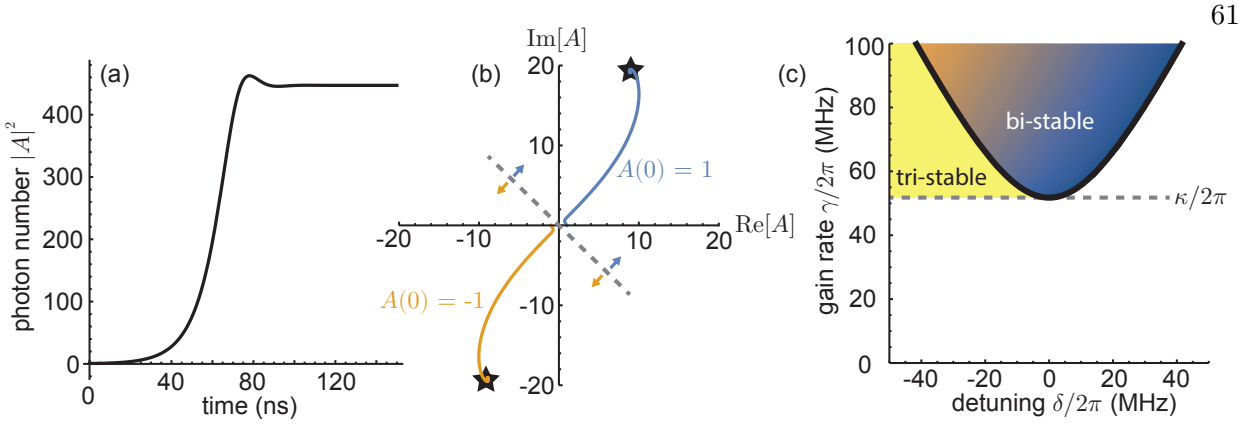

Figure 4.4: **Parametric oscillator dynamics.** (a) The modulus squared of the field in a parametric cavity $|A(t)|^2$, in the rotating wave equation (solution to Eq. 4.12). Using a boundary condition of $A(0) = 1$ or $A(0) = -1$ and $\dot{A}(0) = 0$ at $t = 0$, and a parametric gain rate of $\gamma/2\pi = 68\,\text{MHz}$, loss rate of $\kappa/2\pi = 52\,\text{MHz}$, pump detuning of $\delta/2\pi = 0$ and nonlinearity of $\zeta/2\pi = 49\,\text{kHz}$ as in Ref. [23]. The field in the oscillator exponentially increases until it reaches a steady-state value of approximately 400 photons. (b) Solutions to the same simulation plotted in the complex plane. For an initial state near the origin in phase space, the state of the oscillator will be pulled toward one of two attractors (black stars), which are π out-of-phase from each other and represent stable solutions to Eq. 4.12. The gray dashed line approximately specifies which initial conditions are mapped to which attractor. The closer κ is to γ, the more directly the oscillator approaches the attactor in phase space. (c) Phase diagram for the parametric oscillator. When gain exceeds loss ($\gamma > \kappa$) and detuning of the pump frequency from twice the resonator frequency is small enough such that $|\delta| < \frac{1}{2}\sqrt{\gamma^2 - \kappa^2}$ (Eq. 4.13), the oscillator is bistable as in (a) and (b). The color scale indicates the steady-state photon number $|A|^2$ with gold or blue indicating higher or lower photon numbers, respectively. For large enough negative detunings, the oscillator can become tri-stable with a third attactor at the origin [85, 116, 119]. For $\gamma \leq \kappa$ and/or large enough positive detunings (white region), the dynamics have only one attractor at the origin representing the trivial solution $A(t \to \infty) = 0$. Asymmetry in the steady-state amplitude as a function of detuning is controlled by the sign of the Kerr constant, and the tri-stable region occurs on the side of the bi-stable region for which the steady state amplitude is higher (here the red detuned side). At high enough gain rates and field amplitudes, higher order nonlinearities will change this phase diagram and can lead to greater numbers of stable states [85, 120].

4.4 Performance

4.4.1 Tunability

We frst characterize the JPA within a SIMBA by setting TIB2 to transmit mode and measuring in reflection off of TIB2. Doing so in Ref. [23], we find that the JPA frequency is tunable between approximately 4 and 7 GHz (Fig. 4.5), a similar range over which the TIB is designed to

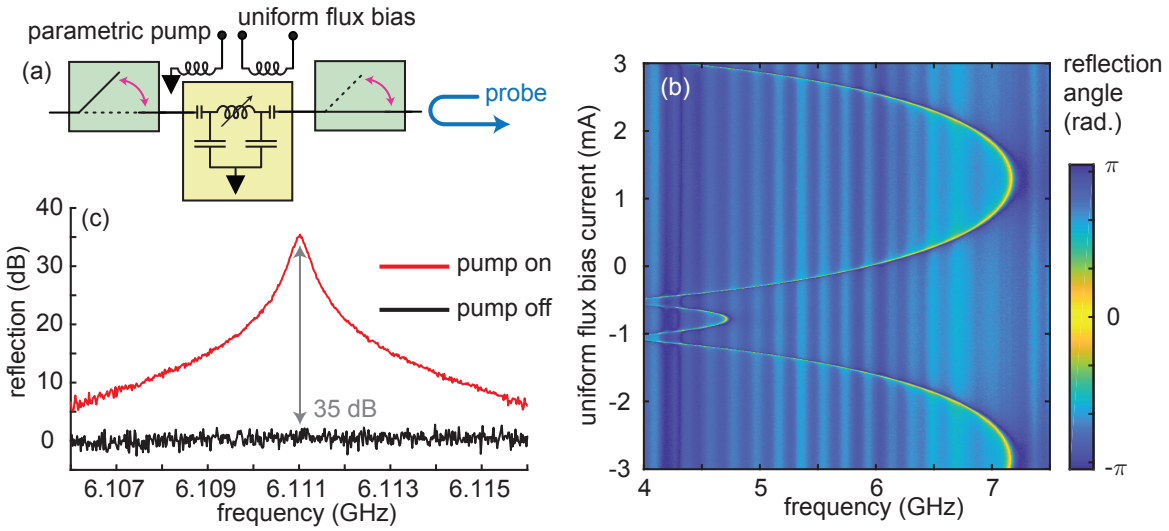

Figure 4.5: **JPA characterization.** (a) The JPA within the SIMBA is characterized when TIB1 is set to reflect mode and TIB2 is set to transmit mode. Reflection off of TIB2 is measured. (b) The JPA resonance frequency is tuned by changing a uniform flux through its SQUID array, applied by current through its on-chip dc bias line (blue, Fig. 4.2b). (c) When the JPA is pumped near resonance at the correct amplitude, it operates as a linear amplifier [95]. In the example shown here, the JPA is tuned to give greater than 20 dB of gain over a 2.2 MHz range, with a maximum of 35 dB of gain.

operate. We emphasize that the SIMBA itself may therefore be tuned to operate over a several GHz frequency range.

Note that the flux tuning curve shown in Fig. 4.5b was taken when sweeping current through an on-chip bias line rather than through an off-chip coil. The rest of the data reported in Ref. [23] was taken in a separate cooldown, using an off-chip coil to tune the JPA frequency rather than the on-chip bias line. This functionality was temporarily removed out of concern for low-frequency noise in the on-chip bias line, which can cause the bifurcated amplifier state to become unstable, creating a source of readout error. With proper low frequency filtering, however, no off-chip coil is needed to operate the SIMBA reported in this work.

While in Ref. [23] we operate the JPA/SIMBA in the bifurcation regime, it can also be operated as a linear amplifier. This is tested in Fig. 4.5c, in which a low amplitude probe tone of variable frequency is reflected from one port of the SIMBA. When the parametric pump is turned

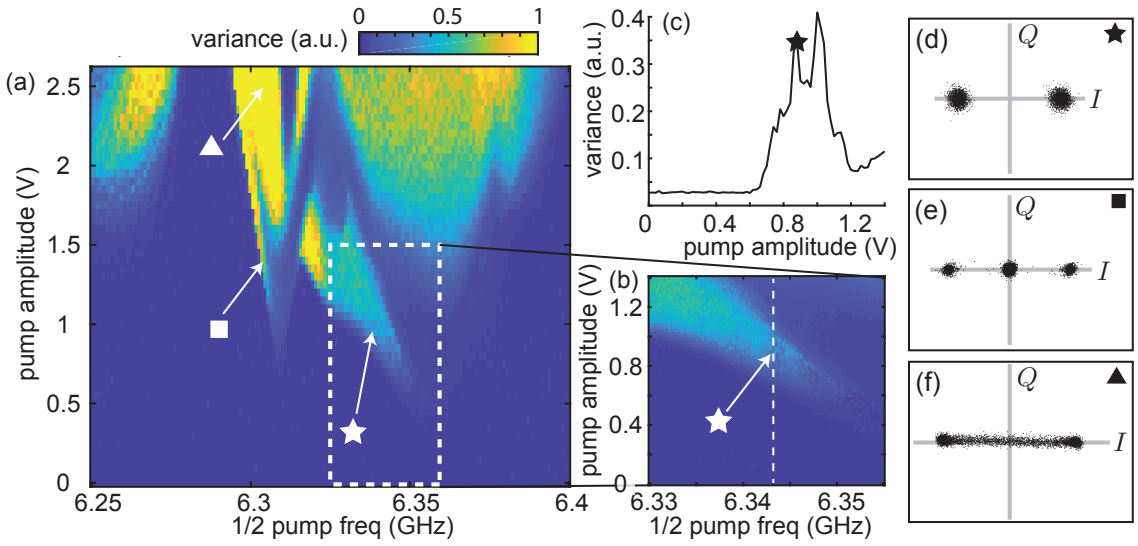

Figure 4.6: **Phase diagram for the pumped parametric cavity**. (a) We examine the behavior of the pumped parametric cavity by computing the variance of the distribution of single-shot measurements in the I/Q plane, i.e. the sum of I and Q variances. This is plotted as a function of pump half-frequency and pump amplitude (in units of voltage bias on a double balanced mixer used to modulate the pump amplitude). Note that for each measurement the state of the parametric cavity was near vacuum, and then the pump was pulsed on (no readout pulse to seed the cavity state). (b) A higher resolution sweep of the boxed region in (a), and (c) a vertical linecut (the dashed white line in (b)) of variance vs. pump amplitude at the half-pump frequency used for qubit readout. The star indicates the pump amplitude used in Ref. [23]. (d) At this operating point, the oscillator latches into one of two stable steady states. Each black dot is a single shot measurement. (e) At a negative detuning and higher pump amplitude, we can see three stable states, one at the origin [119]. (f) At even higher pump amplitudes, the oscillator jumps at random between two quasi-stable states, averaging to the distribution shown.

on near the JPA resonance frequency, linear gain of up to 35 dB is observed (red line).

4.4.2 Bifurcation

In general, noise and nonlinear terms in the resonator equations of motion will lead to more exotic behavior than predicted by the model in Sec. 4.3, which assumes 'small' nonlinearity taking the limit $|\Phi/\Phi_0| \ll 1$. Such behavior can complicate calibration of a SIMBA and can limit its performance. To understand any such effects, we map the region in parameter space where robust bifurcation is observed, Fig. 4.6. To do so, we make single-shot measurements of the pumped parametric cavity with TIB2 in transmit mode, TIB1 in reflect mode, and no readout or qubit

pulses. The variance of the set of these measurements in the I/Q plane is plotted as the color axis in Fig. 4.6a,b. Variance above the background level indicates a pumped parametric cavity state which is no longer vacuum, including the presence of parametric oscillation. Stable bifurcation is observed when pumping near twice the bare cavity resonance frequency, Fig. 4.6b. The region of gain deviates from the parabolic region predicted by Eq. 4.13, however. This deviation is understood to result from higher order nonlinearities in the cavity equations of motion, which can occur when pumping at high enough amplitudes such that the cavity resonance frequency is no longer modulated linearly with flux [85]. This effect can lower the steady state photon number from that predicted by Eq. 4.13 [116].

4.4.3 Reset and stability

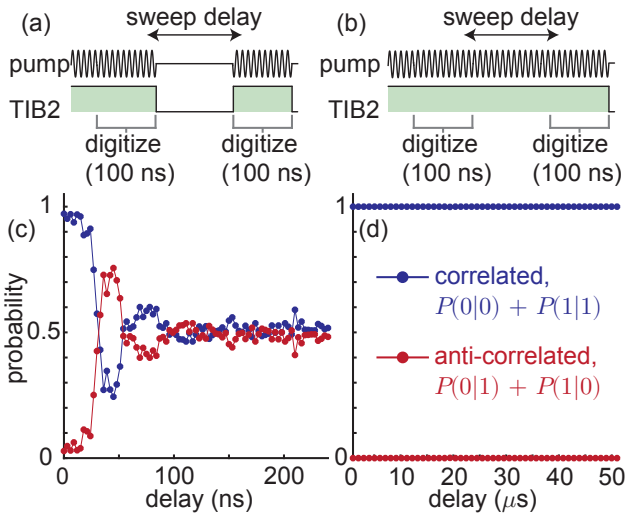

Figure 4.7: **Bifurcation reset and stability.** The bifurcated state of the pumped parametric cavity is measured twice, with a variable delay between measurements. Here, the measurements of '0' and '1' correspond solely to the state of the pumped parametric cavity, with TIB1 set to reflect mode for the entire sequence. (a) During the delay, the pump is turned off and TIB2 is set to reflect mode. (b) During the delay, the pump remains on and TIB2 remains in transmit mode. (c) When the pump is turned off, the second measurement quickly becomes uncorrelated with the first. (d) When the pump remains on, however, the state in the cavity remains exceedingly stable. Data points in both plots are the mean of 1024 single-shot measurements.

We also characterize the stability and reset time of the bifurcated state at the operating point

used in qubit readout in Ref. [23]. Ideally, the pumped state in the bifurcation amplifier should be stable while pumped, and quickly decay when the pump is turned off. These qualities are tested by the measurements shown in Fig. 4.7. While TIB2 is set to transmit mode, the parametric cavity is pumped so that it latches into one of its two bistable states. While doing so, the state in the parametric cavity is digitized over two 100 ns intervals (the same duration used in our readout scheme). These intervals are separated by a delay in which the JPA pump is turned off and TIB2 is set to reflect mode. When sweeping this delay, the second measurement is initially highly correlated with the first. This indicates that the bistable state of the first measurement has yet to dissipate and is seeding the second measurement. After approximately 100 ns without pumping, however, correlation between the first and second measurements has nearly vanished, indicating that the pumped state in the JPA has decayed to near-vacuum. When the pump and TIB state are not changed during the variable delay however, the bifurcated state is extremely stable: the two measurements are greater than 99.9% correlated for any delay between them, with a maximum measured delay of 50 μs.

Chapter 5

Superconducting switches

5.1 Review of current technologies

Over the past two decades, superconducting microwave circuits have emerged as a promising platform for quantum information technology. This has catalyzed recent interest in superconducting switch/coupler technologies. Different types of couplers have already been used to entangle adjacent qubits [121], entangle spatially distant qubits [122] and for qubit readout [23], for example. The two qubit gates in Google's recent demonstration of 'quantum supremacy' [20] are a particular style of coupler designed to carry out fast, high-fidelity gates between adjacent qubits. Other couplers [79, 123, 124] are instead designed to operate as more general purpose switches, for example engineered to connect to a 50 Ohm transmission line on each port. As the field of superconducting quantum information continues to grow, so will the need for switches/couplers or all types.

A selection of recently demonstrated cryogenic, microwave switches is reviewed in Table 5.1.[1] Many of the devices in Table 5.1 achieve a tunable coupling by changing the inductance of a Josephson junction or SQUID. On/off ratios of 50 dB or more have been demonstrated [23], with a greater than 40 dB on/off ratio over several GHz of instantaneous bandwidth [124] and nanosecond switching speeds. Finally, the devices in Table 5.1 have power handling of better than -100 dBm, high enough to be integrated with a Josephson parametric amplifier operated in the high gain limit.

[1] Note that there are many superconducting switches/couplers not listed in this Table 5.1. For example, Refs. [125, 122, 126, 127, 128, 124] make use of superconducting couplers of a similar style to those in Refs. [121, 129, 130]. The couplers in these works are used in conjunction with qubits on the same chip, rather than designed as stand alone switches. Finally, tunable coupling can also be obtained without any explicit switch or coupler device, for example via a parametric interaction (Sec. 2.1.7) as in Refs. [131, 132, 74, 133] and many others.

Table 5.1: **Review of cryogenic switches.** A selection of recent cryogenic switches which have been characterized at microwave frequencies. The values reported from each reference are generally approximate, and whose precise definitions may differ across references. In the 'Technology' column, 'JJ' refers to Josephson-junction based superconducting switches, 'KI' to kinetic-inductance based switches, and 'Comm.' refers to commercial, mechanically actuated switches. Dissipation per switching event is not characterized in most Josephson junction based devices, but is expected to be negligible.

Reference	Tech.	On/off ratio	Bandwidth	Speed	Power dissipated	Power limit
Rosenthal *et al.* (2021), [23]	JJ	50 dB	4-7 GHz	15 ns	N/A[a]	-98 dBm
Chang *et al.* (2020), [124]	JJ	40 dB	4-8 GHz	10 ns	N/A	-83 dBm
Pechal *et al.* (2016), [134]	JJ	30 dB	7.1-7.3 GHz	7 ns	N/A	-90 dBm
Chapman *et al.* (2016), [79, 135]	JJ	40 dB	4-8 GHz	15 ns	N/A	-85 dBm
Naaman *et al.* (2016), [123, 136]	JJ	20 dB	9-11 GHz	20 ns	N/A	-100 dBm
Wagner *et al.* (2019), [137]	KI	10 dB	2-8 GHz	0.4 ns	200 nW	N/A
Potocnik *et al.* (2020), [138]	CMOS	35 dB	0-10 GHz	1 ns	36 μW	N/A
Radiall: #R583423141 (2018)	Comm	60 dB	0-18 GHz	25 ms	200 mW	+50 dBm

[a] Ref. [23] reports 0.05 photons of excess backaction on a qubit due to a switching event.

The Josephson-juntion based superconducting switches in Table 5.1 can also be understood in comparison to other cryogenic switch technologies.

Commercial cryogenic switches, for example part number 'R583423141' from Radiall, have greater bandwidth, higher on/off ratios and higher power handling than other cryogenic switches have been demonstrated to-date. However, commercial cryogenic switches work using the reconfigurable position of a mechanical component, whose switching mechanism is actuated by a large applied current. The switching speed is far slower (25 ms) than the nanosecond time-scales required in superconducting qubit experiments. Switching also heats up the base temperature of a cryostat due to the large required current (e.g. 62.5 mA specified at room temperature). Finally, commercial cryogenic switches are bulky, non-superconducting and lossy.

Another class of cryogenic microwave switches are chip-scale CMOS technologies [139, 140, 138]. These switches overcome the bulkiness problem and can have favorable bandwidth compared to superconducting switches [138]. However, they also dissipate heat when switching although

far less than commercial switches. For example, the multiplexer in Ref. [138] dissipates 36 μW when operating, raising the cryostat base temperature from 10 mK to 32 mK. Additionally, such switches are not superconducting and so have more significant internal loss than Josephson-junction based alternatives. Cryogenic CMOS technologies are arguably an excellent candidate for analog signal processing within a cryostat, but have yet to be demonstrated to be closely integrable with high-performance superconducting qubits.

Finally, superconducting switches may also be built based in the high kinetic inductance of superconducting nanowires [137, 141]. Such switches have relatively high power handling (approximately -60 dBm), but have not yet demonstrated on/off ratios as high as the Josephson-junction based technologies in Table 5.1.

In conclusion, Josephson-junction based superconducting switches are currently a favorable choice for the sensitive signal routing of single-photon level microwave photons at millikelvin temperatures. These switches are especially useful for integration with superconducting qubits, as they can have high on/off ratios with low loss and low power dissipated when switching.

5.2 Tunable inductor bridge design

The work in this thesis relies heavily on 'tunable inductor bridge' (TIB) style superconducting couplers. The TIB design was introduced in 2016 in Ref. [79] and improved for the work in Ref. [23]. The TIB itself is a Wheatstone bridge of tunable inductors realized with SQUID arrays, and draws inspiration from microwave mixers [34] and the Josephson ring modulator [30, 142]. This section describes the TIB design and then performance.

5.2.1 Lumped-element schematic

Central to the TIB is a Wheatstone bridge of tunable inductors, realized with SQUID arrays. Conceptually, the TIB can be thought of as a superconducting analog to a microwave mixer, with diodes replaced by SQUID arrays. As with a mixer, the TIB functions as a microwave switching/modulation element where symmetry of a Wheatstone bridge allows for high-performance,

broadband operation. In particular, the process of preserving vs. breaking the symmetry of the bridge allows for transmission through the TIB to be tuned by a far greater ratio than its constituent inductors can be tuned.

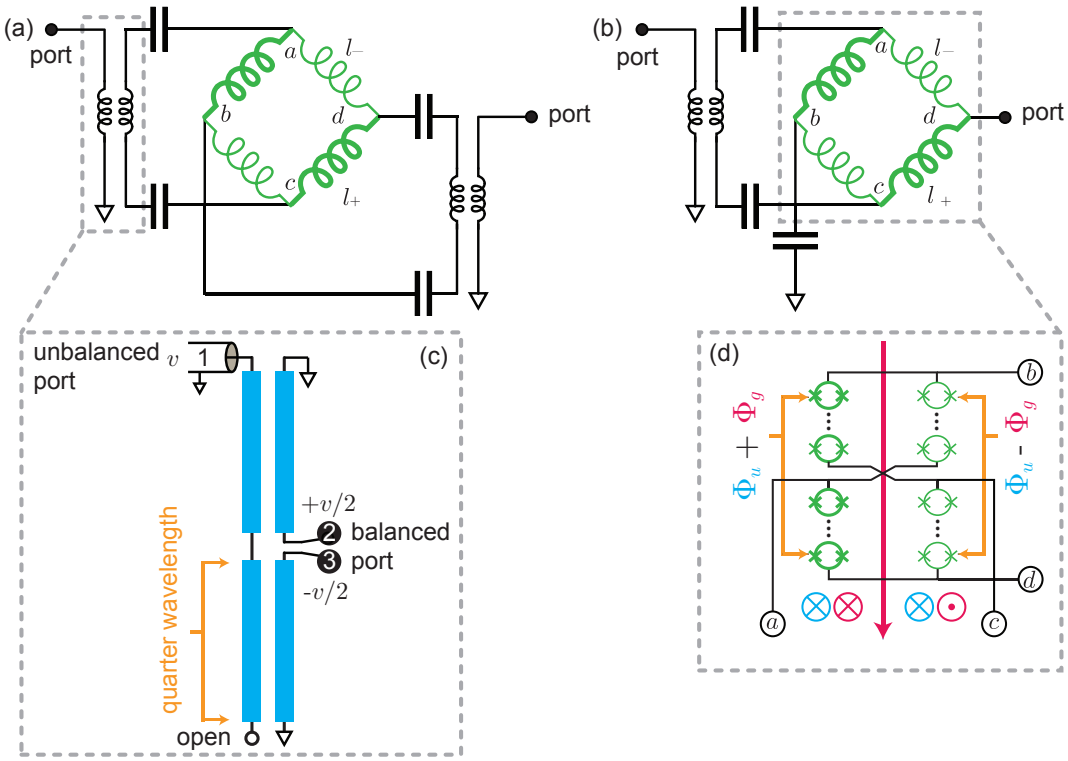

Figure 5.1: **TIB lumped-element schematic.** A tunable inductor bridge (TIB) style superconducting switch is formed from a Wheatstone bridge of SQUID arrays. Ports can be connected to this bridge by either (a) coupling to the differential mode across the north-south nodes (labelled 'a' and 'c') *and* east-west nodes (labelled 'b' and 'd'), as in the device in Refs. [79, 135]. Or (b), by coupling to one opposing pair of nodes deferentially and another node in a single-ended way, as in the device in Ref. [23]. (c) Differential coupling can be achieved with a Marchand balun [143] which consists of a half-wave resonator coupled to two quarter-wave resonators, for a wavelength at the design center frequency (approximately 6 GHz in Refs. [79, 135, 23]). Assuming ideal performance, a signal of amplitude v at the node labelled '1' (the 'unbalanced' port) will cause a response of amplitudes $\pm v/2$ at the nodes labelled '2' and '3'. The differential mode across these ports is the 'balanced' port. (d) The Wheatstone bridge is constructed by twisting the SQUID arrays into a figure-eight geometry. The flux through the SQUID arrays is a combination of a background, uniform flux Φ_u, and a gradiometric flux Φ_g. The gradiometric flux is controlled by the current in a bias line running through the center of the figure-eight (pink arrow). The uniform flux can be controlled by an off-chip superconducting coil, and/or an on-chip bias line threading around the outside of the figure-eight (not drawn).

A lumped-element schematic of a TIB is shown in Fig. 5.1. A Marchand balun (explained in Fig. 5.1c and a simulation shown in Fig. 5.2a) couples the left port of the TIB to the differential voltage across the top and bottom nodes of the bridge (nodes labelled 'a' and 'c' in Fig. 5.1a,b). No signal can couple between the two ports when the bridge is balanced, meaning that all four bridge inductors have equal value. To see this, consider an oscillating signal of amplitude v applied at the left port of the lumped-element circuit in Fig. 5.1a,b. Voltage at the top and bottom nodes of the bridge (labelled 'b' and 'd') will oscillate with amplitude $\pm v'$, respectively, creating an effective ground at the right port and therefore the TIB will reflect (the amplitude $v' \leq |v|/2$ will in general depend on the operating frequency, choice of capacitors, etc). If instead the bridge is imbalanced, as drawn, the symmetry of the bridge is broken so that the right port does *not* see an effective ground, and thus transmission can be nonzero and in fact near unity. Capacitors are added to match the circuit over a desired frequency range.

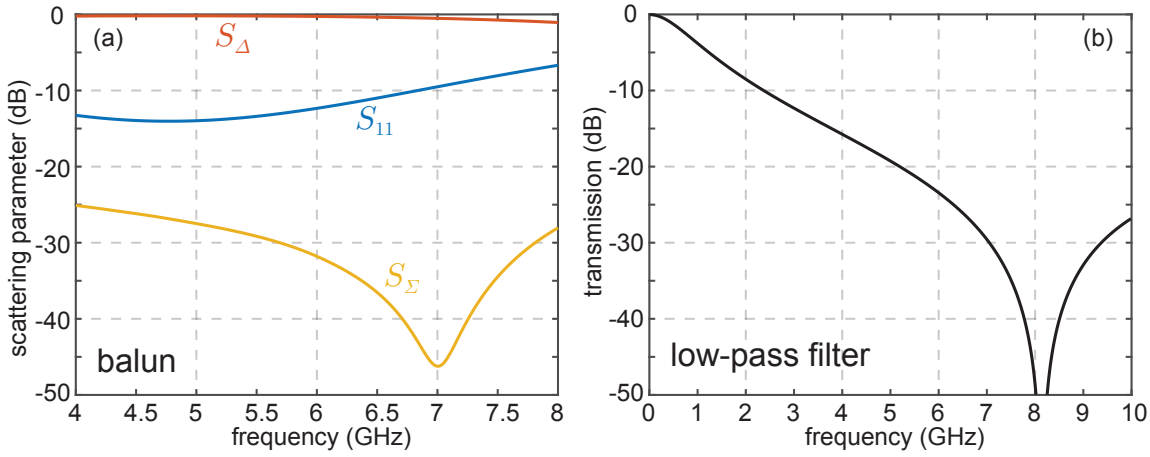

Figure 5.2: **Balun and low-pass filter simulation.** (a) Simulated scattering parameters of the Marchand balun shown in Fig. 5.3. S_{11} is reflection off of the unbalanced port of the balun (labelled '1' in Fig. 5.1c). $S_\Delta = (S_{21} - S_{31})/\sqrt{2}$ is the differential mode transmission coefficient, referring to the balanced port of the balun labelled in Fig. 5.1c), and $S_\Sigma = (S_{21} + S_{31})/\sqrt{2}$ is the common mode transmission coefficient. Transmission through the differential mode is near unity within the design bandwidth of between 4 GHz and 7 GHz. (b) Simulated trasmission through the gradiometric bias line low-pass filter (LPF) shown in Fig. 5.3, with a 50 Ohm port placed on each side of the filter. Transmission goes to unity as frequency approaches zero, allowing the < 350 MHz frequency components of the TIB bias signal in Ref. [23] to pass uninhibited. Transmission drops below -20 dB above 4 GHz. The filter's self-resonance frequency is approximately 8 GHz.

5.2.2 Layout

When constructing a TIB, it is essential to preserve the symmetry of the Wheatstone bridge while still being able to balance or imbalance it. To do so, it is expedient to twist the bridge a figure-eight geometry, and tune the balance or imbalance with a single on-chip bias line running through the center of the bridge, (pink arrow, Fig. 5.1d). This bias line a gradiometric flux $\pm\Phi_g$ into the SQUID arrays on opposite sides of the bridge. At the same time, all the arrays see an identical uniform background flux Φ_u. The inductance l_+ and l_- of the thick and thin inductors in Fig. 5.1 becomes [79],

$$l_{+/-} = \frac{l_0}{\left|\cos\left(\frac{\Phi_u \pm \Phi_g}{2\phi_0}\right)\right|}. \tag{5.1}$$

Where $\phi_0 = \hbar/2e$ is the reduced magnetic flux quantum, with e the charge of an electron. The inductance $l_0 = N\phi_0/2I_c$ is determined by the Josephson junctions critical currents. In Ref. [23], $I_c = 5\,\mu$A and the number of SQUIDs per array is $N = 20$, so that $l_0 = 0.66\,$nH. As long as $\Phi_u/2\phi_0$ is not a multiple of $\pi/2$, applying a nonzero Φ_g will imbalance the bridge such that $l_+ \neq l_-$ and transmission will be nonzero. The greatest imbalance is achieved when $\Phi_g/2\phi_0 = \pi/4$ and $\Phi_u/2\phi_0 = \pi/4 + n\pi$, where n is an integer.

A false-color optical micrograph of a TIB is shown in Fig. 5.3. Its bias lines (for a gradiometric flux, red, and uniform flux, blue, Fig. 5.3a) contain low-pass filters (LPFs), realized with $\sim 20\,$nH spiral inductors. These filters limits microwave power coupling out of the bias line. A numerical finite-element simulation, Fig. 5.2b, indicates that this inductor has a self-resonance frequency of approximately 8 GHz (note that in this style of inductive filter, a higher inductance will generally lead to a lower self-resonance frequency). Further simulations indicate that transmission from a microwave port of the TIB out a bias port is generally smaller than $-40\,$dB between 4 and 8 GHz with inclusion of this LPF, but as high as $-20\,$dB without it. At the operational frequency of 6.34 GHz, transmission from a microwave port of a TIB out of its gradiometric bias port is simulated to be between $-39\,$dB and $-47\,$dB (the exact value changes slightly depending on which of the two microwave ports is used, and whether the TIB is in transmit or reflect mode).

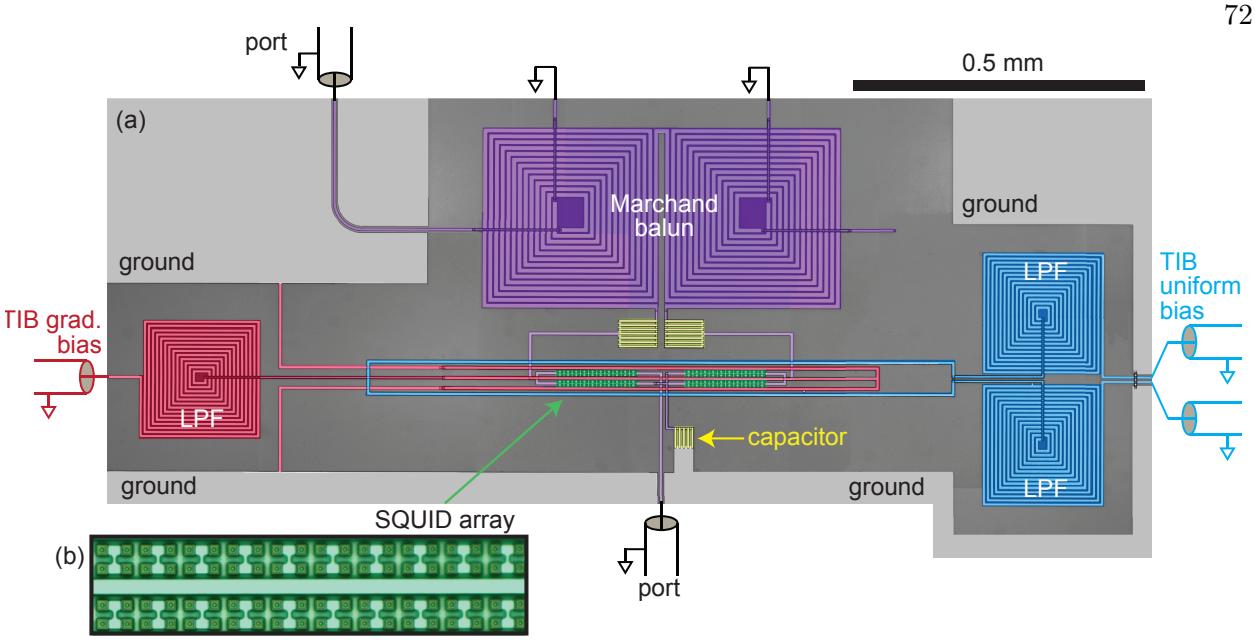

Figure 5.3: **TIB optical micrograph.** (a) False-color optical micrograph of a TIB integrated within the SIMBA used in Ref. [23], following the lumped-element schematic in Fig. 5.1b. The Wheatstone bridge (green, center of the image) is connected to capacitors (yellow), and on one side a Marchand balun (purple). The balance or imbalance of the bridge is controlled with a single bias line (red, coming from the left) which applies a gradiometric flux. A uniform flux is applied from a second bias line (blue, from the right). Both bias lines contain low-pass filters (LPFs) which prevent microwave signal in the TIB from leaking out of these lines. (b) Zoomed-in image of one of the SQUID arrays.

5.3 Performance

Performance of the TIB used in Ref. [23] is shown in Fig. 5.4. Transmission through a single TIB is measured while sweeping the gradiometric bias flux Φ_g. Near $\Phi_g = 0$ the TIB is in 'reflect mode', meaning transmission is near zero. When changing to $\Phi_g \neq 0$, the Wheatstone bridge becomes imbalanced and the TIB is changed to a 'transmit mode'. Transmission is shown in Fig. 5.4c for both an example transmit mode and an example reflect mode, corresponding to horizontal linecuts of the data in Fig. 5.4b, at the gradiometric flux bias specified by the black arrows. By changing Φ_g, the on/off ratio can be tuned to greater than approximately 50 dB at any frequency between 4 and 7.3 GHz.

The bandwidth of the TIB is set by the octave bandwidth of its Marchand balun, here de-

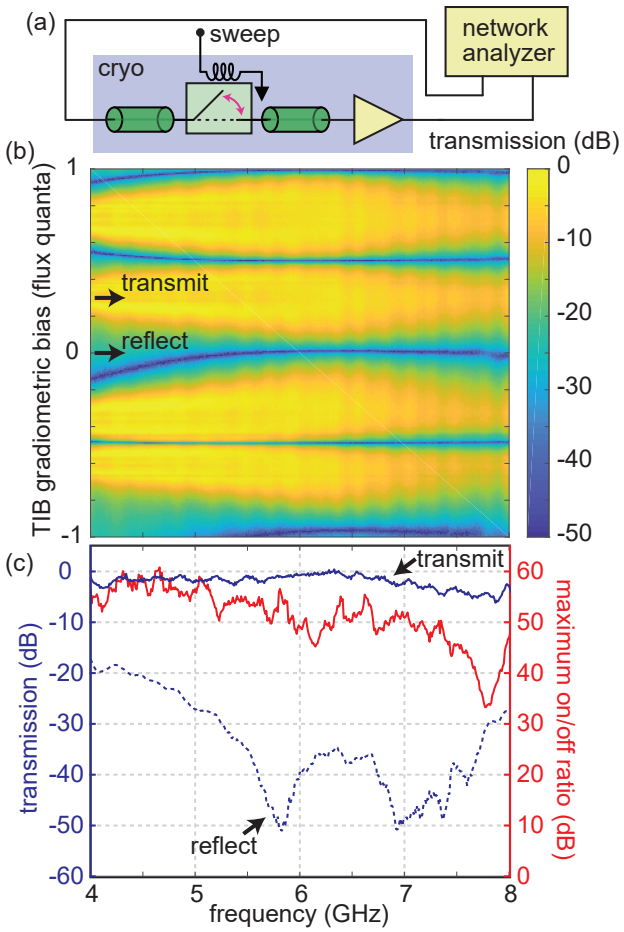

Figure 5.4: **TIB transmission characterization.** (a) A single TIB is measured in transmission while sweeping its gradiometric flux bias, Φ_g. (b) Measurement of transmission vs. Φ_g and frequency. Transmission is normalized to the maximum overall transmission. (c) Transmission vs. frequency at an example transmit mode ($\Phi_g \sim \pi/4$) and reflect mode ($\Phi_g \sim 0$), for uniform flux $\Phi_u \sim \pi/8$. At the reflect mode, transmission is lower than -30 dB over several GHz. The maximum on/off ratio that can be achieved at any given frequency is plotted in red, and is better than 50 dB between 4 to 7.3 GHz. The reflect mode data and on/off ratio are smoothed with a 100 MHz moving filter.

signed to have a center frequency near 6 GHz. Bandwidth is also affected by the maximum bridge imbalances, $l_+/l_- \sim 4$ [79, 135, 61].[2] In general, a higher maximum imbalance improves bandwidth.[3] The bandwidth and center frequency are also affected by choice of matching capacitors, here $\sim 0.5\,\mathrm{pF}$.

[2] The maximum possible bridge imbalance is set by the SQUID array geometry, geometric inductance, and asymmetry of the Josephson junctions [83].

[3] This can be understood as a consequence of the Bode-Fano criteria (Chp. 5.9 of Ref. [34]).

Note that the TIB in Ref. [23] has a reported power handling of approximately -98 dBm along with an approximately 15 ns swithing speed, comparable to previously demonstrated TIBs [79, 135]. See Fig. 5.5 for additional measurements of the TIB power handling and switching speed.

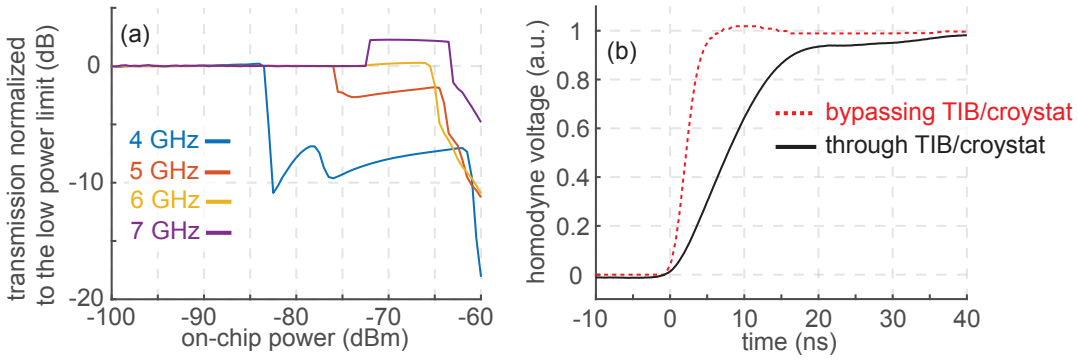

Figure 5.5: **TIB power handling and switching speed characterization.** (a) Power handling: Transmission through a TIB set to transmit mode, as a function of estimated on-chip power. Transmission at each frequency is normalized to unity in the low power limit, but in general is less than unity due to reflections from the device. (Note that the rise in transmission at 7 GHz likely does not represent gain, but instead reflection diminishing in magnitude.) The onset of nonlinearity is observed between -84 dBm at 4 GHz and -73 dBm at 7 GHz. Note that this is higher than the -98 dBm reported in Ref. [23]. (b) Switching speed: a square wave pulse (generated at 1.2 Gs/s) is applied to the TIB gradiometric bias line. Transmission at 6 GHz is measured through the TIB (black, solid line), using a homodyne measurement, and is compared to the same square wave measured directly (red, dashed line). A 350 MHz low-pass filter is placed on the TIB bias line (black line, only), limiting the switching speed. Note that (b) was taken with a slightly difference device/design than used in Ref. [23].

5.4 Switch networks

TIBs can also be combined into networks with more complicated connectivity for example a 2x1-TIB (a single-pull double-throw 'SPDT' geometry). To construct a 2x1-TIB, two 1x1-TIBs are combined on-chip with a T-junction as in Fig. 5.6 and Ref. [124].

In order for the network to be matched when one TIB is set to reflect mode, the phase of the signal reflected from a TIB must be taken into consideration. Transmission through the network will always be zero if reflection from one or both TIBs look like a short at the reference plane of the T-junction. To engineer a TIB in reflect mode to instead look like an open at this reference plane,

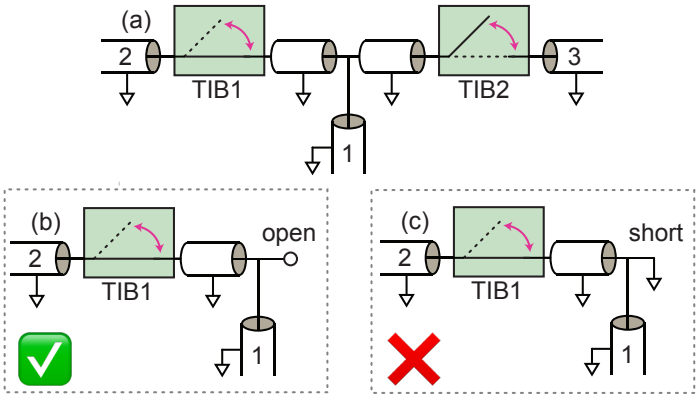

Figure 5.6: **TIB network.** (a) A three-port switch network can be constructed using two-TIBs connected by a T-junction. Depending on the bias of the TIBs, a signal incident on port-1 can be routed either to port-2, port-3 or reflected. Appropriate electrical length can be placed between the TIBs so that a TIB in reflect mode reflects close to an open at the reference plane of the T-junction, at the design frequency, as illustrated in (b). If instead a TIB in reflect mode looks like a short at the reference plane of the T-junction (c), a signal incident on port-1 will be reflected even when the other TIB is set to transmit mode.

appropriate electrical length can be added between the TIBs and the T-junction between them. In general, the amount of electrical length required will depend on the specific properties of the TIBs in the network and the design frequency.

This example can be extended to create larger switch networks. To do so and maintain high performance, it is crucial to understand the scattering parameters of the individual TIBs both when in transmit mode and in reflect mode. Constructing an N×M or even N×1 network of superconducting switches, where $N \gg 1$ and/or $M \gg 1$, remains an outstanding challenge. Doing so while maintaining high-quality performance and ease of calibration would have general use within large scale superconducting qubit systems.

Chapter 6

The SIMBA

The SIMBA ('Superconducting Isolating Modular Bifurcation Amplifier') is a 2-port parametric amplifier with a tunable external coupling on each port, Fig. 6.1. The SIMBA is designed for superconducting qubit readout, Fig. 6.2. As in conventional dispersive readout [15], a pulse is first sent into the weakly coupled port of a two-port readout cavity, where it acquires a qubit state-dependent phase shift. TIB1 is then set to transmit mode for a duration chosen to fully swap this pulse into the parametric cavity, which has previously been tuned near resonance. Next, the field inside the parametric cavity is amplified by parametric modulation at twice the resonance frequency, Sec. 2.1.4. In this work, we choose to pump the parametric cavity into the bistable regime [85, 116]: a non-unitary process in which the cavity latches into one of two bistable states with opposite phase but large, equal amplitudes, Sec. 4.3. Readout is achieved by seeding the parametric cavity state with the probe tone, such that the post-measurement qubit state is correlated with the latched state of the parametric cavity [144, 119]. To learn the measurement result outside of the cryostat, TIB2 is set to transmit mode, coupling the amplified state to a standard cryogenic microwave measurement chain.

6.1 Calibration

The following steps are required to calibrate superconducting qubit readout using a SIMBA:

(1) Tune the JPA frequency to the readout cavity frequency, Fig. 6.3a.

(2) Sweep the JPA pump amplitude/frequency to give desired gain/bifurcation, Fig. 4.6.

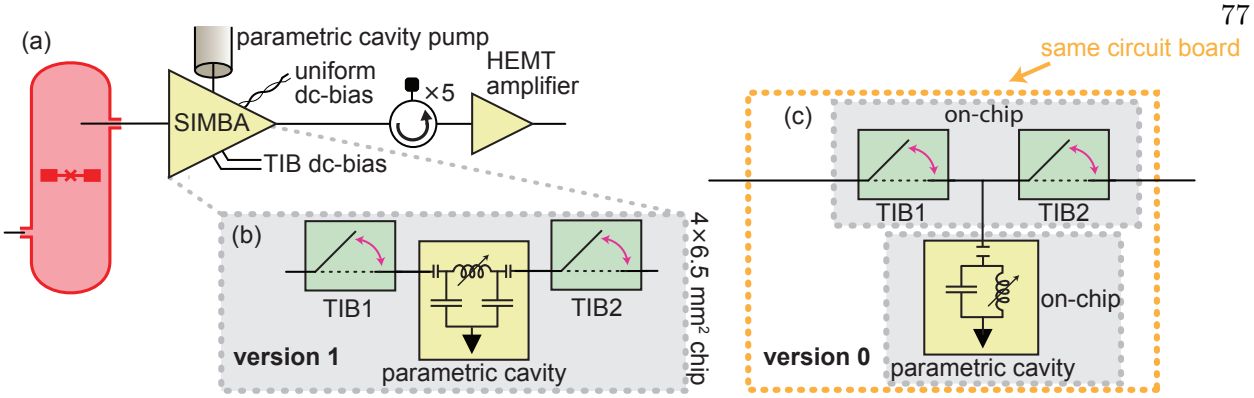

Figure 6.1: **Introduction to the SIMBA**. (a) A transmon qubit in a 3-dimensional readout cavity is measured using a SIMBA ('Superconducting Isolating Modular Bifurcation Amplifier'). (b) The SIMBA is comprised of a two-port parametric cavity with a tunable-inductor-bridge (TIB) style coupler on each port. In this thesis, 'version-1' refers to the device in Ref. [23], which is constructed on one chip using the illustrated geometry. (c) In a preliminary demonstration 'version-0', the SIMBA is constructed using a 1-port resonator combined with a network of TIBs connected to a T-junction, as in Sec. 5.4.

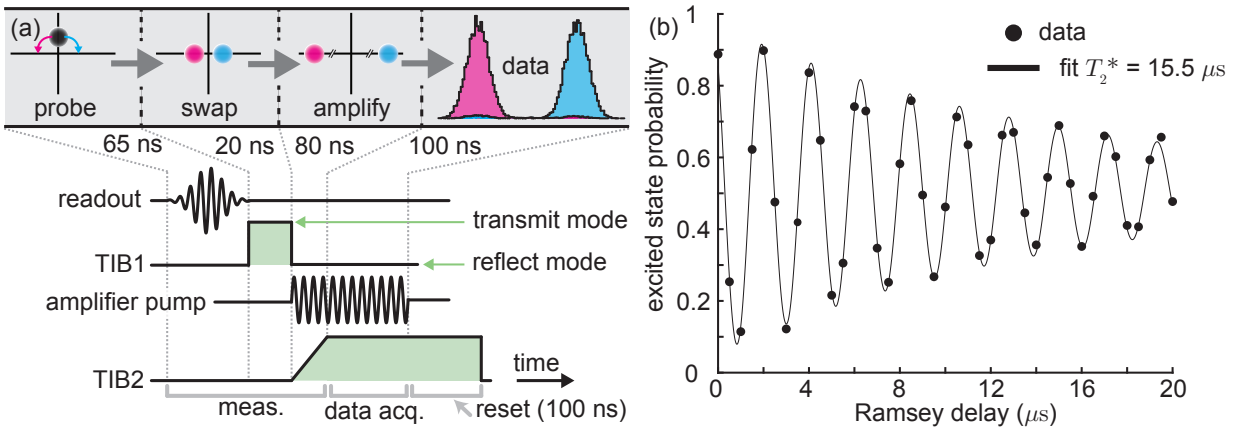

Figure 6.2: **Qubit measurement using a SIMBA**. (a) A probe tone is sent into the readout cavity, swapped into the parametric cavity, and then amplified. The amplified state is then coupled to a standard cryogenic measurement chain and digitized. Cyan (pink) histograms correspond to single-shot measurements when the qubit has been prepared in the ground (excited) state. (b) Example measurement of a transmon qubit's coherence time using a version-1 SIMBA. Two $\pi/2$ pulse are separated by a variable 'Ramsey' delay (the x-axis) and then the qubit is projectively measured using the sequence in (a). Contrast of the measured excited state probability is limited primarily by state preparation errors, in particular the $\pi/2$ pulses not being precisely calibrated in this example.

(3) Choose the readout pulse amplitude/frequency. Specify the readout pulse phase compared

to the JPA pump tone.

(4) Sweep the duration for which TIB1 is set to transmit mode, Fig. 6.3b. Choose the minimum duration which maximizes readout fidelity.

(5) Fine-tune TIB reflect modes to minimize backaction (Fig. 6.4) and maximize the measurement efficiency and readout fidelity (Fig. 6.7c).

The first three steps are generally true of any readout scheme which uses a tunable, narrow band and phase-sensitive parametric amplifier. The final two steps are specific to the SIMBA. From knowledge of the qubit, SIMBA and measurement setup, the parameters in all steps may be reasonably estimated so that near-optimal readout can be calibrated quickly.

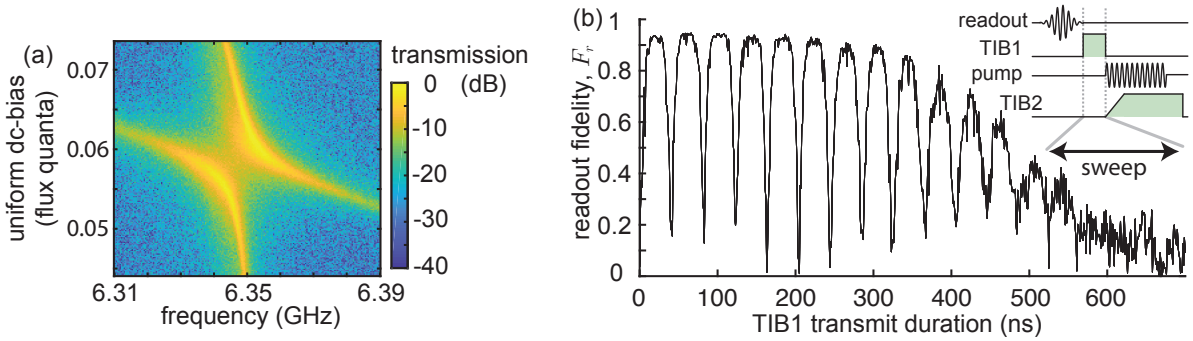

Figure 6.3: **Swap calibration** (using a version-1 SIMBA). (a) A uniform background magnetic flux is swept while probing the readout cavity in transmission with both TIBs in transmit mode. The avoided crossing shows the parametric cavity tuning through the readout cavity. To operate a SIMBA, this uniform flux bias is set so that the readout and parametric cavities are minimally detuned. (b) Readout fidelity F_r (the ability of a measurement to distinguish the qubit eigenstate, [108]), is plotted vs. the duration for which TIB1 is set to transmit mode within the measurement sequence. Oscillations with a period of 40 ns indicate coherent swapping of a readout pulse between the readout and parametric cavities.

6.2 Characterization

6.2.1 Metrics of performance

Important metrics to describe superconducting qubit readout are summarized in Table 6.2.1. These metrics include: excess backaction n_b, the number of readout photons a qubit is exposed

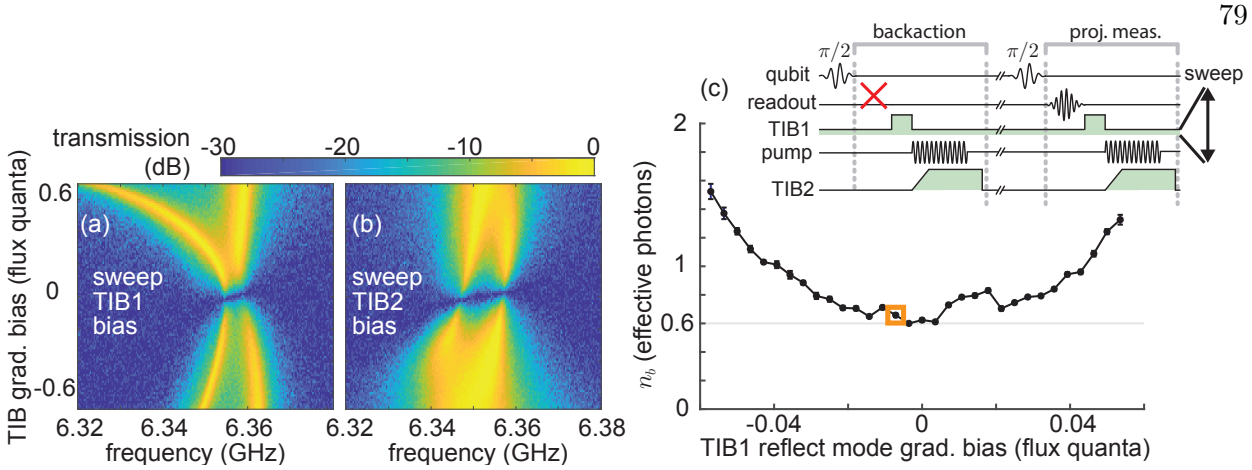

Figure 6.4: **TIB refect mode calibration** (using a version-1 SIMBA). Transmission through the readout cavity when the gradiometric bias on (a) TIB1 and (b) TIB2 is swept with the gradiometric bias on the other TIB set to ~ 0.3. The JPA is tuned near resonance with the readout cavity in both cases. The presence of a reflect mode (transmission $<$ -30 dB in this measurement) is seen by the null in transmission near zero gradiometric bias. (c) Excess backaction n_b is measured by inserting a measurement sequence with zero readout amplitude into a Ramsey sequence, as in Fig. 3. Excess backaction is measured as a function of the gradiometric bias on TIB1, swept near reflect mode. The gold square indicates the operating point used to calibrate the measurement efficiency, for the data shown in Fig. 6.7.

to from detector backaction, the measurement efficiency η which quantifies the overall loss and added noise in a detector, and the maximum readout fidelity F_0 which quantifies how well the qubit state can be discriminated. To characterize n_b and η we use the framework of measurement-induced dephasing [24], which is reviewed in Chp. 3. Important for quantum error correction is how rapidly the measurement and digitization is completed, and also how quantum non-demolition (QND) a measurement is, meaning to what degree the qubit's post-measurement state is correlated with the measurement result [145, 72]. Finally, considerations such as ease of calibration and number/bandwidth of bias tones are also important when trying to scale any measurement scheme.

6.2.2 Version-0

First, we present data from a 'version-0' demonstration of the SIMBA (Fig. 6.1c), preliminary to the 'version-1' device and experiment in Ref. [23]. In version-0, measurement efficiency and readout fidelity were lower than in version-1, and calibration was complicated by issues with trapped

Table 6.1: **Qubit readout performance metrics.**

Metric	Description	Relevant formula	More information
F_r	readout fidelity	$1 - P(e\|0) - P(g\|\pi)$	Ref. [108]
F_0	maximum readout fidelity	$F_0\text{erf}\left[\sqrt{2\eta n_r}\right] = F_0\text{erf}\left[\nu\epsilon\right]$	Sec. 3.3.3
$\|\hat{\rho}'_{01}\|$	post-measurement coherence	$\rho_b e^{-2(\sqrt{n_r})^2} = \rho_b e^{-\epsilon^2/2\sigma^2}$	Sec. 3.2
n_r	readout photons (effective)[a]	$\|\alpha\|^2 \sin^2\theta$	Sec. 3.2
n_b	excess backaction photons (effective)	$-\log\left(2\rho_b\right)/2$	Sec. 3.2
η	measurement efficiency	$2\sigma^2\nu^2$	Sec. 3.3
F_{QND}	quantum non-demolition fidelity	$\frac{1}{2}\left[P(e_2\|e_1) + P(g_2\|g_1)\right]$	Refs. [145, 72]

[a] 'Effective' photon numbers n_r and n_b refer to the photon number of a coherent state scaled by $\sin^2\theta$, where $\theta = \arctan\left(2\chi/\kappa_r\right)$ describes the angle of the coherent state in phase space, defined as in Fig. 3.1.

flux in the parametric cavity. However, excess backaction was significantly lower than in version-1, excess backaction due to TIB switching was negligible, and quantum non-demolition fidelity was near unity and limited by the qubit's T_1 time. The performance of version-0 serves as a proof-of-principle demonstration for some of the metrics which can be improved upon in version-1.

Excess backaction due to TIB switching is characterized in Fig. 6.5a,b. The qubit's energy relaxation and coherence times are measured while TIB1 is square-wave modulated between transmit and reflect mode. (In the example in Fig. 6.5b, the coherence time is measured using an echo sequence: $\pi/2$ pulse, delay, π pulse, then another delay and $\pi/2$ pulse.) The qubit's T_1 and T_2^{echo} times are not dramatically affected by the square-wave modulation rate up to $\Omega/2\pi$. Measurement of $T_2^{\text{echo}} \sim 4\,\mu$s when square-wave modulating TIB1 at 100 MHz indicates less than $\lesssim 6 \times 10^{-4}$ photons of backaction per switching event.

The isolation provided by TIB1 can also be characterized by measuring the qubit's coherence time while the amplifier pump is turned on during the delay step. (In Fig. 6.5c,d, the coherence time is measured using a Ramsey sequence: $\pi/2$ pulse, delay, then $\pi/2$ pulse.) In the measurement

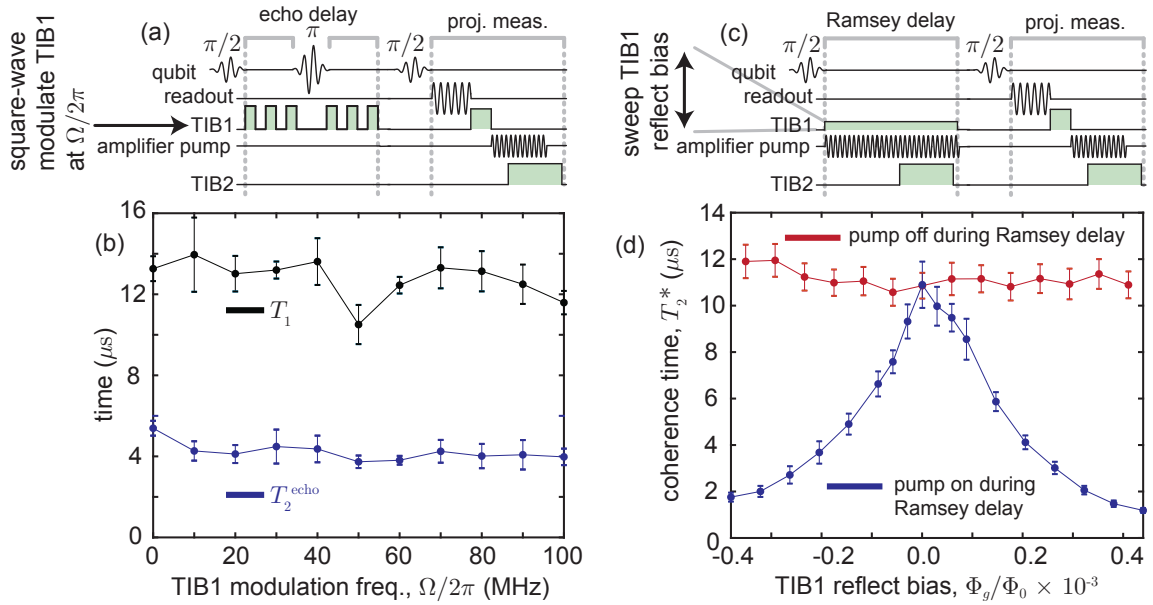

Figure 6.5: **SIMBA backaction, version-0**. (a,b) Measurement of a qubit's energy decay time T_1 and coherence time T_2^{echo} measured with an echo sequence. (Coherence time measured using a Ramsey sequence was less than 1 μs in this experiment.) These measurements are taken while square-wave modulating TIB1 during the Ramsey delay at rate $\Omega/2\pi$. Neither T_1 or T_2^{echo} are dramatically changed by the modulation frequency, bounding any destructive effects due to modulation. See Fig. S15 of Ref. [23] for similar data using SIMBA version-1, where backaction from TIB1 modulation is small per switching event but more noticeable. In both versions, modulating TIB2 had a negligible effect on the coherence time. (c,d) The isolation provided by TIB1 can be measured by pumping the parametric cavity (here at the same pump amplitude as used in a projective measurement) while sweeping the reflect mode bias on TIB1. Away from optimal reflect bias, the qubit is increasingly dephased by pump backaction. At the optimal bias of TIB1's reflect mode, however, the qubit's coherence time of $T_2^* \sim 10$ μs was unaffected by pumping the parametric cavity during the delay. This bounds of $\bar{n}_b \leq 0.03$ steady-state cavity photons due to amplifier backaction. Note than the x-axis value is scaled so that $\Phi_g/\Phi_0 = 0$ corresponds to the calibration of maximum isolation, which is slightly offset from zero bias voltage. See Fig. 6.4c for a similar experiment using version-1. Note that data in (b) and (d) were taken in separate cooldowns, with more careful filtering and radiation shielding in (d), resulting in a longer qubit coherence time.

shown in Fig. 6.5d, when the TIB1 reflect bias is set optimally no difference can be measured between the qubit's ~ 10 μs coherence time when the parametric cavity is pumped during the delay, or not. This places a bound of $\bar{n}_b \lesssim 0.03$ photons in the readout cavity due to pumping the parametric amplifier. In a different data set taken with the same device and qubit, Fig. 6.6, a similar value of $n_b = 0.02$ photons is measured along with efficiency of approximately $\eta = 44\%$ and

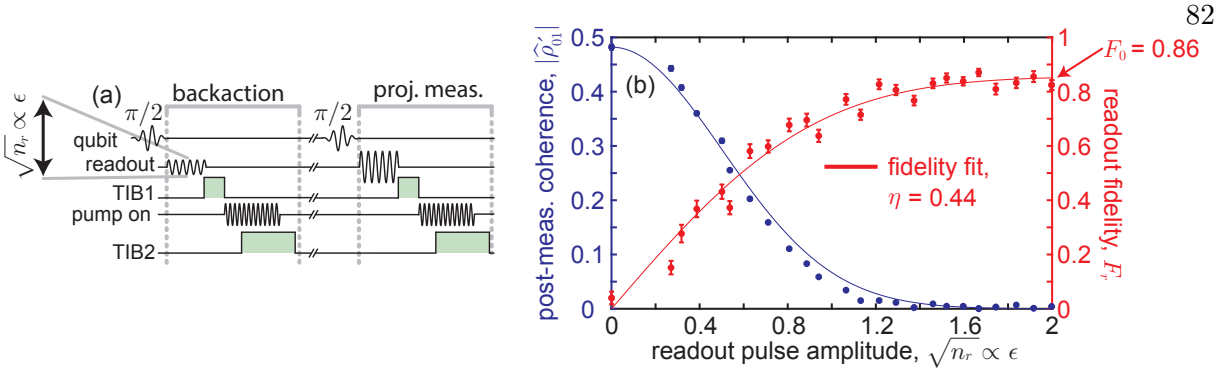

Figure 6.6: **SIMBA efficiency, version-0**. (a) Excess backaction and measurement efficiency are characterized by inserting a variable measurement into a Ramsey sequence, as in Fig. 6.7. (b) Results, with the JPA pump remaining on during the variable strength measurement within the Ramsey sequence. Fitting data to models, Table. 6.2, yields measurement efficiency of approximately $\eta = 0.44$ and maximum readout fidelity $F_0 = 0.86$. For a variable strength measurement of zero readout amplitude ($\sqrt{n_r} = 0$), $\rho_b = 0.482 \pm 0.004$ corresponding to $n_b = 0.018 \pm 0.002$ effective photons of excess backaction.

maximum readout fidelity of approximately $F_0 = 86\%$.

6.2.3 Version-1

In the SIMBA version-1, Ref. [23], we characterize readout to be low-backaction, high fidelity, and high efficiency. Excess backaction is found from $\rho_b = 0.141 \pm 0.002$ (left-most data point, 'pump on' data, Fig. 6.7c, uncertainty represents plus/minus one standard deviation). Using Eq. 3.15, this corresponds to $n_b = 0.63 \pm 0.01$ effective photons of excess backaction; about one quarter of the $n_r^{\text{proj}} = 2.4$ effective photons used in a projective measurement (the maximum value on the x-axis of Fig. 6.7c), and far less than the $\sim$ 150 photons in the pumped state of the parametric cavity (Ref. [23], supplementary material Sec. IV.E). Next, we find ν and the maximum fidelity $F_0 = 95.5\% \pm 0.3\%$ by fitting F_r vs. readout amplitude (red data, Fig. 6.7c) to Eq. 3.26. Finally we obtain σ from a fit of the 'pump off' data (cyan) to Eq. 3.27, and therefore determine $\eta = 70.4\% \pm 0.9\%$ using Eq. 3.28.

This fit excludes the first four data points, which level off more quickly than predicted such that excess backaction includes 0.05 ± 0.01 effective photons caused solely by actuating the TIBs

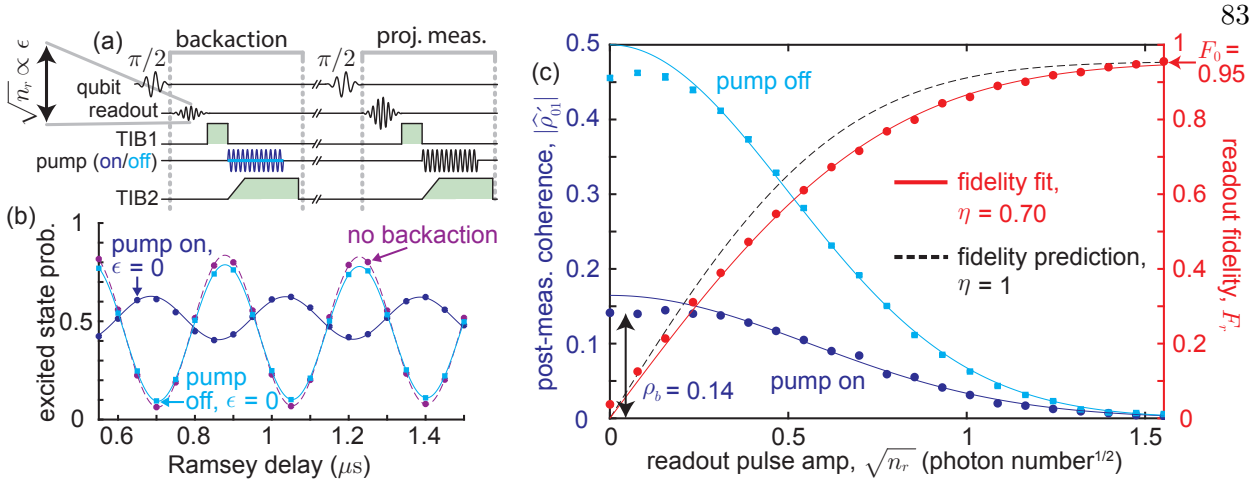

Figure 6.7: **SIMBA characterization, version-1**. (a) Post-measurement qubit coherence $|\hat{\rho}'_{01}|$ is obtained by inserting a variable measurement into a Ramsey sequence, exposing the qubit to backaction. The ratio of the amplitude of the measured Ramsey fringes to the amplitude of those measured without this backaction (nothing inserted into the Ramsey sequence) equals $2|\hat{\rho}'_{01}|$. (b) Excess backaction is determined by inserting a 'measurement' with zero readout amplitude. Post-measurement coherence after excess backaction with the parametric cavity pump on (indigo) and off (cyan), are compared to a case with no backaction (no readout pulse, pump, or TIB switching inserted in the Ramsey sequence, violet). (c) Post-measurement coherence $|\hat{\rho}'_{01}|$ (left y-axis) and readout fidelity F_r (right y-axis, red data points), are measured while sweeping the readout amplitude $\sqrt{n_r}$ of a variable strength measurement. As in (b), $|\hat{\rho}'_{01}|$ is measured both with the parametric pump turned on or off during the variable measurement sequence (indigo or cyan data points, respectively). Post-measurement coherence with the parametric pump turned on, but in the absence of readout photons, is specified by $\rho_b = |\hat{\rho}'_{01}\left(\sqrt{n_r} = 0\right)|$ and determines the excess backaction $n_b = -\log\left(2\rho_b\right)/2$. Measurement efficiency η is determined by a comparison between measurement-induced dephasing and readout fidelity while sweeping readout amplitude.

For $\sqrt{n_r} \gtrsim 0.2$ our models for both $|\hat{\rho}'_{01}|$ and F_r generally fall within the 95% confidence interval of the measurement, and so only these points are used to obtain efficiency. This choice conservatively affects the reported efficiency; including the first four points, or instead fitting the 'pump on' data, returns a larger value for η. We note that in this experiment, η must be limited to 78% or less based on an independent measurement of loss in the parametric cavity and a model for how this loss affects the efficiency (Ref. [23], supplementary material Sec. VI.A). This dephasing process is not captured by our model, and may result from a noise source on the parametric cavity side of TIB1 (Ref. [23], supplementary material Sec. V.B).

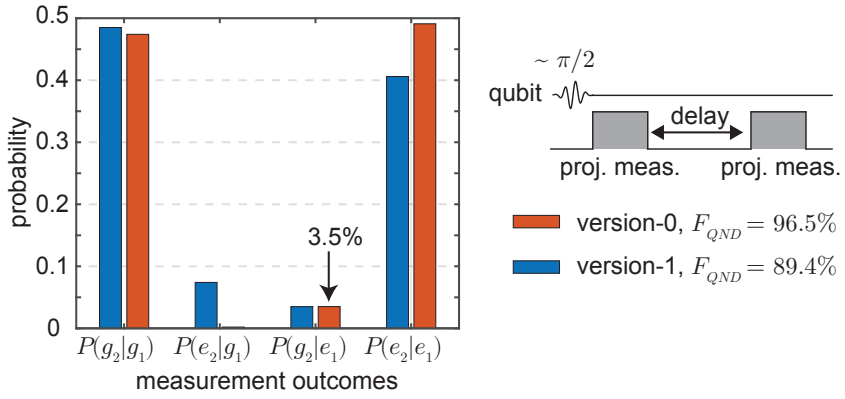

Figure 6.8: **Quantum non-demolition characterization.** A qubit is prepared in a superposition state and projectively measured twice, with a delay between measurements much longer than the SIMBA reset time of 100 ns (Fig. 4.7). Measurement outcomes are far more likely to be correlated than anti-correlated, indicating that the measurement is quantum non-demolition. Red data is from the SIMBA version-0 (Fig. 6.1c), using a delay of 500 ns and a measurement time of 260 ns. Blue data is from the SIMBA version-1 (Fig. 6.1b and Ref. [23]), using a delay of 1 μs and a measurement time of 265 ns. QND-fidelity, Eq. 6.1, is $F_{QND} = 96.5\%$ using version-0 and $F_{QND} = 89.4\%$ using version-1. In version-0, QND-infidelity is dominated by relaxation to the ground state during the delay step, with a probability consistent with the qubit's energy relaxation time of $T_1 \sim 12\,\mu$s.

6.2.4 Quantum non-demolition fidelity

We also characterize the degree to which qubit readout using a SIMBA is quantum non-demolition (QND), meaning that the qubit remains in its measured eigenstate [145, 72]. Low power dispersive readout of superconducting qubits is understood to be QND [15]. To test this using a SIMBA, we prepare the qubit in a superposition state, and then projectively measure it twice with a delay between measurements much longer than the reset time, Fig. 6.8.

QND fidelity is defined as:

$$F_{QND} = \frac{1}{2}\left[P\left(e_2|e_1\right) + P\left(g_2|g_1\right)\right], \tag{6.1}$$

and is diminished by the error probabilities $P(g_2|e_1) = 1 - P(e_2|e_1)$ and $P(e_2|g_1) = 1 - P(g_2|g_1)$ indicating decay from the excited to ground state between measurements, and excitation from the ground to excited state between measurements, respectively. Note that in this definition of QND fidelity taken from Ref. [72], $F_{\mathrm{QND}} = 0.5$ when the results of the two subsequent measurements are

uncorrelated, meaning that measurement outcomes $P(g_2|g_1) = P(g_2|e_1) = P(e_2|g_1) = P(e_2|e_1) = 1/4$ occur with equal probability.

In both experiments shown in Fig. 6.8, probability $P(g_2|e_1)$ of decay from the excited to ground state between measurements is approximately consistent with the qubit's T_1 time and the delay between measurements. The rate of spontaneous excitation from the ground to excited state $P(e_2|g_1)$ may be indicative of a high parametric cavity temperature when the TIBs are disconnected. In version-1, this is potentially related to the dephasing measured when modulating TIB1, (Fig. S15 of Ref. [23]). Note that in Ref. [23], prior to any qubit measurement both TIBs are set to transmit mode for a duration much longer than T_1, as this improved readout fidelity seemingly by reducing the residual qubit excited state population.

6.2.5 Summary of results

Readout performance to-date using a SIMBA is summarized in Table 6.2. In both versions readout is fast, high fidelity and quantum non-demolition. Moreover it is also efficient and low-backaction, indicating that the SIMBA is a successful alternative to using ferrite circulators/isolators before the first amplifier.

Table 6.2: **SIMBA performance summary.**

Parameter	Version-0	Version-1 [23]
Maximum readout fidelity, F_0	86%	95.5%[a]
Excess backaction, n_b	0.02 photons	0.66 photons
Measurement efficiency, η	44%	70.4%
QND-fidelity, F_{QND}	96.5%	89.4%
Measurement time	260 ns	265 ns

[a] Fidelity as high as 97% measured during the same cooldown as Ref. [23], but at a slightly different calibration than in Fig. 6.7 using a higher JPA pump amplitude, leading to greater excess backaction.

In particular, the demonstration in Ref. [23] combines state-of-the-art measurement efficiency *and* considerable isolation from amplifier backaction such that $n_b \sim n_r^{\text{proj}}/4$. The measurement efficiency of previous superconducting qubit readout schemes have been limited to $\eta = 80\%$ [49], and less when providing any isolation before a parametric amplifier [35, 95, 75, 71] (see Table 1.1).

Near-unit measurement efficiency after future improvements would allow for near-*complete* access to the information extracted from a quantum system. Additionally, the SIMBA is chip-scale, compatible with scalable fabrication procedures including the use of through-silicon-vias [146], and requires only one microwave control tone to operate. The SIMBA is therefore a favorable choice for high-quality and scalable superconducting qubit measurement.

6.3 Current limitations

We now discuss the limitations of the qubit readout using the SIMBA version-1 (Fig. 6.1b and Ref. [23]). With reasonable changes to the qubit and SIMBA as outlined in this section, we estimate that it will be straightforward to achieve maximum readout fidelity of $F_0 \geq 99\%$, excess backaction of $n_b \leq 0.02$ photons and efficiency of $\eta > 90\%$, for a measurement and digitization procedure of $\leq 100\,\text{ns}$.

6.3.1 Readout fidelity

Readout infidelity results from a combination of state preparation errors, qubit decay during measurement, and inability of the parametric cavity to correctly latch to the appropriate state. Estimates of these errors are given in Table 6.3, for the characterization in Ref. [23].

Table 6.3: **Sources of readout infidelity.** Estimates for SIMBA version-1, Ref. [23].

Error mechanism	Estimated probability
State preparation	2.3%
Qubit decay before measurement	1.3%[a]
Parametric cavity latching failure	1.1%[b]
Inability to discriminate bifurcated state	$< 0.1\%$

[a] Consistent with a 265 ns readout time and $T_1 \sim 9\,\mu\text{s}$.

[b] Estimated from the difference in $F_0 = 95.5\%$ measured in Ref. [23] compared to the maximum value of $F_0 = 96.8\%$ measured using the same device, during the same cooldown, but with a higher parametric pump amplitude.

Readout fidelity can be improved to near-unity by improving state preparation due to better thermalization, using a qubit with a longer T_1 time, and reducing any latching failure by increasing

the JPA pump amplitude (at the potential cost of greater excess backaction). Readout fidelity has also been shown to be increased by careful shaping of the readout pulse [35], not yet tried using a SIMBA. Readout fidelity of approximately 99.9% in 100 ns is expected given state-of-the-art transmon qubit performance of $T_1 \sim 100\,\mu$s, and a residual thermal photon population of $\bar{n}_{\text{th}} \leq 2 \times 10^{-4}$ as in Ref. [104].

6.3.2 Efficiency

A SIMBA used for qubit readout can be modelled as two cavities connected by a time-dependent coupling $g(t)$. Here, we assume the cavities to each have the degenerate bare resonant frequency ω_0. Inefficiency is caused by loss rates κ_r and κ_p in the readout and parametric cavities, respectively, along with any inefficiency in the amplifier itself. For phase-sensitive gain with no additional added noise, we might expect the measurement efficiency to be approximately: $\eta \sim g_0/\left(g_0 + \kappa_r + \kappa_p\right)$. In Ref. [23], $g_0/2\pi = 12.5\,\text{MHz}$, $\kappa_r/2\pi = 0.44\,\text{MHz}$ and $\kappa_p/2\pi = 4.0\,\text{MHz}$ (see Table 6.4), and such an estimate gives $\eta \sim 0.74$ — close to the measured value of $\eta = 0.70$.

This estimate can be made more precise by numerically solving a classical input-output model for the readout cavity + SIMBA system (see Sections 2.1.6 and 2.3). Consider the classical, time-dependent readout cavity and parametric cavity fields, $A(t)e^{i\omega_0 t}$ and $B(t)e^{i\omega_0 t}$, respectively, which rotate at bare cavity resonance frequency ω_0 (assuming no detuning between the cavities). These cavities are coupled with a time-dependent coupling $g(t)$. Loss in the readout cavity is the sum of an internal loss rate κ_r^{int} along with loss from a weakly coupled port κ_r^w such that $\kappa_r = \kappa_r^{\text{int}} + \kappa_r^w$. Using input-output formalism (Sec. 2.3), this port interacts with an input field $A_I e^{i\omega_0 t}$ and output field $A_O e^{i\omega_0 t}$. In a frame rotating at ω_0, the Heisenberg-Langevin equations of motion for this system simplify to,

$$\sqrt{\kappa_r^w} A = A_I + A_O, \tag{6.2}$$

$$\dot{A} = -\frac{\kappa_r}{2} A + i g(t) B + \sqrt{\kappa_r^w} A_I, \tag{6.3}$$

$$\dot{B} = -\frac{\kappa_p}{2} B + i g(t) A. \tag{6.4}$$

Table 6.4: **Sources of loss.** Estimates of loss in the readout and parametric cavities, from the SIMBA version-1, Ref. [23]. Total loss rates are extracted from measurement. Contributions are approximate and obtained from a combination of measurement, simulation and values reported in the literature. See Table S3 of Ref. [23] for more information.

Mechanism	Readout cavity, $\kappa_r/2\pi$	Parametric cavity, $\kappa_p/2\pi$
Coupling to microwave ports	8 kHz[a]	$\sim$ 2.5 MHz[b]
Internal dissipation	$\sim$ 30 kHz	$\sim$ 1 MHz
Coupling to cable modes	$\sim$ 400 kHz	$\sim$ 400 kHz
Coupling out of bias lines	$<$ 1 kHz	80 kHz
Total loss rate	440 kHz	4.0 MHz

[a] Through a weakly coupled port (in addition to the strongly coupled port connected to the SIMBA).
[b] Estimated through TIB2 when in reflect mode. Note this rate is 52 MHz when TIB2 is in transmit mode.

Eqs. 6.2-6.4 are solved with the initial conditions $A = B = 0$ and $\dot{A} = \dot{B} = 0$ at time $t = 0$, and with the cavities initially decoupled, i.e. $g(t) = 0$. Beginning at $t = 0$, an input field with a Gaussian profile of standard deviation s and amplitude maximum at time $\tau_1/2$ is incident on the readout cavity until time τ_1. At τ_1, the input field is turned off and a coupling $g(t) = g_0$ is turned on until τ_2. These boundary conditions and tunable interactions are described by the piecewise functions,

$$A_I(t) = \begin{cases} e^{-(t-\tau_1/2)^2/2s^2}, & 0 < t < \tau_1 \\ 0, & \tau_1 < t \end{cases} \tag{6.5}$$

$$g(t) = \begin{cases} 0, & 0 < t < \tau_1 \\ g_0, & \tau_1 < t < \tau_2. \end{cases} \tag{6.6}$$

Time τ_2 corresponds to the time at which the coupling $g(t)$ is turned off, and when phase-sensitive parametric gain is turned on in the parametric cavity. In this model, gain is assumed to instantaneously exceed loss such that the amplifier efficiency is assumed to be unity.

To estimate the fraction of readout power lost before τ_2, we first numerically solve Eqs. 6.2-6.4 using the definitions in Eq. 6.5 and Eq. 6.6, while setting the cavity internal loss rates to zero ($\kappa_r - \kappa_r^w = 0$ and $\kappa_p = 0$). Doing so, we compute the energy in the parametric cavity immediately

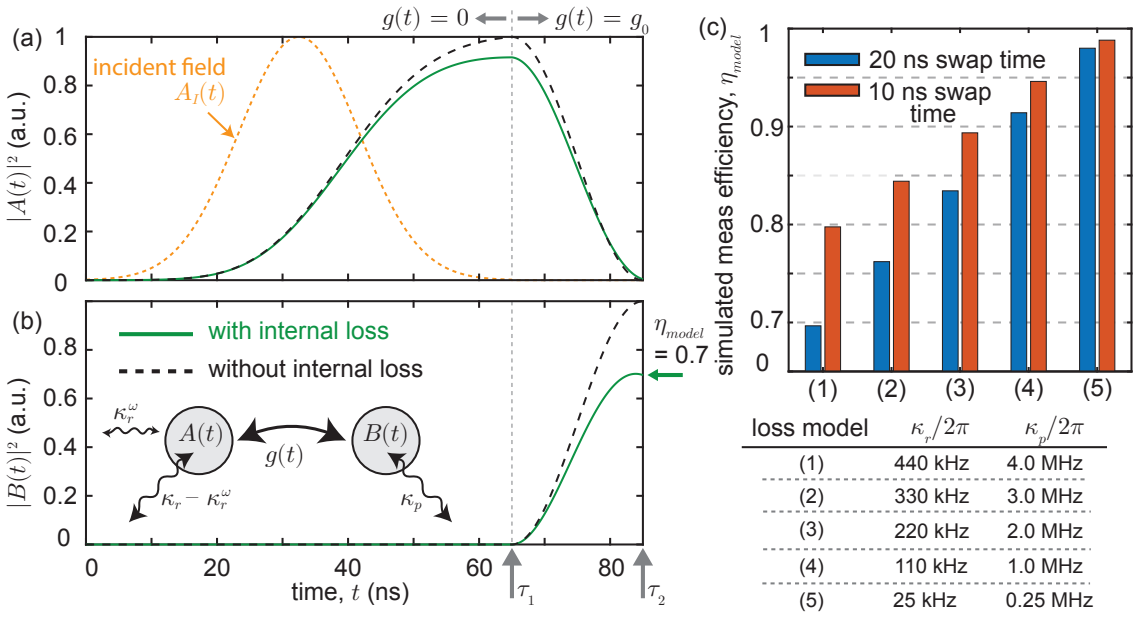

loss model	$\kappa_r/2\pi$	$\kappa_p/2\pi$
(1)	440 kHz	4.0 MHz
(2)	330 kHz	3.0 MHz
(3)	220 kHz	2.0 MHz
(4)	110 kHz	1.0 MHz
(5)	25 kHz	0.25 MHz

Figure 6.9: **Measurement efficiency model.** (a,b) Model of energy vs. time in the readout cavity (a), and parametric cavity (b), which is proportional to $|A(t)|^2$ and $|B(t)|^2$, respectively. This simulation uses Eqs. 6.2-6.4 with the parameters $\kappa_r^w/2\pi \times 8\,\text{kHz}$, $\kappa_r/2\pi \times 440\,\text{kHz}$, $\kappa_p/2\pi = 4.0\,\text{MHz}$, $s = 13\,\text{ns}$, $\tau_1 = 65\,\text{ns}$, $\tau_2 = \tau_1 + 20\,\text{ns}$ and $g_0/2\pi = 12.5\,\text{MHz}$, chosen to emulate the experiment in Ref. [23]. Solid green lines result from a simulation which includes internal loss in both cavities, while the dashed black lines result from a simulation with this loss turned off, $\kappa_r - \kappa_r^w = \kappa_p = 0$. Simulated measurement efficiency η_{model} is the ratio of energy remaining at time τ_2 with/without internal loss included in the model. The time τ_2 corresponds to when the parametric pump is turned on in experiment. (c) Simulated measurement efficiency for five different models of loss in the readout and parametric cavities. The blue bar in model (1) is the simulation shown in subplots a,b, corresponding the the experiment in Ref. [23]. Measurement efficiency is expected to improve to $\eta \geq 0.9$ for the readily realizable parameters of model (4).

before amplification to be $E_0 = \hbar\omega_0|B(\tau_2)|^2$. Next, we choose $\kappa_r \neq 0$ and $\kappa_p \neq 0$, and re-simulate Eqs. 6.2-6.4 to compute the energy in the parametric cavity before amplification *including* this loss, E'. Modelled measurement efficiency is the ratio of these two numbers, $\eta_{model} = E'/E_0$ and depends on κ_p, κ_r and g_0. We experimentally measure the parametric cavity loss rate to be $\kappa_p/2\pi = 4.0 \pm 0.2\,\text{MHz}$ with both TIBs in reflect (Fig. S19 or Ref. [23]). We also measure $g_0 = 12.5\,\text{MHz}$ from the data shown in Fig. 6.3a, and $\eta = 0.70 \pm 0.01$ from the measurement in Fig. 6.7. We therefore compute $\eta_{model} = 0.70$ by using these parameters and estimating the loss rate of the readout cavity to be $\kappa_r/2\pi = 440\,\text{kHz}$.

6.3.3 Excess backaction

Non-zero excess backaction indicates residual coupling between the readout and parametric cavities even when the TIB between them is nominally in reflect mode. The $n_b = 0.66$ photons of backaction reported in Ref. [23] are estimated to correspond to transmission of $-26\,\mathrm{dB}$ through TIB1. This is worse than expected given the $50\,\mathrm{dB}$ on/off ratio characterized in a single TIB, Fig. 5.4. The discrepancy may result from an alternative transmission path which bypasses the TIB when integrated into a SIMBA. An example of such an effect would be a cable mode which is coupled to both the readout and parametric cavities, such that the TIB is not as fine-tuned to reflect well at the cable mode frequency. Such an effect could be eliminated by improving the device packaging so that the SIMBA and qubit are separated by much less than a wavelength at the frequency of interest. Non-zero excess backaction could also result from too low a power handling of the TIB compared to the amplified state in the parametric cavity; this can be improved by increasing the number of SQUIDs per array in the TIBs and also changing their critical currents.

While the precise contributions to excess backaction in the version-1 SIMBA demonstration (Fig. 6.7) are difficult to determine, excess backaction can in-principle be much lower than the $n_b = 0.66$ photons (0.63 effective photons) reported in that work. For example, the version-0 SIMBA demonstration (Fig. 6.6) saw $n_b = 0.018 \pm 0.002$ effective photons of excess backaction compared to $n_r^{\mathrm{proj}} \sim 4$ effective photons in a projective readout pulse. Moreover, this was done at an operating point with approximately $\eta = 44\%$ and readout fidelity of $F_0 = 86\%$ (Fig. S21 of Ref. [23]). This proof-of-principle demonstration gives confidence that with further work, excess backaction can be dramatically lowered while maintaining high efficiency and readout fidelity.

6.3.4 Readout time

Readout using a SIMBA can be significantly sped up without detriment to performance. In principle, a faster readout should also be higher fidelity, due to less chance of a bit flip error from qubit decay before/during measurement.

Table 6.5: **Contributions to measurement time.** Note that the experiment in Ref. [23] has $2\chi/2\pi = 1.93\,\mathrm{MHz}$, $g_0/2\pi = 12.5\,\mathrm{MHz}$ and the SIMBA has a reset time of 100 ns. The 'estimated after improvement' column assumes $2\chi/2\pi = 11\,\mathrm{MHz}$, $g_0/2\pi = 25\,\mathrm{MHz}$ and $\kappa_p/2\pi = 1\,\mathrm{MHz}$.

system	readout pulse	swap	JPA ring-up	digization	total
demonstration in Ref. [23]	65 ns	20 ns	80 ns	100 ns	265 ns
estimated after improvement	15 ns	10 ns	20 ns	25 ns	70 ns

Readout using a SIMBA differs from standard dispersive readout because the readout cavity external coupling rate is now tunable. Advantageously, this rate can be made large during the measurement to allow for fast readout, but can otherwise be tuned close to zero so that the qubit's T_1 time is not Purcell limited [147].

For optimal readout using a SIMBA, it is desirable to minimize loss in the readout cavity such that $2\chi \gg \kappa_r$. In this limit, a readout pulse of appropriate frequency and a duration of approximately $1/2\chi$ will be phase-shifted by $\pm\pi/2$ in phase space, dependent on the qubit state. The dispersive shift alone therefore sets the readout duration when using a SIMBA, not the ratio of $2\chi/\kappa_r$ as in conventional dispersive readout (assuming κ_r is dominated by external loss through a strongly coupled port) [15]. The experiment in Ref. [23] uses $2\chi/2\pi = 1.93\,\mathrm{MHz}$, which can be significantly increased to speed up the readout, while still remaining in the dispersive limit.

The swap time between the readout and parametric cavities can also be sped up simply by increasing the bare coupling rate between them. Doing so should also increase efficiency, Fig. 6.9c. Additionally in Ref. [23], the 80 ns ring-up time for the pumped parametric cavity to reach a stable, bifurcated state was in-principle far longer than necessary, and can be reduced to several nanoseconds by pumping the JPA harder. This results in a higher amplitude state in the pumped parametric cavity, also reducing the time required to digitize this state at room temperature, albeit at the cost of more excess backaction if the TIB isolalation is imperfect.

In conclusion, all steps of the SIMBA readout procedure may be sped up, Table. 6.5. Complicated trade-offs arise between the length of different readout steps and the various metrics for readout performance, but we anticipate a total measurement time of less than 100 ns is achievable

with readily attainable improvements to the experiment in Ref. [23].

6.3.5 Ease of calibration

Finally, ease of calibration is an important factor to consider with regards to scalability. Calibration of qubit readout when using a SIMBA is not significantly more complicated than use of a conventional Josephson parametric amplifier, but can still be simplified.

In particular, in Ref. [23] the parametric amplifier performance (for example, the region where it bifurcates as a function of pump frequency and amplitude), is dependent on the uniform bias flux seen by both TIBs. This is because the SQUID arrays within the TIBs participate somewhat in the parametric amplifier mode. In general this is undesirable; it requires extra care when choosing the uniform magnetic flux applied to the device. This participation can be easily lowered by reducing the coupling between the JPA and TIBs, at the cost of a slower swap time. More difficult but perhaps more useful, the superconducting switch element can be redesigned to participate minimally in the parametric cavity resonance.

Chapter 7

Outlook

A great challenge of quantum information science is to isolate qubits extremely well from their environment while still being able to couple them strongly to other qubits and a measurement apparatus. State-of-the-art performance in any platform requires careful understanding and balance of such tradeoffs. In superconducting systems, tunable coupling elements are a natural way to circumvent this roadblock.

Toward this goal, in this thesis we develop superconducting microwave switches (TIBs), which are used to engineer a 'SIMBA'-style directional amplifier [23]. Using a SIMBA, we demonstrate state-of-the-art readout of a superconducting qubit while eliminating any ferrite circulators/isolators before amplification. Since the limitations of the current generation of SIMBAs are well understood and not inherent to the concept itself, there is a clear path towards using an optimized SIMBA to improve upon current superconducting qubit readout performance in a scalable way. Furthermore, the switches themselves are versatile tools with utility beyond our demonstration of qubit measurement.

We conclude by presenting several promising avenues for future research.

7.1 Parametric coupling to reduce backaction

While the 0.66 photons of excess backaction reported in Ref. [23] is low compared to the several photon readout pulse and the hundreds of photons in the pumped parametric cavity, there is significant room for improvement in performance. Easier calibration is also desirable; for example,

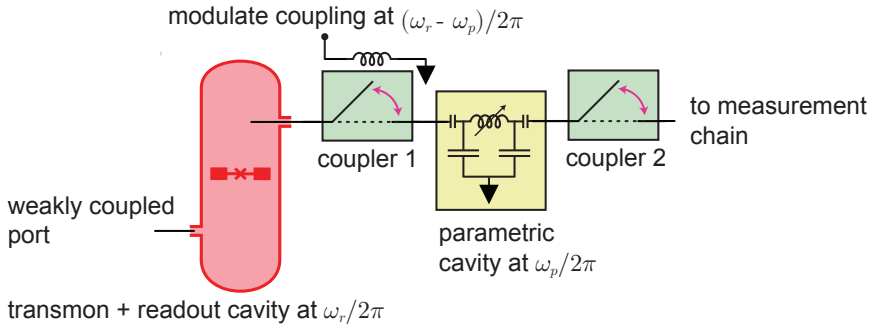

Figure 7.1: **A SIMBA operated using parametric coupling.** As in Ref. [23], a superconducting qubit is dispersively coupled to a readout cavity with a tunable coupler on its output. This coupler is shared by a second cavity which can be parametrically modulated and can be connected to a measurement chain. Unlike in Ref. [23], the parametric cavity is at a different frequency than the readout cavity. Coupling is turned on by modulating the first coupler at the difference frequency between these cavities. With this approach it is much easier to obtain and calibrate good isolation between the readout and parametric cavities, as they are naturally detuned in addition to being decoupled when the modulation is turned off.

the TIB gradiometric bias voltage for optimal isolation can be slightly offset from zero, Fig. 6.4, due to small but unavoidable asymmetry in the circuit layout. It is desirable to have low excess backaction without having to carefully calibrate this bias for every device.

One way to circumvent these problems is to engineer the parametric cavity to be at a *different* frequency from the readout cavity (different by much greater than the linewidths of either cavity), then turn on a beamsplitter interaction between them by parametrically modulating their coupling at this difference frequency, Section. 2.1.7. Isolation is therefore provided by the cavities being far-detuned, in addition to the coupler between them being tuned near reflect mode when interaction is not desired.

In such a system, the coupling rate $g(t)$ between two oscillators is modulated in time such that $g(t) = g_0\,(1 + \epsilon \sin(\Delta t + \theta))$ where $\Delta = |\omega_r - \omega_p|$ is the difference frequency between the two oscillators, g_0 is a bare coupling rate, and ϵ is a modulation amplitude. In the limit $\epsilon \ll 1$, this modulation couples the two oscillators at rate $g_0\epsilon$, Sec. 2.1.7. Improved isolation therefore generally comes with a slower swap step, to the extent that modulation remains in this weak limit.

Alternatively, the parametric cavity could be rapidly tuned in and out of resonance with the

readout cavity in order to swap their states. A swap could be implemented in this manner by sending a square shaped voltage pulse into the uniform flux bias lines already implemented in the SIMBA. Careful tuning of this pulse might be required but in-principle, such a procedure would have the advantage of strong coupling during the swap, combined with isolation due to cavity detuning when the swap is over. Such an approach could even be implemented without a tunable coupling between the readout and parametric cavities.

7.2 Autonomous feedback using a SIMBA

As operated in Ref. [23], the SIMBA stores the qubit measurement result as a classical bit of information in the pumped state of the bifurcation amplifier. This bit can be used for classical information processing, such as in a feedback loop as part of a quantum error correction algorithm. Current state-of-the-art feedback loops [73, 148] are limited by control electronics at room temperature, but also the round-trip time for signals to travel in and out of a cryostat. When using a SIMBA, however, the qubit measurement result is stored at the base temperature stage of a dilution refrigerator. This classical bit of information can in-principle be used to implement fast feedback loops which avoid the round trip travel time between the base of the cryostat and a digitizer at room temperature.

To realize this advantage, we propose a scheme for a rapid feedback loop where a qubit is selectively π-pulse based on a measurement result, Fig. 7.2, similar to the concept in Ref. [149]. In this approach, a carefully calibrated cancellation pulse shifts the state in the parametric cavity to be either near-vacuum or high-amplitude depending on the measurement result. (Such a procedure could also be achieved by using the tri-stable state of the parametric cavity to correlate the state of the qubit with either a high-amplitude state or vacuum [119].) Next, coupling between the parametric cavity and readout cavity is turned back on, shifting the qubit frequency via the ac-Stark shift [16], conditioned on the measurement result. Finally, a pulse is applied to the qubit which is now effective only if its frequency has *not* been shifted. The pulse is therefore conditional on the measurement result.

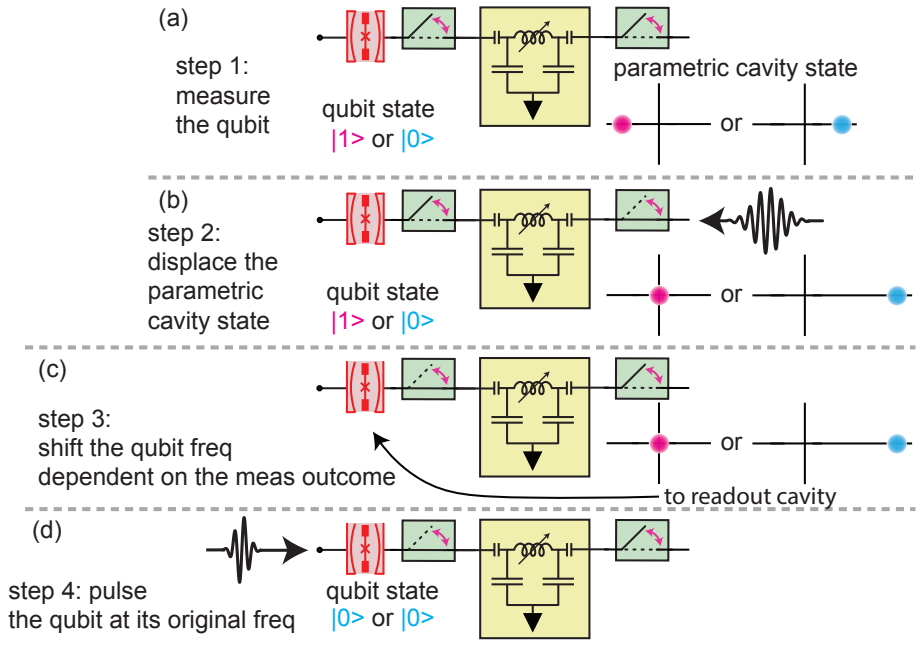

Figure 7.2: **Autonomous feedback.** Fast, conditional π-pulse using a SIMBA. (a) The result of a qubit measurement is stored in the bifurcated state of a parametric cavity. (b) The parametric cavity pump is turned off and the parametric cavity state is displaced by applying a bias tone of appropriate frequency, amplitude and phase. The measurement result is therefore either correlated with near vacuum or a high amplitude state. (c) Next, TIB1 is set to transmit mode to swap the state in the parametric cavity into the readout cavity, shifting the qubit frequency, or not, dependent on the measurement result. (d) Finally, a π-pulse is applied to the qubit, which will only be effective if the qubit frequency has not been shifted (correlated with vacuum in the parametric cavity, and one particular result from the first measurement).

If this procedure works with high fidelity and calibration is not prohibitively difficult, such a procedure could readily be extended to multi-qubit networks. In other words, a Bloch-sphere rotation can be applied on one qubit in a network conditional on the measurement result of a *different* qubit. Such a procedure, if effective, could be useful for improving the speed of feedback loops used for quantum error correction.

7.3 Utility of a readout cavity with tunable external coupling

Even with a conventional measurement setup, it is generally useful to have a superconducting qubit readout cavity with a tunable external coupling. This coupling can be set to zero until

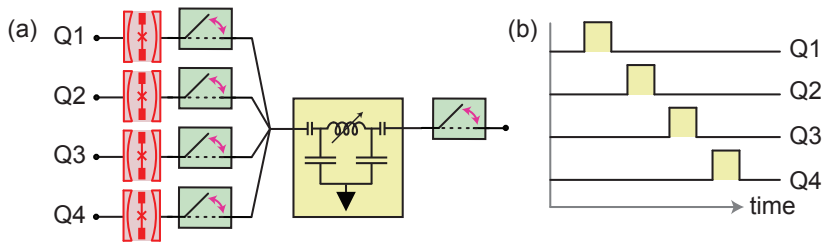

Figure 7.3: **Qubit multiplexing.** (a) Example mutliplexing architecture using a SIMBA. A SIMBA can be constructed using an N × 1 superconducting switch at the input (with N = 4 shown), constructed from TIBs. (b) With an adequate reset time between measurements, the qubits can be time-domain multiplexed using the same SIMBA. (Square pulses in this schematic represent a full measurement, digitization and reset procedure).

measurement, when it can be turned on to allow for fast readout [74].

More precisely, the energy decay time of a superconducting qubit coupled dispersively to a readout cavity is limited by the Purcell effect to be $1/T_1 = (g/\Delta)^2 \kappa_r$ where g is the coupling rate between the qubit and cavity, Δ is the detuning between them, and κ_r is the linewidth of the readout cavity [150, 15, 151] (see Sec. 2.1.6.1). Ideally, the linewidth of a readout cavity is dominated by its coupling to the measurement chain (taking any weak port coupling rate or internal loss to be negligible). The dispersive shift χ is also a function of g and Δ (see Eq. 2.54) such that larger values of κ_r and χ, necessary for faster readout, lower the Purcell limit on a qubit's T_1 time.

This detrimental effect can be inhibited by using a 'Purcell filter', essentially a high-pass filter on the external port of a readout cavity which blocks transmission out of the cavity at the qubit frequency [152]. However, there are still limits to how well any filtering scheme can work [34], and filtering becomes less effective as χ increases. The same benefits of a Purcell filter can be achieved using a readout cavity with a *tunable* external coupling, an approach which is just beginning to be explored [153, 74, 23].

Moreover, readout cavities with a tunable external coupling can be generally useful for multiplexing [79]. Such a feature can be used to reduce frequency crowding as different resonators may in-principle be placed at the same frequency and time-domain multiplexed, as illustrated in Fig. 7.3. This concept can be extended by constructing larger switch networks from TIBs, Sec. 5.4,

or from other styles of couplers [124].

7.4 Superconducting switch from a Wheatstone bridge of capacitors

One non-ideal feature of the TIBs in Refs. [79, 23] is their dependence on the uniform[1] magnetic flux. Recall that there is *no* transmit mode for certain values of this uniform flux including when it is zero (see Eq. 5.1).

A potential solution to this problem is introduced in Ref. [23] by engineering on-chip 'uniform' bias lines surrounding the Wheatstone bridges in these TIBs, different from the 'gradiometric' bias line used to imbalance the bridge. The uniform bias lines are designed so that current flowing through them will thread the same amount of magnetic flux through all SQUIDs in a bridge, allowing this flux to be tuned to an appropriate value without use of an off-chip coil. However, these uniform bias lines can be a source of noise/loss, and furthermore add both to requisite wire count and the complexity of device calibration.

In recognition of these problems, here we present a design for a superconducting switch which is *not* susceptible to any external magnetic field. This concept is illustrated in Fig. 7.4, and is still based on breaking/preserving the symmetry of a Wheatstone bridge. Unlike the TIBs developed in this thesis, however, the design in Fig. 7.4 is based on a Wheatstone bridge of *capacitors*. These capacitors have fixed value, but any tunable impedance placed at the north/south nodes of the bridge can still be used to imbalance it.

For example, tunable inductances can be realized with arrays of Josephson junctions. When the junction arrays are not biased, from symmetry of the circuit the Wheatstone bridge is *balanced* and the device is in reflect mode, Fig. 7.4a. When current is applied through one array, however, symmetry is broken and the bridge becomes effectively *imbalanced* realizing a transmit mode.[2] Capacitors are added to match the network and also break any superconducting loops. Finally, low

[1] 'Uniform', meaning a flux which is the same through all SQUIDs.

[2] In fact, symmetry is broken as long as a different current is applied to the two arrays, causing them to have different inductances. Therefore to imbalance the bridge it is not necessary to apply any current through the second bias line. This line is included in the design, however, to preserve the symmetry of the balanced circuit.

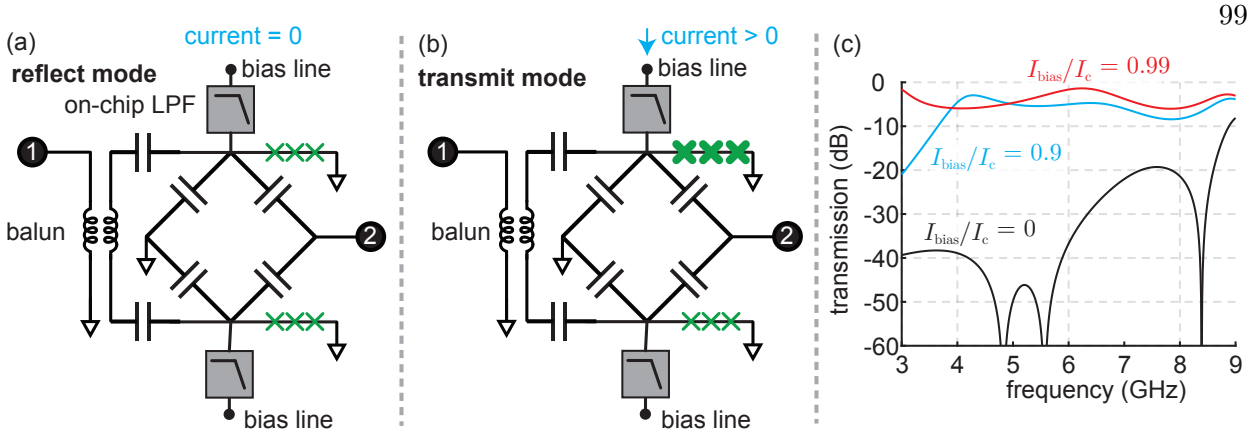

Figure 7.4: **Superconducting switch from a Wheatstone bridge of capacitors.** The bridge can be balanced/imbalanced by applying current through arrays of Josephson junctions placed at its north/south nodes and connected to ground. The inductance of these arrays can be changed by applying current through them, using on-chip bias lines with low-pass filters on them to prevent microwave power from leaving the circuit. (a) Illustration of the bridge in reflect mode. No current is applied through either bias line and the brige is balanced, causing it to reflect. (b) The bridge is imbalanced when current is applied through one bias line, leading to transmission between port 1 to port 2. (c) Numerical simulation of a device based on the design in (a,b). The simulated devices uses the same baluns and low-pass filters as in the SIMBA in Ref. [23], with all capacitors equal to 1 pF and unbiased junction arrays equal to 0.6 nH inductors. Bias current changes the array inductance according to Eq. A.3. Applying a bias current of $I_{\text{bias}}/I_{\text{c}} = 0.9$ gives -6 dB or greater of transmission between approximately 4 GHz and 6 GHz, with an on/off ration of greater than 35 dB over this range.

pass filters are added to the bias lines in order to prevent microwave frequency signal leaking out of them.

Performance of a preliminary version of this design is simulated in Fig. 7.4c. This is a numerical simulation of a chip layout using similar parameters as those of the TIBs in Ref. [23]. An on/off ratio of greater than 40 dB with transmission above -6 dB is simulation between 4 GHz and 6 GHz, when biasing the bridge at $I_{\text{bias}}/I_{\text{c}} = 0.9$. While this performance is not an improvement upon the TIBs in Ref. [23], it does captures the salient features of high on/off ratio and large bandwidth. The parameters of the simulated device still have a great deal of room for optimization.

The advantage of the design in Fig. 7.4 is that it preserves the bandwidth and high on/off ratio of a bridge circuit while not being susceptible to an external magnetic flux. Additionally, it requires only a single on-chip bias line which can in-principle require a much lower bias current

than the flux-biased TIB designs presented earlier in this thesis, therefore providing a lower heat load to the cryostat.

A disadvantage of using Josephson junction arrays as a tunable impedance is that the bias current must be a large fraction of the junction's critical current in order to significantly imbalance the bridge (see Eq. A.3 and Fig. A.1d). A high bias current can potentially limit the match and power handling of such a device, although these features can in general be less important than on/off ratio for the proposed use as a tunable external coupling on a qubit readout cavity. Such problems could potentially be avoided, however, by replacing the arrays of Josephson junctions with asymmetric SQUIDs [46]. The loops of such SQUIDs can be twisted in a figure-8 or 'asymmetrically threaded SQUID' geometry [154], to eliminate any performance dependence on a uniform external magnetic field.

Bibliography

[1] R. P. Feynman, "Simulating physics with computers," International Journal of Theoretical Physics, vol. 21, no. 6, pp. 467–488, Jun 1982. [Online]. Available: https://doi.org/10.1007/BF02650179

[2] ——, "Quantum mechanical computers," Foundations of Physics, vol. 16, no. 6, pp. 507–531, Jun 1986. [Online]. Available: https://doi.org/10.1007/BF01886518

[3] M. H. Freedman, A. Kitaev, M. J. Larsen, and Z. Wang, "Topological quantum computation," arXiv:0101025v2, 2002. [Online]. Available: https://arxiv.org/abs/quant-ph/0101025

[4] S. Aaronson, "The limits of quantum computers," Scientific American, March 2008. [Online]. Available: https://www.scientificamerican.com/article/the-limits-of-quantum-computers/

[5] P. W. Shor, "Algorithms for quantum computation: discrete logarithms and factoring," Proceedings 35th Annual Symposium on Foundations of Computer Science, p. 124–134, 1994. [Online]. Available: https://ieeexplore.ieee.org/document/365700

[6] ——, "Scheme for reducing decoherence in quantum computer memory," Phys. Rev. A, vol. 52, pp. R2493–R2496, Oct 1995. [Online]. Available: https://link.aps.org/doi/10.1103/PhysRevA.52.R2493

[7] A. Steane, "Multiple-particle interference and quantum error correction," Proceedings of the Royal Society of London A: Mathematical, Physical and Engineering Sciences, vol. 452, no. 1954, pp. 2551–2577, 1996. [Online]. Available: https://royalsocietypublishing.org/doi/10.1098/rspa.1996.0136

[8] E. Knill and R. Laflamme, "Theory of quantum error-correcting codes," Phys. Rev. A, vol. 55, pp. 900–911, Feb 1997. [Online]. Available: https://link.aps.org/doi/10.1103/PhysRevA.55.900

[9] D. Aharonov and M. Ben-Or, "Fault-tolerant quantum computation with constant error rate," arXiv preprint arXiv:quant-ph/9906129, 1999. [Online]. Available: https://arxiv.org/abs/quant-ph/9906129

[10] J. Preskill, "Quantum computing in the nisq era and beyond," Quantum, vol. 2, p. 79, 2018. [Online]. Available: https://quantum-journal.org/papers/q-2018-08-06-79/

[11] B. M. Terhal, "Quantum error correction for quantum memories," Rev. Mod. Phys., vol. 87, pp. 307–346, Apr 2015. [Online]. Available: https://link.aps.org/doi/10.1103/RevModPhys.87.307

[12] M. H. Devoret and R. J. Schoelkopf, "Superconducting circuits for quantum information: an outlook," Science, vol. 339, no. 6124, pp. 1169–1174, 2013. [Online]. Available: https://science.sciencemag.org/content/339/6124/1169

[13] A. Blais, A. L. Grimsmo, and A. Wallraff, "Circuit quantum electrodynamics," arXiv:2005.12667, 2020. [Online]. Available: https://arxiv.org/abs/2005.12667

[14] A. Wallraff, D. I. Schuster, A. Blais, L. Frunzio, R.-S. Huang, J. Majer, S. Kumar, S. M. Girvin, and R. J. Schoelkopf, "Strong coupling of a single photon to a superconducting qubit using circuit quantum electrodynamics," Nature, vol. 431, no. 7005, pp. 162–167, 2004. [Online]. Available: https://www.nature.com/articles/nature02851

[15] A. Blais, R.-S. Huang, A. Wallraff, S. M. Girvin, and R. J. Schoelkopf, "Cavity quantum electrodynamics for superconducting electrical circuits: An architecture for quantum computation," Phys. Rev. A, vol. 69, p. 062320, Jun 2004. [Online]. Available: https://link.aps.org/doi/10.1103/PhysRevA.69.062320

[16] D. I. Schuster, A. Wallraff, A. Blais, L. Frunzio, R.-S. Huang, J. Majer, S. M. Girvin, and R. J. Schoelkopf, "ac stark shift and dephasing of a superconducting qubit strongly coupled to a cavity field," Phys. Rev. Lett., vol. 94, p. 123602, Mar 2005. [Online]. Available: https://link.aps.org/doi/10.1103/PhysRevLett.94.123602

[17] D. P. DiVincenzo, "The physical implementation of quantum computation," Fortschr. Phys., vol. 48, pp. 771–783, 2000. [Online]. Available: https://onlinelibrary.wiley.com/doi/10.1002/1521-3978(200009)48:9/11⟨771::AID-PROP771⟩3.0.CO;2-E

[18] J. Koch, T. M. Yu, J. Gambetta, A. A. Houck, D. I. Schuster, J. Majer, A. Blais, M. H. Devoret, S. M. Girvin, and R. J. Schoelkopf, "Charge-insensitive qubit design derived from the cooper pair box," Phys. Rev. A, vol. 76, p. 042319, Oct 2007. [Online]. Available: https://link.aps.org/doi/10.1103/PhysRevA.76.042319

[19] A. Kandala, A. Mezzacapo, K. Temme, M. Takita, M. Brink, J. M. Chow, and J. M. Gambetta, "Hardware-efficient variational quantum eigensolver for small molecules and quantum magnets," Nature, vol. 549, p. 242–246, 2017. [Online]. Available: https://www.nature.com/articles/nature23879

[20] F. Arute, K. Arya, R. Babbush, D. Bacon, J. C. Bardin, R. Barends, R. Biswas, S. Boixo, F. G. S. L. Brandao, D. A. Buell, B. Burkett, Y. Chen, Z. Chen, B. Chiaro, R. Collins, W. Courtney, A. Dunsworth, E. Farhi, B. Foxen, A. Fowler, C. Gidney, M. Giustina, R. Graff, K. Guerin, S. Habegger, M. P. Harrigan, M. J. Hartmann, A. Ho, M. Hoffmann, T. Huang, T. S. Humble, S. V. Isakov, E. Jeffrey, Z. Jiang, D. Kafri, K. Kechedzhi, J. Kelly, P. V. Klimov, S. Knysh, A. Korotkov, F. Kostritsa, D. Landhuis, M. Lindmark, E. Lucero, D. Lyakh, S. Mandrá, J. R. McClean, M. McEwen, A. Megrant, X. Mi, K. Michielsen, M. Mohseni, J. Mutus, O. Naaman, M. Neeley, C. Neill, M. Y. Niu, E. Ostby, A. Petukhov, J. C. Platt, C. Quintana, E. G. Rieffel, P. Roushan, N. C. Rubin, D. Sank, K. J. Satzinger, V. Smelyanskiy, K. J. Sung, M. D. Trevithick, A. Vainsencher, B. Villalonga, T. White, Z. J. Yao, P. Yeh, A. Zalcman, H. Neven, and J. M. Martinis, "Quantum supremacy using a programmable superconducting processor," Nature, vol. 574, p. 505–510, 2019. [Online]. Available: https://www.nature.com/articles/s41586-019-1666-5

[21] C. Wang, Y. Y. Gao, P. Reinhold, R. W. Heeres, N. Ofek, K. Chou, C. Axline, M. Reagor, J. Blumoff, K. M. Sliwa, L. Frunzio, S. M. Girvin, L. Jiang, M. Mirrahimi, M. H. Devoret, and R. J. Schoelkopf, "A schrödinger cat living in two boxes," Science, vol. 352, no. 6289, pp. 1087–1091, 2016. [Online]. Available: https://science.sciencemag.org/content/352/6289/1087

[22] C. S. Wang, J. C. Curtis, B. J. Lester, Y. Zhang, Y. Y. Gao, J. Freeze, V. S. Batista, P. H. Vaccaro, I. L. Chuang, L. Frunzio, L. Jiang, S. M. Girvin, and R. J. Schoelkopf, "Efficient multiphoton sampling of molecular vibronic spectra on a superconducting bosonic processor," Phys. Rev. X, vol. 10, p. 021060, Jun 2020. [Online]. Available: https://link.aps.org/doi/10.1103/PhysRevX.10.021060

[23] E. I. Rosenthal, C. M. F. Schneider, M. Malnou, Z. Zhao, F. Leditzky, B. J. Chapman, W. Wustmann, X. Ma, D. A. Palken, M. F. Zanner, L. R. Vale, G. C. Hilton, J. Gao, G. Smith, G. Kirchmair, and K. W. Lehnert, "Efficient and low-backaction quantum measurement using a chip-scale detector," Phys. Rev. Lett., vol. 126, p. 090503, Mar 2021. [Online]. Available: https://link.aps.org/doi/10.1103/PhysRevLett.126.090503

[24] A. A. Clerk, M. H. Devoret, S. M. Girvin, F. Marquardt, and R. J. Schoelkopf, "Introduction to quantum noise, measurement, and amplification," Rev. Mod. Phys., vol. 82, pp. 1155–1208, Apr 2010. [Online]. Available: https://link.aps.org/doi/10.1103/RevModPhys.82.1155

[25] C. M. Caves, "Quantum limits on noise in linear amplifiers," Phys. Rev. D, vol. 26, pp. 1817–1839, Oct 1982. [Online]. Available: https://link.aps.org/doi/10.1103/PhysRevD.26.1817

[26] C. M. Caves, J. Combes, Z. Jiang, and S. Pandey, "Quantum limits on phase-preserving linear amplifiers," Phys. Rev. A, vol. 86, p. 063802, Dec 2012. [Online]. Available: https://link.aps.org/doi/10.1103/PhysRevA.86.063802

[27] I. Siddiqi, R. Vijay, F. Pierre, C. M. Wilson, M. Metcalfe, C. Rigetti, L. Frunzio, and M. H. Devoret, "Rf-driven josephson bifurcation amplifier for quantum measurement," Phys. Rev. Lett., vol. 93, p. 207002, Nov 2004. [Online]. Available: https://link.aps.org/doi/10.1103/PhysRevLett.93.207002

[28] M. A. Castellanos-Beltran and K. W. Lehnert, "Widely tunable parametric amplifier based on a superconducting quantum interference device array resonator," Applied Physics Letters, vol. 91, no. 8, p. 083509, 2007. [Online]. Available: https://aip.scitation.org/doi/10.1063/1.2773988

[29] T. Yamamoto, K. Inomata, M. Watanabe, K. Matsuba, T. Miyazaki, W. D. Oliver, Y. Nakamura, and J. S. Tsai, "Flux-driven josephson parametric amplifier," Applied Physics Letters, vol. 93, no. 4, p. 042510, 2008. [Online]. Available: https://aip.scitation.org/doi/abs/10.1063/1.2964182?journalCode=apl

[30] N. Bergeal, R. Vijay, V. E. Manucharyan, I. Siddiqi, R. J. Schoelkopf, S. M. Girvin, and M. H. Devoret, "Analog information processing at the quantum limit with a Josephson ring modulator," Nature Physics, vol. 6, no. 4, pp. 296–302, 2010. [Online]. Available: https://www.nature.com/articles/nphys1516

[31] C. Macklin, K. O'Brien, D. Hover, M. E. Schwartz, V. Bolkhovsky, X. Zhang, W. D. Oliver, and I. Siddiqi, "A near–quantum-limited Josephson traveling-wave

parametric amplifier," Science, vol. 350, no. 6258, pp. 307–310, 2015. [Online]. Available: https://science.sciencemag.org/content/350/6258/307

[32] D. H. Slichter, R. Vijay, S. J. Weber, S. Boutin, M. Boissonneault, J. M. Gambetta, A. Blais, and I. Siddiqi, "Measurement-induced qubit state mixing in circuit qed from up-converted dephasing noise," Phys. Rev. Lett., vol. 109, p. 153601, Oct 2012. [Online]. Available: https://link.aps.org/doi/10.1103/PhysRevLett.109.153601

[33] D. Sank, Z. Chen, M. Khezri, J. Kelly, R. Barends, B. Campbell, Y. Chen, B. Chiaro, A. Dunsworth, A. Fowler, E. Jeffrey, E. Lucero, A. Megrant, J. Mutus, M. Neeley, C. Neill, P. J. J. O'Malley, C. Quintana, P. Roushan, A. Vainsencher, T. White, J. Wenner, A. N. Korotkov, and J. M. Martinis, "Measurement-induced state transitions in a superconducting qubit: Beyond the rotating wave approximation," Phys. Rev. Lett., vol. 117, p. 190503, Nov 2016. [Online]. Available: https://link.aps.org/doi/10.1103/PhysRevLett.117.190503

[34] D. M. Pozar, Microwave Engineering, 4th ed. Wiley, 2011. [Online]. Available: https://www.wiley.com/en-us/Microwave+Engineering,+4th+Edition-p-9780470631553

[35] T. Walter, P. Kurpiers, S. Gasparinetti, P. Magnard, A. Potočnik, Y. Salathé, M. Pechal, M. Mondal, M. Oppliger, C. Eichler, and A. Wallraff, "Rapid high-fidelity single-shot dispersive readout of superconducting qubits," Phys. Rev. Applied, vol. 7, p. 054020, May 2017. [Online]. Available: https://link.aps.org/doi/10.1103/PhysRevApplied.7.054020

[36] E. Jeffrey, D. Sank, J. Y. Mutus, T. C. White, J. Kelly, R. Barends, Y. Chen, Z. Chen, B. Chiaro, A. Dunsworth, A. Megrant, P. J. J. O'Malley, C. Neill, P. Roushan, A. Vainsencher, J. Wenner, A. N. Cleland, and J. M. Martinis, "Fast accurate state measurement with superconducting qubits," Phys. Rev. Lett., vol. 112, p. 190504, May 2014. [Online]. Available: https://link.aps.org/doi/10.1103/PhysRevLett.112.190504

[37] S. S. Elder, C. S. Wang, P. Reinhold, C. T. Hann, K. S. Chou, B. J. Lester, S. Rosenblum, L. Frunzio, L. Jiang, and R. J. Schoelkopf, "High-fidelity measurement of qubits encoded in multilevel superconducting circuits," Phys. Rev. X, vol. 10, p. 011001, Jan 2020. [Online]. Available: https://link.aps.org/doi/10.1103/PhysRevX.10.011001

[38] A. Wallraff, D. I. Schuster, A. Blais, L. Frunzio, J. Majer, M. H. Devoret, S. M. Girvin, and R. J. Schoelkopf, "Approaching unit visibility for control of a superconducting qubit with dispersive readout," Phys. Rev. Lett., vol. 95, p. 060501, Aug 2005. [Online]. Available: https://link.aps.org/doi/10.1103/PhysRevLett.95.060501

[39] I. Siddiqi, R. Vijay, M. Metcalfe, E. Boaknin, L. Frunzio, R. J. Schoelkopf, and M. H. Devoret, "Dispersive measurements of superconducting qubit coherence with a fast latching readout," Phys. Rev. B, vol. 73, p. 054510, Feb 2006. [Online]. Available: https://link.aps.org/doi/10.1103/PhysRevB.73.054510

[40] M. A. Castellanos-Beltran, K. D. Irwin, G. C. Hilton, L. R. Vale, and K. W. Lehnert, "Amplification and squeezing of quantum noise with a tunable Josephson metamaterial," Nature Physics, vol. 4, no. 12, pp. 929–931, 2008. [Online]. Available: https://www.nature.com/articles/nphys1090

[41] B. Abdo, F. Schackert, M. Hatridge, C. Rigetti, and M. Devoret, "Josephson amplifier for qubit readout," Applied Physics Letters, vol. 99, no. 16, pp. –, 2011. [Online]. Available: http://scitation.aip.org/content/aip/journal/apl/99/16/10.1063/1.3653473

[42] T. Roy, S. Kundu, M. Chand, A. M. Vadiraj, A. Ranadive, N. Nehra, M. P. Patankar, J. Aumentado, A. Clerk, and R. Vijay, "Broadband parametric amplification with impedance engineering: Beyond the gain-bandwidth product," Applied Physics Letters, vol. 107, no. 262601, 2015. [Online]. Available: https://aip.scitation.org/doi/abs/10.1063/1.4939148?journalCode=apl

[43] E. I. Rosenthal, B. J. Chapman, A. P. Higginbotham, J. Kerckhoff, and K. W. Lehnert, "Breaking Lorentz reciprocity with frequency conversion and delay," Phys. Rev. Lett., vol. 119, p. 147703, Oct 2017. [Online]. Available: https://link.aps.org/doi/10.1103/PhysRevLett.119.147703

[44] L. Ranzani, S. Kotler, A. J. Sirois, M. P. DeFeo, M. Castellanos-Beltran, K. Cicak, L. R. Vale, and J. Aumentado, "Wideband isolation by frequency conversion in a josephson-junction transmission line," Phys. Rev. Applied, vol. 8, p. 054035, Nov 2017. [Online]. Available: https://link.aps.org/doi/10.1103/PhysRevApplied.8.054035

[45] B. J. Chapman, E. I. Rosenthal, and K. W. Lehnert, "Design of an on-chip superconducting microwave circulator with octave bandwidth," Phys. Rev. Applied, vol. 11, p. 044048, Apr 2019. [Online]. Available: https://link.aps.org/doi/10.1103/PhysRevApplied.11.044048

[46] N. E. Frattini, U. Vool, S. Shankar, A. Narla, K. M. Sliwa, and M. H. Devoret, "3-wave mixing josephson dipole element," Applied Physics Letters, vol. 110, no. 22, p. 222603, 2017. [Online]. Available: https://aip.scitation.org/doi/10.1063/1.4984142

[47] N. E. Frattini, V. V. Sivak, A. Lingenfelter, S. Shankar, and M. H. Devoret, "Optimizing the nonlinearity and dissipation of a snail parametric amplifier for dynamic range," Phys. Rev. Applied, vol. 10, p. 054020, Nov 2018. [Online]. Available: https://link.aps.org/doi/10.1103/PhysRevApplied.10.054020

[48] A. Opremcak, I. V. Pechenezhskiy, C. Howington, B. G. Christensen, M. A. Beck, E. Leonard Jr., J. Suttle, C. Wilen, K. N. Nesterov, G. J. Ribeill, T. Thorbeck, F. Schlenker, M. G. Vavilov, B. L. T. Plourde, and R. McDermott, "Measurement of a superconducting qubit with a microwave photon counter," Science, vol. 361, no. 6408, p. 1239–1242, 2018. [Online]. Available: https://science.sciencemag.org/content/361/6408/1239

[49] A. Eddins, J. M. Kreikebaum, D. M. Toyli, E. M. Levenson-Falk, A. Dove, W. P. Livingston, B. A. Levitan, L. C. G. Govia, A. A. Clerk, and I. Siddiqi, "High-efficiency measurement of an artificial atom embedded in a parametric amplifier," Phys. Rev. X, vol. 9, p. 011004, Jan 2019. [Online]. Available: https://link.aps.org/doi/10.1103/PhysRevX.9.011004

[50] A. Opremcak, C. H. Liu, C. Wilen, K. Okubo, B. G. Christensen, D. Sank, T. C. White, A. Vainsencher, M. Giustina, A. Megrant, B. Burkett, B. L. T. Plourde, and R. McDermott, "High-fidelity measurement of a superconducting qubit using an on-chip microwave photon counter," Phys. Rev. X, vol. 11, p. 011027, Feb 2021. [Online]. Available: https://link.aps.org/doi/10.1103/PhysRevX.11.011027

[51] K. O'Brien, C. Macklin, I. Siddiqi, and X. Zhang, "Resonant phase matching of josephson junction traveling wave parametric amplifiers," Phys. Rev. Lett., vol. 113, p. 157001, Oct 2014. [Online]. Available: https://link.aps.org/doi/10.1103/PhysRevLett.113.157001

[52] T. White, J. Mutus, I.-C. Hoi, R. Barends, B. Campbell, Y. Chen, Z. Chen, B. Chiaro, A. Dunsworth, E. Jeffrey, J. Kelly, A. Megrant, C. Neill, P. J. J. O'Malley, P. Roushan, D. Sank, A. Vainsencher, J. Wenner, S. Chaudhuri, J. Gao, and J. M. Martinis, "Traveling wave parametric amplifier with josephson junctions using minimal resonator phase matching," Applied Physics Letters, vol. 106, no. 242601, 2015. [Online]. Available: https://aip.scitation.org/doi/abs/10.1063/1.4922348?journalCode=apl

[53] V. V. Sivak, S. Shankar, G. Liu, J. Aumentado, and M. H. Devoret, "Josephson array-mode parametric amplifier," Phys. Rev. Applied, vol. 13, p. 024014, Feb 2020. [Online]. Available: https://link.aps.org/doi/10.1103/PhysRevApplied.13.024014

[54] L. Planat, A. Ranadive, R. Dassonneville, J. Puertas Martínez, S. Léger, C. Naud, O. Buisson, W. Hasch-Guichard, D. M. Basko, and N. Roch, "Photonic-crystal josephson traveling-wave parametric amplifier," Phys. Rev. X, vol. 10, p. 021021, Apr 2020. [Online]. Available: https://link.aps.org/doi/10.1103/PhysRevX.10.021021

[55] M. Vissers, R. Erickson, H.-S. Ku, L. Vale, X. Wu, G. Hilton, and D. Pappas, "Low-noise kinetic inductance traveling-wave amplifier using three-wave mixing," Applied Physics Letters, vol. 108, no. 1, p. 012601, 2016. [Online]. Available: https://aip.scitation.org/doi/10.1063/1.4937922

[56] L. Ranzani, M. Bal, K. C. Fong, G. Ribeill, X. Wu, J. Long, H.-S. Ku, R. Erickson, D. Pappas, and T. Ohki, "Kinetic inductance traveling-wave amplifiers for multiplexed qubit readout," Applied Physics Letters, vol. 113, no. 24, p. 242602, 2018. [Online]. Available: https://aip.scitation.org/doi/10.1063/1.5063252

[57] M. Malnou, M. Vissers, J. Wheeler, J. Aumentado, J. Hubmayr, J. Ullom, and J. Gao, "Three-wave mixing kinetic inductance traveling-wave amplifier with near-quantum-limited noise performance," PRX Quantum, vol. 2, p. 010302, Jan 2021. [Online]. Available: https://link.aps.org/doi/10.1103/PRXQuantum.2.010302

[58] L. Ranzani and J. Aumentado, "Circulators at the quantum limit: Recent realizations of quantum-limited superconducting circulators and related approaches," IEEE Microwave Magazine, vol. 20, 2019. [Online]. Available: https://ieeexplore.ieee.org/document/8661687

[59] ——, "Graph-based analysis of nonreciprocity in coupled-mode systems," New Journal of Physics, vol. 17, no. 2, p. 023024, 2015. [Online]. Available: https://iopscience.iop.org/article/10.1088/1367-2630/17/2/023024

[60] J. Kerckhoff, K. Lalumière, B. J. Chapman, A. Blais, and K. W. Lehnert, "On-chip superconducting microwave circulator from synthetic rotation," Phys. Rev. Applied, vol. 4, p. 034002, Sep 2015. [Online]. Available: http://link.aps.org/doi/10.1103/PhysRevApplied.4.034002

[61] B. J. Chapman, E. I. Rosenthal, J. Kerckhoff, B. A. Moores, L. R. Vale, J. A. B. Mates, G. C. Hilton, K. Lalumière, A. Blais, and K. W. Lehnert, "Widely tunable on-chip

microwave circulator for superconducting quantum circuits," Phys. Rev. X, vol. 7, p. 041043, Nov 2017. [Online]. Available: https://link.aps.org/doi/10.1103/PhysRevX.7.041043

[62] B. Abdo, N. T. Bronn, O. Jinka, S. Olivadese, M. Brink, and J. M. Chow, "Multi-path interferometric Josephson directional amplifier for qubit readout," Quantum Science and Technology, vol. 3, no. 2, p. 024003, 2018. [Online]. Available: http://stacks.iop.org/2058-9565/3/i=2/a=024003

[63] B. Abdo, K. Sliwa, S. Shankar, M. Hatridge, L. Frunzio, R. Schoelkopf, and M. Devoret, "Josephson directional amplifier for quantum measurement of superconducting circuits," Phys. Rev. Lett., vol. 112, p. 167701, Apr 2014. [Online]. Available: https://link.aps.org/doi/10.1103/PhysRevLett.112.167701

[64] K. M. Sliwa, M. Hatridge, A. Narla, S. Shankar, L. Frunzio, R. J. Schoelkopf, and M. H. Devoret, "Reconfigurable josephson circulator/directional amplifier," Phys. Rev. X, vol. 5, p. 041020, Nov 2015. [Online]. Available: https://link.aps.org/doi/10.1103/PhysRevX.5.041020

[65] F. Lecocq, L. Ranzani, G. A. Peterson, K. Cicak, R. W. Simmonds, J. D. Teufel, and J. Aumentado, "Nonreciprocal microwave signal processing with a field-programmable Josephson amplifier," Phys. Rev. Applied, vol. 7, p. 024028, Feb 2017. [Online]. Available: https://link.aps.org/doi/10.1103/PhysRevApplied.7.024028

[66] F. Lecocq, L. Ranzani, G. A. Peterson, K. Cicak, A. Metelmann, S. Kotler, R. W. Simmonds, J. D. Teufel, and J. Aumentado, "Microwave measurement beyond the quantum limit with a nonreciprocal amplifier," Phys. Rev. Applied, vol. 13, p. 044005, Apr 2020. [Online]. Available: https://link.aps.org/doi/10.1103/PhysRevApplied.13.044005

[67] D. Jalas, A. Petrov, M. Eich, W. Freude, S. Fan, Z. Yu, R. Baets, M. Popović, A. Melloni, J. D. Joannopoulos, M. Vanwolleghem, C. R. Doerr, and H. Renner, "What is — and what is not — an optical isolator," Nature Photonics, vol. 7, p. 579–582, 2013. [Online]. Available: https://www.nature.com/articles/nphoton.2013.185

[68] D. L. Sounas and A. Alù, "Non-reciprocal photonics based on time modulation," Nature Photonics, vol. 11, p. 774–783, 2017. [Online]. Available: https://www.nature.com/articles/s41566-017-0051-x

[69] B. Abdo, N. T. Bronn, O. Jinka, S. Olivadese, A. D. Córcoles, V. P. Adiga, M. Brink, R. E. Lake, X. Wu, D. P. Pappas, and J. M. Chow, "Active protection of a superconducting qubit with an interferometric josephson isolator," Nature communications, vol. 10, no. 3154, 2019. [Online]. Available: https://www.nature.com/articles/s41467-019-11101-3

[70] B. Abdo, O. Jinka, N. T. Bronn, S. Olivadese, and M. Brink, "On-chip single-pump interferometric josephson isolator for quantum measurements," arXiv preprint arXiv:2006.01918, 2020. [Online]. Available: https://arxiv.org/abs/2006.01918

[71] F. Lecocq, L. Ranzani, G. A. Peterson, K. Cicak, X. Y. Jin, R. W. Simmonds, J. D. Teufel, and J. Aumentado, "Efficient qubit measurement with a nonreciprocal microwave amplifier," Phys. Rev. Lett., vol. 126, p. 020502, Jan 2021. [Online]. Available: https://link.aps.org/doi/10.1103/PhysRevLett.126.020502

[72] A. Lupaşcu, S. Saito, T. Picot, P. C. De Groot, C. J. P. M. Harmans, and J. E. Mooij, "Quantum non-demolition measurement of a superconducting two-level system," Nature Physics, vol. 3, no. 2, pp. 119–123, 2007. [Online]. Available: https://www.nature.com/articles/nphys509

[73] C. K. Andersen, A. Remm, S. Lazar, S. Krinner, J. Heinsoo, J.-C. Besse, M. Gabureac, A. Wallraff, and C. Eichler, "Entanglement stabilization using ancilla-based parity detection and real-time feedback in superconducting circuits," npj Quantum Information, vol. 5, 2019. [Online]. Available: https://www.nature.com/articles/s41534-019-0185-4

[74] T. Peronnin, D. Marković, Q. Ficheux, and B. Huard, "Sequential dispersive measurement of a superconducting qubit," Phys. Rev. Lett., vol. 124, p. 180502, May 2020. [Online]. Available: https://link.aps.org/doi/10.1103/PhysRevLett.124.180502

[75] S. Touzard, A. Kou, N. E. Frattini, V. V. Sivak, S. Puri, A. Grimm, L. Frunzio, S. Shankar, and M. H. Devoret, "Gated conditional displacement readout of superconducting qubits," Phys. Rev. Lett., vol. 122, p. 080502, Feb 2019. [Online]. Available: https://link.aps.org/doi/10.1103/PhysRevLett.122.080502

[76] J. Heinsoo, C. K. Andersen, A. Remm, S. Krinner, T. Walter, Y. Salathé, S. Gasparinetti, J.-C. Besse, A. Potočnik, A. Wallraff, and C. Eichler, "Rapid high-fidelity multiplexed readout of superconducting qubits," Phys. Rev. Applied, vol. 10, p. 034040, Sep 2018. [Online]. Available: https://link.aps.org/doi/10.1103/PhysRevApplied.10.034040

[77] C. C. Bultink, B. Tarasinski, N. Haandbæk, S. Poletto, N. Haider, D. J. Michalak, A. Bruno, and L. DiCarlo, "General method for extracting the quantum efficiency of dispersive qubit readout in circuit qed," Applied Physics Letters, vol. 112, no. 9, 2018. [Online]. Available: https://aip.scitation.org/doi/abs/10.1063/1.5015954?journalCode=apl

[78] A. Eddins, S. Schreppler, D. M. Toyli, L. S. Martin, S. Hacohen-Gourgy, L. C. G. Govia, H. Ribeiro, A. A. Clerk, and I. Siddiqi, "Stroboscopic qubit measurement with squeezed illumination," Phys. Rev. Lett., vol. 120, p. 040505, Jan 2018. [Online]. Available: https://link.aps.org/doi/10.1103/PhysRevLett.120.040505

[79] B. J. Chapman, B. A. Moores, E. I. Rosenthal, J. Kerckhoff, and K. W. Lehnert, "General purpose multiplexing device for cryogenic microwave systems," Applied Physics Letters, vol. 108, no. 22, p. 222602, 2016. [Online]. Available: https://aip.scitation.org/doi/abs/10.1063/1.4952772

[80] R. Shankar, Principles of Quantum Mechanics, 2nd ed. Springer, 2011. [Online]. Available: https://link.springer.com/book/10.1007/978-1-4757-0576-8

[81] P. Krantz, M. Kjaergaard, F. Yan, T. P. Orlando, S. Gustavsson, , and W. D. Oliver, "A quantum engineer's guide to superconducting qubits," Applied Physics Reviews, vol. 6, no. 021318, 2019. [Online]. Available: https://aip.scitation.org/doi/10.1063/1.5089550

[82] D. F. Walls and G. J. Milburn, Quantum Optics. Springer, 1994. [Online]. Available: https://www.springer.com/gp/book/9783540285731

[83] T. Van Duzer and C. W. Turner, Principles of superconductive devices and circuits, 2nd ed. Pearson, 1981. [Online]. Available: https://www.pearson.com/us/higher-education/

program/Van-Duzer-Principles-of-Superconductive-Devices-and-Circuits-2nd-Edition/PGM1410.html

[84] V. E. Manucharyan, E. Boaknin, M. Metcalfe, R. Vijay, I. Siddiqi, and M. Devoret, "Microwave bifurcation of a Josephson junction: Embedding-circuit requirements," Phys. Rev. B, vol. 76, p. 014524, Jul 2007. [Online]. Available: https://link.aps.org/doi/10.1103/PhysRevB.76.014524

[85] W. Wustmann and V. Shumeiko, "Parametric resonance in tunable superconducting cavities," Phys. Rev. B, vol. 87, p. 184501, May 2013. [Online]. Available: https://link.aps.org/doi/10.1103/PhysRevB.87.184501

[86] R. Loudon, The Quantum Theory of Light, 3rd ed. Oxford Science Publications, 2000. [Online]. Available: https://global.oup.com/academic/product/the-quantum-theory-of-light-9780198501763?cc=us&lang=en&

[87] C. Gerry and P. Knight, Introductory Quantum Optics. Cambridge University Press, 2004. [Online]. Available: https://www.cambridge.org/core/books/introductory-quantum-optics/B9866F1F40C45936A81D03AF7617CF44

[88] M. Kjaergaard, M. E. Schwartz, J. Braumüller, P. Krantz, J. I.-J. Wang, S. Gustavsson, and W. D. Oliver, "Superconducting qubits: Current state of play," Annual Reviews of Condensed Matter Physics, vol. 11, pp. 369–395, March 2020. [Online]. Available: https://www.annualreviews.org/doi/abs/10.1146/annurev-conmatphys-031119-050605

[89] J. A. Schreier, A. A. Houck, J. Koch, D. I. Schuster, B. R. Johnson, J. M. Chow, J. M. Gambetta, J. Majer, L. Frunzio, M. H. Devoret, S. M. Girvin, and R. J. Schoelkopf, "Suppressing charge noise decoherence in superconducting charge qubits," Phys. Rev. B, vol. 77, p. 180502, May 2008. [Online]. Available: https://link.aps.org/doi/10.1103/PhysRevB.77.180502

[90] E. Jaynes and F. Cummings, "Comparison of quantum and semiclassical radiation theories with application to the beam maser," Proceedings of the IEEE, vol. 51, 1963. [Online]. Available: https://ieeexplore.ieee.org/document/1443594

[91] M. J. Collett and C. W. Gardiner, "Squeezing of intracavity and traveling-wave light fields produced in parametric amplification," Phys. Rev. A, vol. 30, pp. 1386–1391, Sep 1984. [Online]. Available: https://link.aps.org/doi/10.1103/PhysRevA.30.1386

[92] C. W. Gardiner and M. J. Collett, "Input and output in damped quantum systems: Quantum stochastic differential equations and the master equation," Phys. Rev. A, vol. 31, pp. 3761–3774, Jun 1985. [Online]. Available: https://link.aps.org/doi/10.1103/PhysRevA.31.3761

[93] C. Gardiner and P. Zoller, Quantum noise. Springer Science & Business Media, 2004. [Online]. Available: https://www.springer.com/gp/book/9783540223016

[94] M. Reagor, H. Paik, G. Catelani, L. Sun, C. Axline, E. Holland, I. M. Pop, N. A. Masluk, T. Brecht, L. Frunzio, M. H. Devoret, L. Glazman, and R. J. Schoelkopf, "Reaching 10 ms single photon lifetimes for superconducting aluminum cavities," Applied Physics Letters, vol. 102, no. 19, p. 192604, 2013. [Online]. Available: https://aip.scitation.org/doi/abs/10.1063/1.4807015

[95] M. Malnou, D. A. Palken, B. M. Brubaker, L. R. Vale, G. C. Hilton, and K. W. Lehnert, "Squeezed vacuum used to accelerate the search for a weak classical signal," Phys. Rev. X, vol. 9, p. 021023, May 2019. [Online]. Available: https://link.aps.org/doi/10.1103/PhysRevX.9.021023

[96] C. K. Andersen, A. Kamal, N. A. Masluk, I. M. Pop, A. Blais, and M. H. Devoret, "Quantum versus classical switching dynamics of driven dissipative kerr resonators," Phys. Rev. Applied, vol. 13, p. 044017, Apr 2020. [Online]. Available: https://link.aps.org/doi/10.1103/PhysRevApplied.13.044017

[97] H. Paik, D. I. Schuster, L. S. Bishop, G. Kirchmair, G. Catelani, A. P. Sears, B. R. Johnson, M. J. Reagor, L. Frunzio, L. I. Glazman, S. M. Girvin, M. H. Devoret, and R. J. Schoelkopf, "Observation of high coherence in josephson junction qubits measured in a three-dimensional circuit qed architecture," Phys. Rev. Lett., vol. 107, p. 240501, Dec 2011. [Online]. Available: https://link.aps.org/doi/10.1103/PhysRevLett.107.240501

[98] G.-S. M. Blais, Alexandre and W. D. Oliver, "Quantum information processing and quantum optics with circuit quantum electrodynamics," Nature Physics, vol. 16, pp. 247—-256, 2020.

[99] A. Einstein, B. Podolsky, and N. Rosen, "Can quantum-mechanical description of physical reality be considered complete?" Phys. Rev., vol. 47, pp. 777–780, May 1935. [Online]. Available: https://link.aps.org/doi/10.1103/PhysRev.47.777

[100] J. Preskill, Lecture Notes for Ph219/CS219: Quantum Information and Computation Chapter 2, 2015. [Online]. Available: \OT1\textquotedblrighthttp://www.theory.caltech.edu/people/preskill/ph229/

[101] K. Kraus, "General state changes in quantum theory," Ann. Phys., vol. 64, pp. 311–335, 1971. [Online]. Available: https://www.sciencedirect.com/science/article/abs/pii/0003491671901084

[102] M. Dall'Arno, G. M. D'Ariano, and M. F. Sacchi, "Purification of noisy quantum measurements," Phys. Rev. A, vol. 82, p. 042315, Oct 2010. [Online]. Available: https://link.aps.org/doi/10.1103/PhysRevA.82.042315

[103] J.-H. Yeh, J. LeFebvre, S. Premaratne, F. C. Wellstood, and B. S. Palmer, "Microwave attenuators for use with quantum devices below 100 mk," Journal of Applied Physics, vol. 121, p. 224501, 2017. [Online]. Available: https://aip.scitation.org/doi/10.1063/1.4984894

[104] Z. Wang, S. Shankar, Z. Minev, P. Campagne-Ibarcq, A. Narla, and M. Devoret, "Cavity attenuators for superconducting qubits," Phys. Rev. Applied, vol. 11, p. 014031, Jan 2019. [Online]. Available: https://link.aps.org/doi/10.1103/PhysRevApplied.11.014031

[105] A. A. Clerk and D. W. Utami, "Using a qubit to measure photon-number statistics of a driven thermal oscillator," Phys. Rev. A, vol. 75, p. 042302, Apr 2007. [Online]. Available: https://link.aps.org/doi/10.1103/PhysRevA.75.042302

[106] F. Yan, S. Gustavsson, A. Kamal, J. Birenbaum, A. P. Sears, D. Hover, T. J. Gudmundsen, D. Rosenberg, G. Samach, S. Weber, J. L. Yoder, T. P. Orlando, J. Clarke, A. J. Kerman, and W. D. Oliver, "The flux qubit revisited to enhance coherence and reproducibility," Nature communications, vol. 7, no. 12964, 2016. [Online]. Available: https://www.nature.com/articles/ncomms12964

[107] A. N. Korotkov, "Quantum bayesian approach to circuit qed measurement with moderate bandwidth," Phys. Rev. A, vol. 94, p. 042326, Oct 2016. [Online]. Available: https://link.aps.org/doi/10.1103/PhysRevA.94.042326

[108] J. Gambetta, W. A. Braff, A. Wallraff, S. M. Girvin, and R. J. Schoelkopf, "Protocols for optimal readout of qubits using a continuous quantum nondemolition measurement," Phys. Rev. A, vol. 76, p. 012325, Jul 2007. [Online]. Available: https://link.aps.org/doi/10.1103/PhysRevA.76.012325

[109] A. A. Clerk, S. M. Girvin, and A. D. Stone, "Quantum-limited measurement and information in mesoscopic detectors," Phys. Rev. B, vol. 67, p. 165324, Apr 2003. [Online]. Available: https://link.aps.org/doi/10.1103/PhysRevB.67.165324

[110] R. Han, G. Leuchs, and M. Grassl, "Residual and destroyed accessible information after measurements," Phys. Rev. Lett., vol. 120, p. 160501, Apr 2018. [Online]. Available: https://link.aps.org/doi/10.1103/PhysRevLett.120.160501

[111] C. Shannon, "A mathematical theory of communication," Bell System Technical Journal, vol. 27, pp. 379–423,623–656, 1948. [Online]. Available: https://ieeexplore.ieee.org/document/6773024

[112] C. Helstrom, Quantum detection and estimation theory. Academic Press: New York, 1976. [Online]. Available: https://link.springer.com/article/10.1007/BF01007479

[113] S. Dolinar, "An optimum receiver for the binary coherent state quantum channel," MIT Research Laboratory of Electronics Quarterly Progress Report, vol. 111, pp. 115–120, 1973.

[114] J. Geremia, "Distinguishing between optical coherent states with imperfect detection," Phys. Rev. A, vol. 70, p. 062303, Dec 2004. [Online]. Available: https://link.aps.org/doi/10.1103/PhysRevA.70.062303

[115] F. E. Becerra, J. Fan, G. Baumgartner, J. Goldhar, J. T. Kosloski, and A. Migdall, "Experimental demonstration of a receiver beating the standard quantum limit for multiple nonorthogonal state discrimination," Nature Photonics, vol. 7, pp. 147–152, 2013. [Online]. Available: https://www.nature.com/articles/nphoton.2012.316

[116] P. Krantz, Y. Reshitnyk, W. Wustmann, J. Bylander, S. Gustavsson, W. D. Oliver, T. Duty, V. Shumeiko, and P. Delsing, "Investigation of nonlinear effects in josephson parametric oscillators used in circuit quantum electrodynamics," New J. Phys., vol. 15, no. 105002, 2013. [Online]. Available: https://iopscience.iop.org/article/10.1088/1367-2630/15/10/105002

[117] M. Malnou, D. A. Palken, L. R. Vale, G. C. Hilton, and K. W. Lehnert, "Optimal operation of a josephson parametric amplifier for vacuum squeezing," Phys. Rev. Applied, vol. 9, p. 044023, Apr 2018. [Online]. Available: https://link.aps.org/doi/10.1103/PhysRevApplied.9.044023

[118] W. Wustmann and V. Shumeiko, "Parametric effects in circuit quantum electrodynamics," Low Temperature Physics, vol. 45, p. 848, 2019. [Online]. Available: https://aip.scitation.org/doi/abs/10.1063/1.5116533?journalCode=ltp

[119] P. Krantz, A. Bengtsson, M. Simoen, S. Gustavsson, V. Shumeiko, W. D. Oliver, C. M. Wilson, P. Delsing, and B. Bylander, "Single-shot read-out of a superconducting qubit using

a josephson parametric oscillator," Nature communications, vol. 7, no. 11417, 2016. [Online]. Available: https://www.nature.com/articles/ncomms11417

[120] I.-M. Svensson, A. Bengtsson, P. Krantz, J. Bylander, V. Shumeiko, and P. Delsing, "Period-tripling subharmonic oscillations in a driven superconducting resonator," Phys. Rev. B, vol. 96, p. 174503, Nov 2017. [Online]. Available: https://link.aps.org/doi/10.1103/PhysRevB.96.174503

[121] R. C. Bialczak, M. Ansmann, M. Hofheinz, M. Lenander, E. Lucero, M. Neeley, A. D. O'Connell, D. Sank, H. Wang, M. Weides, J. Wenner, T. Yamamoto, A. N. Cleland, and J. M. Martinis, "Fast tunable coupler for superconducting qubits," Phys. Rev. Lett., vol. 106, p. 060501, Feb 2011. [Online]. Available: https://link.aps.org/doi/10.1103/PhysRevLett.106.060501

[122] Y. P. Zhong, H.-S. Chang, K. J. Satzinger, M.-H. Chou, A. Bienfait, C. R. Conner, É. Dumur, J. Grebel, G. A. Peairs, R. G. Povey, D. I. Schuster, and A. N. Cleland, "Violating Bell's inequality with remotely-connected superconducting qubits," Nature Physics, vol. 15, pp. 741—-744, 2019. [Online]. Available: https://www.nature.com/articles/s41567-019-0507-7

[123] O. Naaman, M. O. Abutaleb, C. Kirby, and M. Rennie, "On-chip josephson junction microwave switch," Applied Physics Letters, vol. 108, no. 11, p. 112601, 2016. [Online]. Available: https://aip.scitation.org/doi/10.1063/1.4943602

[124] Chang, H.-S., Y. P. Satzinger, K. J.and Zhong, A. Bienfait, M.-H. Chou, C. R. Conner, E. Dumur, J. Grebel, G. A. Peairs, R. G. Povey, and A. N. Cleland, "A fast and large bandwidth superconducting variable coupler," Applied Physics Letters, vol. 117, p. 244001, 2020. [Online]. Available: https://aip.scitation.org/doi/abs/10.1063/5.0028840

[125] K. J. Satzinger, Y. P. Zhong, H.-S. Chang, G. A. Peairs, A. Bienfait, M.-H. Chou, A. Y. Cleland, C. R. Conner, E. Dumur, J. Grebel, I. Gutierrez, B. H. November, R. G. Povey, S. J. Whiteley, D. D. Awschalom, D. I. Schuster, and A. N. Cleland, "Quantum control of surface acoustic wave phonons," Nature, vol. 563, p. 661–665, 2018. [Online]. Available: https://www.nature.com/articles/s41586-018-0719-5

[126] A. Bienfait, K. J. Satzinger, Y. P. Zhong, H.-S. Chang, M.-H. Chou, C. R. Conner, E. Dumur, J. Grebel, G. A. Peairs, R. G. Povey, and A. N. Cleland, "Phonon-mediated quantum state transfer and remote qubit entanglement," Science, vol. 364, pp. 368–371, 2019. [Online]. Available: https://science.sciencemag.org/content/364/6438/368

[127] A. Bienfait, Y. P. Zhong, H.-S. Chang, M.-H. Chou, C. R. Conner, E. Dumur, J. Grebel, G. A. Peairs, R. G. Povey, K. J. Satzinger, and A. N. Cleland, "Quantum erasure using entangled surface acoustic phonons," Phys. Rev. X, vol. 10, p. 021055, Jun 2020. [Online]. Available: https://link.aps.org/doi/10.1103/PhysRevX.10.021055

[128] H.-S. Chang, Y. P. Zhong, A. Bienfait, M.-H. Chou, C. R. Conner, E. Dumur, J. Grebel, G. A. Peairs, R. G. Povey, K. J. Satzinger, and A. N. Cleland, "Remote entanglement via adiabatic passage using a tunably dissipative quantum communication system," Phys. Rev. Lett., vol. 124, p. 240502, Jun 2020. [Online]. Available: https://link.aps.org/doi/10.1103/PhysRevLett.124.240502

[129] Y. Chen, C. Neill, P. Roushan, N. Leung, M. Fang, R. Barends, J. Kelly, B. Campbell, Z. Chen, B. Chiaro, A. Dunsworth, E. Jeffrey, A. Megrant, J. Y. Mutus, P. J. J. O'Malley, C. M. Quintana, D. Sank, A. Vainsencher, J. Wenner, T. C. White, M. R. Geller, A. N. Cleland, and J. M. Martinis, "Qubit architecture with high coherence and fast tunable coupling," Phys. Rev. Lett., vol. 113, p. 220502, Nov 2014. [Online]. Available: https://link.aps.org/doi/10.1103/PhysRevLett.113.220502

[130] M. R. Geller, E. Donate, Y. Chen, M. T. Fang, N. Leung, C. Neill, P. Roushan, and J. M. Martinis, "Tunable coupler for superconducting xmon qubits: Perturbative nonlinear model," Phys. Rev. A, vol. 92, p. 012320, Jul 2015. [Online]. Available: https://link.aps.org/doi/10.1103/PhysRevA.92.012320

[131] E. Flurin, N. Roch, J. D. Pillet, F. Mallet, and B. Huard, "Superconducting quantum node for entanglement and storage of microwave radiation," Phys. Rev. Lett., vol. 114, p. 090503, Mar 2015. [Online]. Available: https://link.aps.org/doi/10.1103/PhysRevLett.114.090503

[132] W. Pfaff, C. J. Axline, L. D. Burkhart, U. Vool, P. Reinhold, L. Frunzio, L. Jiang, M. H. Devoret, and R. J. Schoelkopf, "Controlled release of multiphoton quantum states from a microwave cavity memory," Nature Physics, vol. 13, p. 882–887, 2017. [Online]. Available: https://www.nature.com/articles/nphys4143

[133] L. D. Burkhart, J. Teoh, Y. Zhang, C. J. Axline, L. Frunzio, M. Devoret, L. Jiang, S. Girvin, and R. Schoelkopf, "Error-detected state transfer and entanglement in a superconducting quantum network," arXiv preprint arXiv:2004.06168, 2020. [Online]. Available: https://arxiv.org/abs/2004.06168

[134] M. Pechal, J.-C. Besse, M. Mondal, M. Oppliger, S. Gasparinetti, and A. Wallraff, "Superconducting switch for fast on-chip routing of quantum microwave fields," Phys. Rev. Applied, vol. 6, p. 024009, Aug 2016. [Online]. Available: https://link.aps.org/doi/10.1103/PhysRevApplied.6.024009

[135] B. J. Chapman, E. I. Rosenthal, J. Kerckhoff, L. R. Vale, G. C. Hilton, and K. W. Lehnert, "Single-sideband modulator for frequency domain multiplexing of superconducting qubit readout," Applied Physics Letters, vol. 110, no. 16, p. 162601, 2017. [Online]. Available: https://aip.scitation.org/doi/abs/10.1063/1.4981390

[136] O. Naaman, J. A. Strong, D. G. Ferguson, J. Egan, N. Bailey, and R. T. Hinkey, "Josephson junction microwave modulators for qubit control," Journal of Applied Physics, vol. 121, no. 7, p. 073904, 2017. [Online]. Available: https://aip.scitation.org/doi/abs/10.1063/1.4976809

[137] A. Wagner, L. Ranzani, G. Ribeill, and T. A. Ohki, "Demonstration of a superconducting nanowire microwave switch," vol. 115, pp. –, 2019. [Online]. Available: https://aip.scitation.org/doi/abs/10.1063/1.5120009

[138] A. Potočnik, S. Brebels, J. Verjauw, R. Acharya, A. Grill, D. Wan, M. Mongillo, R. Li, T. Ivanov, S. V. Winckel, F. A. Mohiyaddin, B. Govoreanu, J. Craninckx, and I. P. Radu, "Millikelvin temperature cryo-cmos multiplexer for scalable quantum device characterisation," arXiv preprint arXiv:2011.11514, 2020. [Online]. Available: https://arxiv.org/abs/2011.11514

[139] S. Schaal, A. Rossi, V. N. Ciriano-Tejeland, T.-Y. Yang, S. Barraud, J. J. Morton, and M. F. Gonzalez-Zalba, "A cmos dynamic random access architecture for radio-frequency readout of quantum devices," Nature Electronics, vol. 2, p. 236–242, June 2019. [Online]. Available: https://www.nature.com/articles/s41928-019-0259-5

[140] S. Pauka, K. Das, J. Hornibrook, G. Gardner, M. Manfra, M. Cassidy, and D. Reilly, "Characterizing quantum devices at scale with custom cryo-cmos," Phys. Rev. Applied, vol. 13, p. 054072, May 2020. [Online]. Available: https://link.aps.org/doi/10.1103/PhysRevApplied.13.054072

[141] M. Colangelo, D. Zhu, D. F. Santavicca, B. A. Butters, J. C. Bienfang, and K. K. Berggren, "Compact and tunable forward coupler based on high-impedance superconducting nanowires," Phys. Rev. Applied, vol. 15, p. 024064, Feb 2021. [Online]. Available: https://link.aps.org/doi/10.1103/PhysRevApplied.15.024064

[142] B. Abdo, A. Kamal, and M. Devoret, "Nondegenerate three-wave mixing with the josephson ring modulator," Phys. Rev. B, vol. 87, p. 014508, Jan 2013. [Online]. Available: https://link.aps.org/doi/10.1103/PhysRevB.87.014508

[143] N. Marchand, "Transmission-line conversion transformers," Electronics, vol. 17, pp. 142–145, 1944.

[144] Z. R. Lin, K. Inomata, K. Koshino, W. D. Oliver, Y. Nakamura, J. S. Tsai, and T. Yamamoto, "Josephson parametric phase-locked oscillator and its application to dispersive readout of superconducting qubits," Nature communications, vol. 5, no. 4480, 2014. [Online]. Available: https://www.nature.com/articles/ncomms5480

[145] V. B. Braginsky and F. Y. Khalili, "Quantum nondemolition measurements: the route from toys to tools," Rev. Mod. Phys., vol. 68, pp. 1–11, Jan 1996. [Online]. Available: https://link.aps.org/doi/10.1103/RevModPhys.68.1

[146] D. Rosenberg, D. Kim, R. Das, D. Yost, S. Gustavsson, D. Hover, P. Krantz, A. Melville, L. Racz, G. O. Samach, S. J. Weber, F. Yan, J. L. Yoder, A. J. Kerman, and W. D. Oliver, "3d integrated superconducting qubits," npj Quantum Inf, vol. 3, no. 42, 2017. [Online]. Available: https://www.nature.com/articles/s41534-017-0044-0

[147] M. D. Reed, L. DiCarlo, B. R. Johnson, L. Sun, D. I. Schuster, L. Frunzio, and R. J. Schoelkopf, "High-fidelity readout in circuit quantum electrodynamics using the jaynes-cummings nonlinearity," Phys. Rev. Lett., vol. 105, p. 173601, Oct 2010. [Online]. Available: https://link.aps.org/doi/10.1103/PhysRevLett.105.173601

[148] C. K. Andersen, A. Remm, S. Lazar, S. Krinner, N. Lacroix, G. J. Norris, M. Gabureac, C. Eichler, and A. Wallraff, "Repeated quantum error detection in a surface code," Nature Physics, vol. 16, pp. 875–880, 2020. [Online]. Available: https://www.nature.com/articles/s41567-020-0920-y

[149] C. K. Andersen, J. Kerckhoff, K. W. Lehnert, B. J. Chapman, and K. Mølmer, "Closing a quantum feedback loop inside a cryostat: Autonomous state preparation and long-time memory of a superconducting qubit," Phys. Rev. A, vol. 93, p. 012346, Jan 2016. [Online]. Available: https://link.aps.org/doi/10.1103/PhysRevA.93.012346

[150] E. M. Purcell, H. C. Torrey, and R. V. Pound, "Resonance absorption by nuclear magnetic moments in a solid," Phys. Rev., vol. 69, pp. 37–38, Jan 1946. [Online]. Available: https://link.aps.org/doi/10.1103/PhysRev.69.37

[151] A. A. Houck, J. A. Schreier, B. R. Johnson, J. M. Chow, J. Koch, J. M. Gambetta, D. I. Schuster, L. Frunzio, M. H. Devoret, S. M. Girvin, and R. J. Schoelkopf, "Controlling the spontaneous emission of a superconducting transmon qubit," Phys. Rev. Lett., vol. 101, p. 080502, Aug 2008. [Online]. Available: https://link.aps.org/doi/10.1103/PhysRevLett.101.080502

[152] M. D. Reed, B. R. Johnson, A. A. Houck, L. DiCarlo, C. J. M., D. I. Schuster, L. Frunzio, and R. J. Schoelkopf, "Fast reset and suppressing spontaneous emission of a superconducting qubit," Applied Physics Letters, vol. 96, no. 203110, 2010. [Online]. Available: https://aip.scitation.org/doi/abs/10.1063/1.3435463

[153] B. T. Gard, K. Jacobs, J. Aumentado, and R. W. Simmonds, "Fast, high-fidelity, quantum non-demolition readout of a superconducting qubit using a transverse coupling," arXiv preprint arXiv:1809.02597, 2019. [Online]. Available: https://arxiv.org/abs/1809.02597

[154] R. Lescanne, M. Villiers, T. Peronnin, A. Sarlette, M. Delbecq, B. Huard, T. Kontos, M. Mirrahimi, and Z. Leghtas, "Amplification and squeezing of quantum noise with a tunable Josephson metamaterial," Nature Physics, vol. 16, pp. 509—513, 2020. [Online]. Available: https://www.nature.com/articles/nphys1090

[155] K. K. Likharev, Dynamics of Josephson junctions and circuits. Gordon and Breach science publishers, 1986.

[156] G. Dolan, "Offset masks for lift-off photoprocessing," Applied Physics Letters, vol. 31, p. 337, 2017. [Online]. Available: https://aip.scitation.org/doi/10.1063/1.89690

[157] B. J. Chapman, "Widely tunable on-chip microwave circulator for superconducting quantum circuits," Thesis, October 2017. [Online]. Available: https://jila.colorado.edu/sites/default/files/2019-03/ChapmanThesisOct25.pdf

[158] P. Le Corbeiller, "Matrix analysis of electric networks," p. 329, 1950. [Online]. Available: https://aapt.scitation.org/doi/abs/10.1119/1.1932586?journalCode=ajp

[159] K. Nagappan, "Step-by-step formation of bus admittance matrix," IEEE transactions on power apparatus and systems, vol. 89, pp. 812–820, 1970. [Online]. Available: https://ieeexplore.ieee.org/document/4074138

Appendix A

Introduction to Josephson junctions and SQUIDs

A.1 The Josephson relations

A Josephson junction, Fig. A.1, is formed by a non-superconducting region between two superconducting leads [83, 155]. The time-dependent current $I(t)$ flowing through the Josephson junction and the superconducting phase $\varphi(t) = 2\pi\Phi(t)/\Phi_0$ across it are governed by the Josephson relations:

$$I = I_c \sin(\varphi), \tag{A.1}$$

$$v = \frac{\Phi_0}{2\pi}\frac{\partial\varphi}{\partial t}, \tag{A.2}$$

where $\Phi(t) = \int_{-\infty}^{t} dt' v(t')$ the 'branch flux' across the junction, $v(t)$ the voltage across it, $\Phi_0 = h/2e$ is the magnetic flux quantum and I_c is the junction's critical current. The critical current parameterizes the dynamics of the Josephson junction, and generally depends on the geometry and material of its non-superconducting region.

From Eqs. A.1 and A.2, a Josephson junction acts like an inductor whose inductance L'_J depends on the current flowing across it according to,

$$L'_J = \frac{L_J}{\sqrt{1-(I/I_c)^2}}. \tag{A.3}$$

Where

$$L_J = \frac{\Phi_0}{2\pi I_c} \tag{A.4}$$

is the Josephson inductance. The solution to Eq. A.3 is plotted in Fig. A.1d. As the applied current I approaches the critical current I_c, the Josephson inductance diverges. For $I \geq I_c$ the junction behaves as a resistor and the Josephson relations no longer apply.

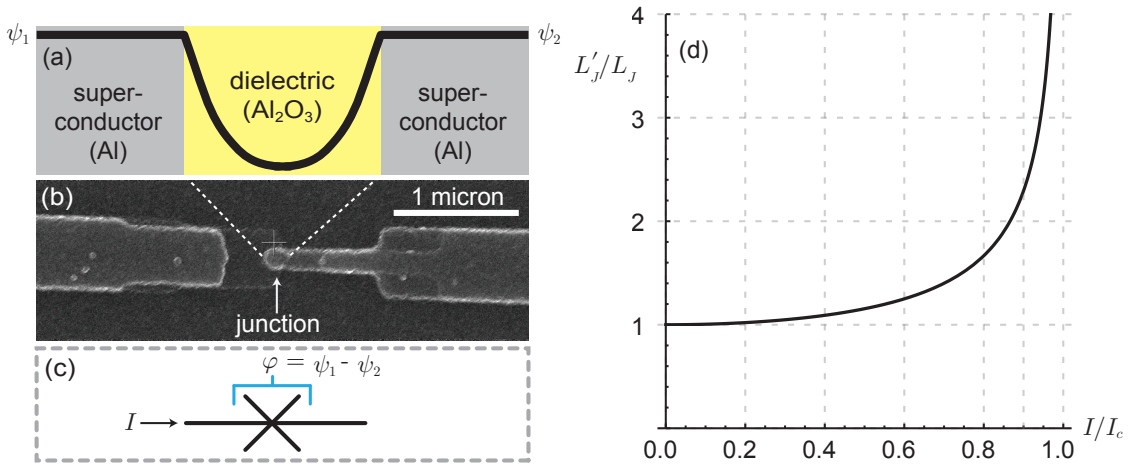

Figure A.1: **Introduction to Josephson junctions**. (a) A Josephson junction is formed by a non-superconducting region (often a dielectric) between two superconducting leads. The absolute value of the superconducting order parameter (illustrated by the thick black line) evanescently decays inside the junction, with the decay constant determined by the junction's critical current I_c (dependent on the junction geometry and material). The superconducting phase difference across the junction $\varphi = \psi_1 - \psi_2$, where ψ_1 and ψ_2 are the phases on either side of the junction, is given by the Josephson relations, Eq. A.1 and A.2. (b) Scanning electron microscope (SEM) image of a Josephson junction, fabricated by the author using the common 'double angle evaporation' technique [156]. The approximately 150 nm × 150 nm region at the center of the image consists of a thin layer of aluminum oxide (Al_2O_3) sandwiched between two layers of aluminum. (c) Josephson junctions are schematically illustrated by the '×' symbol. (d) Josephson inductance L'_J, as a function of the current I applied across a single junction, divided by the critical current I_c.

A.2 SQUIDs

A SQUID or 'Superconducting QUantum Interference Device' is formed by one or more Josephson junctions placed in a superconducting loop. A SQUID behaves as a single Josephson junction whose critical current is dependent on the magnetic flux threaded through its loop.

To understand this, consider a SQUID formed by two junctions with critical currents $I_{c,1}$ and $I_{c,2}$, arranged in parallel as in Fig. A.2a, and where the linear inductance of the loop itself is

neglected. Current I applied across the SQUID will divide into the currents I_1 and I_2 across side of the loop such that $I = I_1 + I_2$. From Eq. A.1,

$$I = I_{c,1} \sin \varphi_1 + I_{c,2} \sin \varphi_2, \tag{A.5}$$

where φ_1 and φ_2 are the superconducting phase drops across each junction. To ensure the superconducting order parameter remains single valued around the loop, these phase drops are related to the magnetic flux piercing the loop φ_{ext} by:

$$2\pi n = \varphi_2 - \varphi_1 - \varphi_{\text{ext}}, \tag{A.6}$$

where n is an integer.

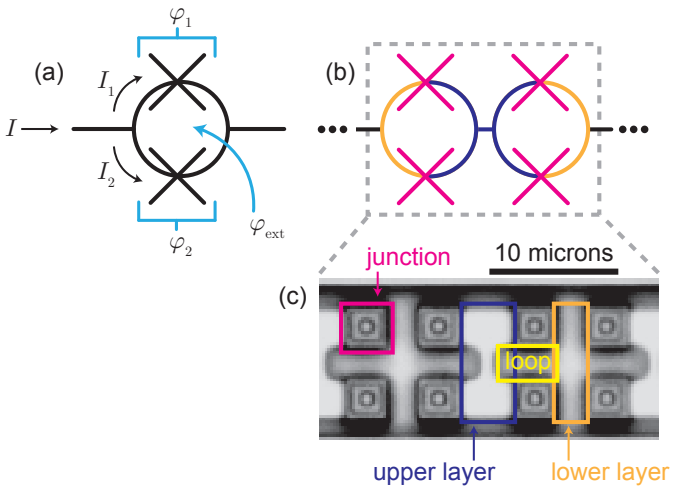

Figure A.2: **Introduction to SQUIDs**. (a) Two Josephson junctions in parallel form a SQUID (Superconducting QUantum Interference Device). Here, $I = I_1 + I_2$ is the current applied across the SQUID, with I_1 and I_2 the currents across each arm. The superconducting phase drops across the junctions, φ_1 and φ_2, are related to the magnetic flux φ_{ext} piercing the loop by Eq. A.6. (b) SQUIDs may be constructed in series to form an array. (c) Optical micrograph of an array of SQUIDs used in the TIBs of Ref. [23]. (For further information on fabrication of these SQUIDs, see Section 5.2 and Appendix B of Ref. [157]).

In a 'dc-SQUID' (the style used through this thesis), the two Josephson junctions are designed to be identical such that $I_{c,1} = I_{c,2} = I_c$. Following from Eq. A.5 and Eq. A.6, the dc-SQUID behaves like a single Josephson junction whose critical current is $2I_c \left|\cos\left(\varphi_{\text{ext}}/2\right)\right|$, or equivalently,

whose Josephson relation is modified to:

$$I = 2I_c \left|\cos\left(\frac{\varphi_{\text{ext}}}{2}\right)\right| \sin(\varphi)\,. \tag{A.7}$$

Here, I_c is the critical current of a single Josephson junction, and $\varphi_{\text{ext}}(t) = 2\pi\Phi_{\text{ext}}(t)/\Phi_0$ is the external magnetic flux applied through each SQUID loop, $\Phi_{\text{ext}}(t)$, scaled by the magnetic flux quantum. In general, this flux may be time-dependent. Note that Eq. A.7 neglects the self-capacitance of the Josephson junctions, the linear inductance of the loop, the inductance of the SQUIDs themselves, and any loss.

A.3 Arrays

A single junction or SQUID can be replaced by an *array* of many in series, Fig. A.2b,c. Denoting the superconducting phase difference over an array of identical SQUIDs as $2\pi\Phi/\Phi_0$, the phase difference across each individual SQUID equals $2\pi\Phi/N\Phi_0$, where N is the number of SQUIDs. From Kirchhoff's current law, the common-mode current through each individual SQUID equals the current I running through the entire SQUID array. The relationship between current flowing through an array of SQUIDs and the phase across it is therefore

$$I = 2I_c \left|\cos\left(\frac{\varphi_{\text{ext}}}{2}\right)\right| \sin\left(\frac{\varphi}{N}\right). \tag{A.8}$$

From Eq. A.8 we see that the effective nonlinearity of the SQUID-array is reduced relative to a single SQUID. In particular, the ratio of the leading nonlinear to the linear term in the expansion of the current-phase relation around $\Phi = 0$ scales with $1/N^2$.

Appendix B

SIMBA experimental schematic

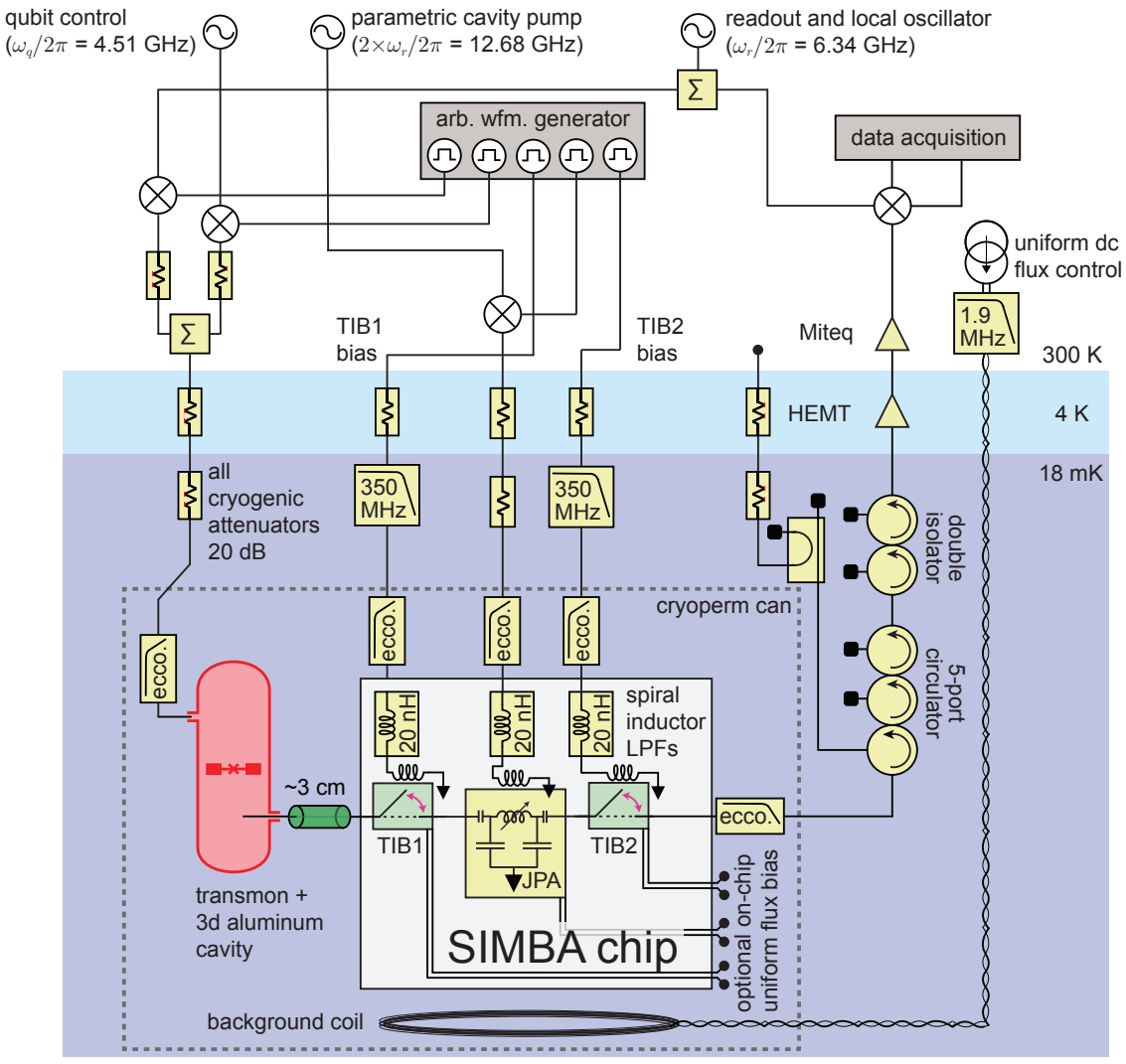

Figure B.1: Schematic for the experiment in Ref. [23].

Appendix C

Graph theory approach to circuit analysis

The scattering matrix $\mathbf{S}$ describes the response of a signal exiting port α of a network, given a signal incident on port β. More precisely, its elements $\mathbf{S}_{\alpha\beta}$ are defined as the ratio of a phasor v_β^+ incident on port β of a network to a phasor v_α^- outgoing from port α [34]:

$$\mathbf{S}_{\alpha\beta} = \frac{v_\alpha^-}{v_\beta^+}, \tag{C.1}$$

assuming that no other ports are being driven (such that $v_\gamma^+ = 0$ for $\gamma \neq \beta$).[1] The scattering matrix is a useful tool for characterizing circuit performance, but can be cumbersome to analytically derive for complicated circuits such as the superconducting switches developed in this thesis. Here, we review a simple, formulaic method for using graph theory to analytically calculating the scattering matrix of an arbitrary linear circuit.

A linear network is completely described by the following information:

(1) The connectivity of its nodes.[2]

(2) The impedance/admittance between connected nodes.

(3) Which nodes are connected to ports, and the characteristic impedance of each port.

Points (1) and (2) fully determine the admittance matrix $\mathbf{Y}$. The scattering matrix can be computed from $\mathbf{Y}$ combined with information about the ports of the network (3).

[1] Note that the diagonal elements of the scattering matrix are 'reflection coefficients' and the off-diagonal elements are 'transmission coefficients'.

[2] Nodes are regions of equipotential.

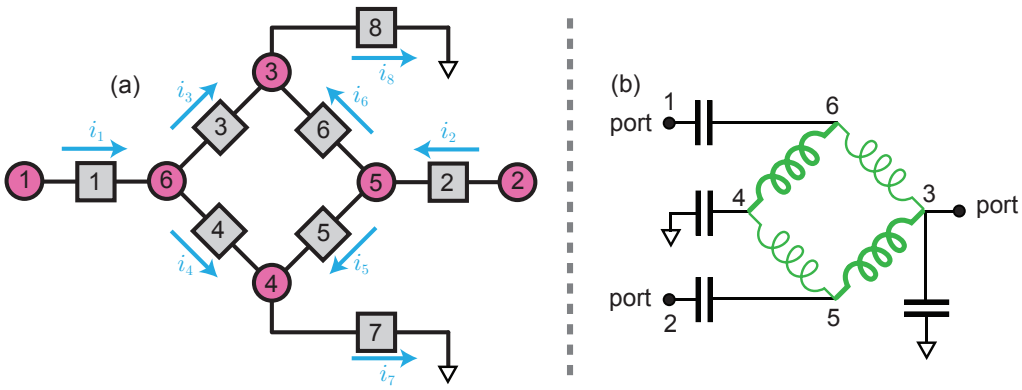

Figure C.1: **Graph theory approach to circuit analysis.** (a) An example network. Nodes (pink circles) are equipotential regions at potential v_ν where $\nu \in \{1, 2, ..., 6\}$. The m chords in the network are connected by impedances y_μ where $\mu \in \{1, 2, ..., 8\}$ (gray squares). The chords have currents i_μ running across them. (b) A lumped element diagram for a tunable inductor bridge (TIB) circuit (Chp. 5) which realizes a superconducting switch. This circuit is an example of the network in (a), where labels $1, 2, ..., 6$ correspond to the same nodes as in (a), and where nodes 1, 2 and 3 are specified to connect to ports.

C.1 Calculating the admittance matrix

Elements of the admittance matrix $\mathbf{Y}_{\alpha\beta}$ are defined as the current i_α at port α when driving port β with voltage v_β [34]:

$$\mathbf{Y}_{\alpha\beta} = \frac{i_\alpha}{v_\beta}, \tag{C.2}$$

when all other ports are short-circuited ($v_\gamma = 0$ for $\gamma \neq \beta$). Here, we compute the admittance matrix using graph theory.

Consider a circuit with n nodes each at potential v_ν, where $\nu \in \{1, 2, ..., n\}$. These nodes are connected by m chords. Each chord contains an admittance y_μ[3] where $\mu \in \{1, 2, ..., m\}$, and has a current i_μ flowing across. The direction corresponding to positive current flow across each chord can be arbitrarily chosen, but must be kept consistent throughout the analysis. The admittance matrix $\mathbf{Y}$ is [158, 159]:

$$Y = \mathbf{A}^T \mathbf{y} \mathbf{A}. \tag{C.3}$$

[3] The admittance of a circuit element is the inverse of impedance, and generally depends on the frequency ω. For example, the admittance of an inductor l is $1/j\omega l$, the admittance of a capacitor c is $j\omega c$ and the admittance of a resistor r is $1/r$.

Here, $\mathbf{y}$ is the 'primitive admittance matrix', an $m \times m$ diagonal matrix whose frequency dependent elements are the admittances y_m across chords of the network,

$$\mathbf{y} = \begin{bmatrix} y_1 & 0 & \dots & 0 \\ 0 & y_2 & \dots & 0 \\ \vdots & \vdots & \ddots & \vdots \\ 0 & \dots & 0 & y_m \end{bmatrix}. \tag{C.4}$$

For example, for the network in Fig. C.1b the primitive admittance matrix is:

$$\mathbf{y} = \begin{bmatrix} j\omega c & 0 & 0 & 0 & 0 & 0 & 0 & 0 \\ 0 & j\omega c & 0 & 0 & 0 & 0 & 0 & 0 \\ 0 & 0 & 1/j\omega l_1 & 0 & 0 & 0 & 0 & 0 \\ 0 & 0 & 0 & 1/j\omega l_2 & 0 & 0 & 0 & 0 \\ 0 & 0 & 0 & 0 & 1/j\omega l_1 & 0 & 0 & 0 \\ 0 & 0 & 0 & 0 & 0 & 1/j\omega l_2 & 0 & 0 \\ 0 & 0 & 0 & 0 & 0 & 0 & j\omega c & 0 \\ 0 & 0 & 0 & 0 & 0 & 0 & 0 & j\omega c \end{bmatrix}, \tag{C.5}$$

where we have assumed all capacitors have equal capacitance c, thin inductors (connecting nodes 3 and 6, and nodes 4 and 5) the have inductance l_1, and thick inductors (connecting nodes 4 and 6, and nodes 4 and 5) to have inductance l_2. In Eq. C.3, the 'adjacency matrix' $\mathbf{A}$ is an $m \times n$ matrix which describes the circuit topology, i.e. which pairs of nodes are connected. For example,

the adjacency matrix for the circuit in Fig. C.1 is:

$$\mathbf{A} = \begin{bmatrix} 1 & 0 & 0 & 0 & 0 & -1 \\ 0 & 1 & 0 & 0 & -1 & 0 \\ 0 & 0 & -1 & 0 & 0 & 1 \\ 0 & 0 & 0 & -1 & 0 & 1 \\ 0 & 0 & 0 & -1 & 1 & 0 \\ 0 & 0 & -1 & 0 & 1 & 0 \\ 0 & 0 & 0 & 1 & 0 & 0 \\ 0 & 0 & 1 & 0 & 0 & 0 \end{bmatrix}. \tag{C.6}$$

The simplicity of Eq. C.3 is that both $\mathbf{y}$ and $\mathbf{A}$ may be easily written down by inspecting a circuit diagram.

To understand the adjacency matrix, let's first consider some of the different rows in Eq. C.6: the first row refers to a current i_1 flowing *from* node 1 *to* node 6 across admittance y_1, with the current direction specified by the direction of the arrow in the network diagram in Fig. C.1a. The second row refers to current i_2 flowing *from* node 2 *to* node 5 across admittance y_2. The final row refers to current i_8 flowing *from* node 3 to ground, etc. Now let's consider the columns: for example, the third column has -1 as its 3^{rd} and 6^{th} elements, and $+1$ as its 8^{th} element. This means node 3 (specified by the third column) has currents i_3 and i_6 flowing *into* it, and current i_8 flowing *out* of it. As another example, consider the final (6^{th}) column: its first element is -1 and its 3^{rd} and 4^{th} elements are $+1$, meaning that node 6 has current i_1 flowing into it and currents i_3 and i_4 flowing out of it. In this manner we can construct the adjacency matrix $\mathbf{A}$ based on inspection of a network, or equivalently, $\mathbf{A}$ fully describes the connectivity of this network.

C.2 Calculating the scattering matrix

The scattering matrix $\mathbf{S}$ follows from the admittance matrix. To determine the scattering matrix, we construct the network such that nodes 1 through $1 \leq n_p \leq n$ are connected to ports of

characteristic admittance $1/z_0$ (the inverse of the usually defined characteristic impedance z_0).[4] The next $n_p + 1$ through n nodes of the network are not connected to any port, or equivalently, are connected to ports of characteristic admittance of zero (characteristic impedance approaching infinity).

The scattering matrix of the network is [34]:

$$\mathbf{S} = \left(\frac{1}{z_0}\mathbf{M} - \mathbf{Y}\right)\left(\frac{1}{z_0}\mathbf{M} + \mathbf{Y}\right)^{-1}, \tag{C.7}$$

where $\mathbf{M}$ is an $n \times n$ matrix whose upper-left $n_p \times n_p$ block is an identity matrix and all other blocks are zero. For the example in Fig. C.1b:

$$\mathbf{M} = \begin{bmatrix} 1 & 0 & 0 & 0 & 0 & 0 \\ 0 & 1 & 0 & 0 & 0 & 0 \\ 0 & 0 & 1 & 0 & 0 & 0 \\ 0 & 0 & 0 & 0 & 0 & 0 \\ 0 & 0 & 0 & 0 & 0 & 0 \\ 0 & 0 & 0 & 0 & 0 & 0 \end{bmatrix}. \tag{C.8}$$

In conclusion, the scattering matrix for an arbitrary network can be calculated by constructing the admittance matrix using graph theory, Eq. C.3, and then plugging the result into Eq. C.7. For example, the scattering parameters for the circuit shown in Fig. C.1b are shown in Fig. C.2 for two different choices of parameters.

[4] Here, we assume all ports have the same characteristic admittance. See Chp. 4 of Ref. [34] for analysis where these values are different.

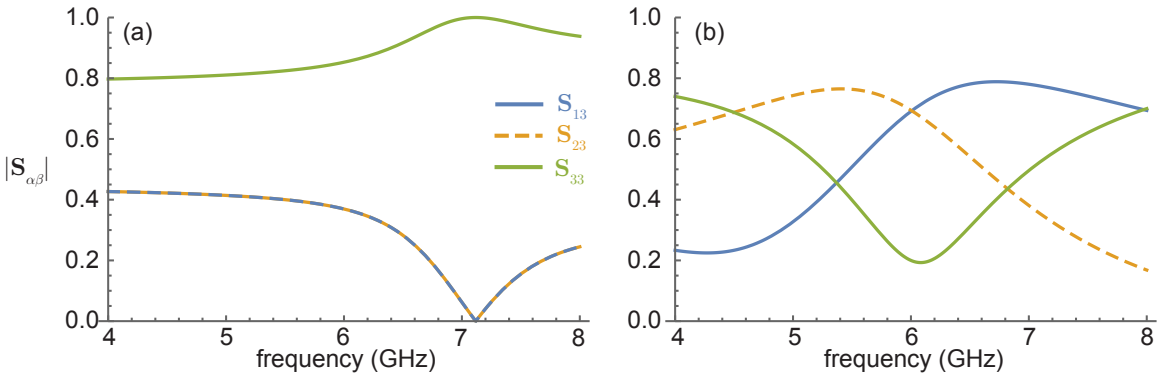

Figure C.2: **Scattering parameters from an example circuit.** (a) Scattering parameters of the circuit in Fig. C.1b where all capacitors have equal value of 1 pF, all inductors have an equal value of 1 nH, ports 1, 2 and 3 are attached to nodes 1, 2 and 3, respectively, and all ports have a characteristic impedance of 50 Ohms. From symmetry of the circuit, the transmission from port 3 to port 1 and from port 3 to port 2 have equal magnitude at any frequency. (Connecting the balanced ports of a balun to ports 1 and 2 realizes a TIB in *reflect* mode, where the bridge is balanced.) (b) Scattering parameters where thick/thin inductors in Fig. C.1b have different values of 2 nH and 0.5 nH, respectively, but other parameters are the same as in (a). (Connecting the balanced ports of a balun to ports 1 and 2 realizes a TIB in *transmit* mode, where the bridge is *im*balanced).